The University of Nottingham

UNITED KINGDOM · CHINA · MALAYSIA

Investigation of the Performance of a Slotted Aerofoil at Low Reynolds Numbers

Otuami Obiga, B. Eng. (Hons)

Thesis submitted to the University of Nottingham for the degree of Doctor of Philosophy

October 2016

Author's Declaration

- I Otuami Obiga declare that I am the sole author of this thesis titled, "Investigation of a Slotted Aerofoil for Wind Power Generation at Low Reynolds Numbers".

- The entire work was done while in candidacy for a PhD degree at the University of Nottingham Malaysia Campus.

- This work has not been submitted in any form for another degree at any other university or institution of higher learning.

- All information derived from published or unpublished works of others have been duly acknowledged.

Otuami Obiga

Signature: ……………………   Date: 21 October 2016

Abstract

Slotted aerofoils have been suggested by numerous researchers as an effective means of controlling boundary layer flow separation, and improving aerodynamic performance. Numerous slot designs have been studied at high Reynolds number, but there is scarcity of study of such slots effect on aerofoil performance in low Reynolds number scenarios. In the present work, wind tunnel and numerical investigation of the effect of a unique slot configuration and its geometric parameters on the aerodynamic performance of a NACA0018 aerofoil at low Reynolds number was executed. The aim of this work is to ascertain if the unique slot configuration on the NACA0018 can improve the aerodynamic performance compared to a plain NACA0018, and if the slotted NACA0018 could be applied as rotors on a Darrieus-style vertical axis micro wind turbine for small scale energy conversion at low wind speeds. Four aerofoils were initially fabricated for the wind tunnel tests, each conforming to the NACA0018 profile; a plain aerofoil and three other slotted aerofoils, each with a span–length slot positioned at X=15%, X=45% and X=70% from the leading edge. The, chord length (c), span, slot slope (ψ) and slot width of the slotted aerofoils were 0.25m, 0.3m, 55° and 0.02c respectively. A 2D wind tunnel set up was used in testing the four aerofoils at Reynolds numbers of 92×10^3 138×10^3, 184×10^3 and 230×10^3, within $\alpha = 0°$ to $\alpha = 20°$ range of incidence. Comparing the slotted and plain aerofoils, the aerodynamic force data shows that the presence of the slots was detrimental to aerodynamic performance especially when the slot location is closer to the leading edge. Therefore, a 2D numerical parametric study of slot width and slope was carried out using ANSYS FLUENT 16.0 with the intention of improving the lift–to–drag (L/D) ratio of the span–length slotted aerofoils. Furthermore, a final slot configuration consisting of segmented slot pattern which incorporated the results of the parametric study was fabricated and tested in a wind tunnel. The aerodynamic force analysis shows a 50% increase in L/D ratio of the slotted aerofoil with slot position at

X=70%, but its aerodynamic performance was still less than the Plain NACA0018. Thus this work proves that the suggested slot layout did not improve the aerodynamic performance of the NACA0018 aerofoil and as a result, it cannot be recommended to be used as a vertical axis wind turbine rotor. Finally, in order to improve the NACA0018 aerofoil performance, it was suggested that a new slot layout with slot slope on the pressure side inclined towards the leading edge should be designed and studied.

Acknowledgements

First and foremost my thanks go to God almighty for the successful completion of this research project. To my supervisor Dr. Yousif Abakr, thanks for your technical support, guidance and contribution to this project, I have learnt so much from you both personally and professionally. Thanks to the University of Nottingham Malaysia campus for my PhD scholarship, tuition waiver and the lab facilities which made this work possible. Finally my appreciation goes to my family and friends; to my family I have missed you all so much, words cannot describe how much you all mean to me, and to my friends Victor Ewhe, Ejikeme Ezeigwe, Chioma Eberechukwu Ewurum, Azubuike Ile, and Kenobi Isima thanks for your encouragement, motivation and the good times we shared.

Table of Contents

List of Figures

List of tables

Abbreviations and Symbols

Nomenclature

A	area of aerofoil	[m2]
c	chord length	[m]
C_{do}	aerofoil drag coefficient	[--]
C_{du}	uncorrected aerofoil drag coefficient	[--]
C_l	lift coefficient	[--]
C_N	normal force coefficient	[--]
C_T	tangential force coefficient	[--]
C_{lu}	uncorrected lift coefficient	[--]
D	aerofoil drag force	[N]
F_N	normal force	[N]
h	height of working section	[m]
L	aerofoil lift force	[N]
R	blade radius	[m]
V	flow velocity	[m/s]
S_α	Stall Angle	[°]
V_a	induced velocity	[m/s]

Vc	chordal velocity	[m/s]
V_w	wake velocity in downstream	[m/s]
V_n	normal velocity component	[m/s]
V_∞	wind velocity	[m/s]

Greek

σ	streamline curvature factor	[--]
ω	angular velocity of turbine	[rad/s]
α	aerofoil angle of attack	[°]
ε	blockage factor	[--]
ε_{sb}	solid blockage	[--]
ε_{wb}	wake blockage	[--]
Λ	aerofoil shape factor	[--]
π	pi constant	[--]
θ	azimuth angle	[°]
ψ	Slot Slope	[°]

Abbreviations

AoA   Angle of Attack

LMS   Lead Mid Slot

LMTS   Lead Mid Trail Slot

LS   Lead Slot

LTS   Lead Trail Slot

MS   Mid Slot

MTS   Mid Trail Slot

NACA   National Advisory Committee on Aeronautics

TS   Trail Slot

VAWT   Vertical Axis Wind Turbine

Chapter 1

1. Introduction

In 2010, the world's energy consumption increased by 5.6%, the highest rate since 1973 [1]. This increase affected all forms of viable energy sources on earth. Globally, energy consumption grew more rapidly than the economy, meaning that the energy intensity of economic activities increased. This increase in energy consumption is attributed to rising population, industrialisation and energy demand in previously less developed countries, aggravated by gross inefficiencies in available energy sources in all countries [2]. For example, energy consumption of China grew by 11.2%, and China surpassed the US as the world's largest energy consumer. Crude Oil remains the world's leading energy source, at 31.4% of global energy consumption [3]. Notwithstanding, oil continued to lose market share for the 11th consecutive year. Whatever the source of energy is, there is an overriding need for efficient and sustainable energy generation and usage [4]; renewable energy in power generation grew by 16.3% and accounted for a record 5.3% of global power generation [5].

Increase in environmental awareness and depleting fossil fuel resources has led to the search for more environmental friendly energy sources, of which wind power is one of the cheapest and most promising option. Wind is formed as a result of the rotation of the earth coupled with the uneven heating and cooling of its surface. Wind energy is a clean, renewable infinite and widely distributed energy resource with an emerging influence as a renewable energy resource in global energy policy in response to climate change. Wind energy utilisation is one of the fastest growing renewable energy source worldwide reaching more than 318 GW of installed wind capacity in

2013 [6] and presently accounts for more than half of the renewable power generation with a 20.7% increase from previous year [5].

Over the years extensive research efforts have been put into improving the technology of electricity generation through wind. Most wind power plants are located in Europe, US, China and India [7]. Presently, the energy conversion systems are growing in efficiency, size and capacity. The industry is well-established and wind turbine capacity ranges from tens of watts to megawatts, and turbine diameters spanning about 1m to more than 100m [4]. With such increase in capacity, wind farms have been integrated into the grid in most parts of Europe, Australia and Asia, and other countries are steadily increasing and exploring their wind power potential in the areas of feasibility studies and wind turbine installation. However, not all countries can boast of high wind speed values. For these countries, small scale wind turbines are considered useful either as supplementary or grid-connectable energy sources. One of the major challenges of employing these small scale wind turbines is the problem of improving their efficiency when they operate in low-wind speed environments.

There has been a rebirth of interest in vertical axis wind turbine (VAWT) not only because of its independency on wind direction and design simplicity but also for its low noise levels due to low blade speed [8], which makes it suitable for urban application. Urban wind power is a growing sector and it has been receiving tremendous attention from researchers due to the growing need to supplement household energy demand. For example, an analysis of roof-top mounted Darrieus VAWT has shown that 70% of the intended capacity factor could be exploited especially when a building reasonably higher than the average surrounding obstructions, with suitable geometric proportions to the upwind structure is selected. Nonetheless, different cities present different difficulties especially in terms of wind speed profile, building aspect ratio and proximity, topography, heat intensity, etc. [9]. All these factors including wind turbine inherent problems

like dynamic stall and starting torque issues can cumulatively or independently affect turbine yield.

Early flow transition over aerofoils at higher angles of attack often result in the manifestation of unsteady flow phenomena such as drag enhancement, local separation regions, vortex shedding, boundary layer transition and turbulence. These phenomena are associated with high energy deficit that adversely affects the aerodynamic loads in the form of lift loss and drag increase [10]. Therefore, the ability to control these occurrences in wind turbines can effectively improve turbine energy yield. Boundary layer control in fluid mechanics can be divided into two main categories; active and passive boundary layer control. Active boundary layer control techniques usually involve the use of pulsating or pumping devices (most often imbedded in the flow body) to inject or remove fluid from the boundary layer. On the other hand passive flow control requires no auxiliary power and is simpler and economical to implement, hence in recent times it has been receiving more attention from researchers [11]. Previous studies have shown that surface texturing by introducing grooves, bumps and riblets are renowned examples of passive flow control approach that can reduce drag by changing near-wall flow structure. These surface geometrical modifications in transverse or longitudinal orientation to the flow stream can serve as vortex generators introducing vortices and increasing momentum of the boundary layer region, hence mitigating aerodynamic losses and delaying boundary layer separation [12][13].

This work emphasizes on the use of slots as passive flow separation control devices. Slots in aerofoils assist in accelerating flow into the boundary layer by directing a portion of the fluid in the main stream from a region of high pressure to the retarded region of the boundary layer. Early experimental investigation of passive flow control studies involving slots were carried out in NACA (National Advisory Committee on Aeronautics) wind tunnel facility in Hampton, Virginia, U.S. in the early 20th century. However, these studies were mainly for flight application, and the aerofoils studied were cambered and equipped with multiple fixed slots and

flaps[14][15]. Currently there appears to be a dearth of experimental and numerical data on slotted aerofoils involving passive flow control methods in low Reynolds number flows and small wind turbine application. Most available literatures on slotted aerofoils are more directed towards active flow control methods with high Reynolds number [16][17][18]. Therefore, there is need for further exploration of the benefits of using slots for passive flow control on wind turbine rotors in low wind speed environments. Figure 1.1 shows a vertical axis wind generator by Shenzhen Wind Water Wheel Technology Co. Ltd. The wind generator comprises of a pond (circular water tank containing water) and a floating platform with eight rotors fastened on it. Together, the platform and the rotors rotate in the pond under the drive of wind. Each rotor consists of rows of slots along its span at multiple chordal positions. The slot layout was designed to mimic the arrangement of gills in some marine organisms.
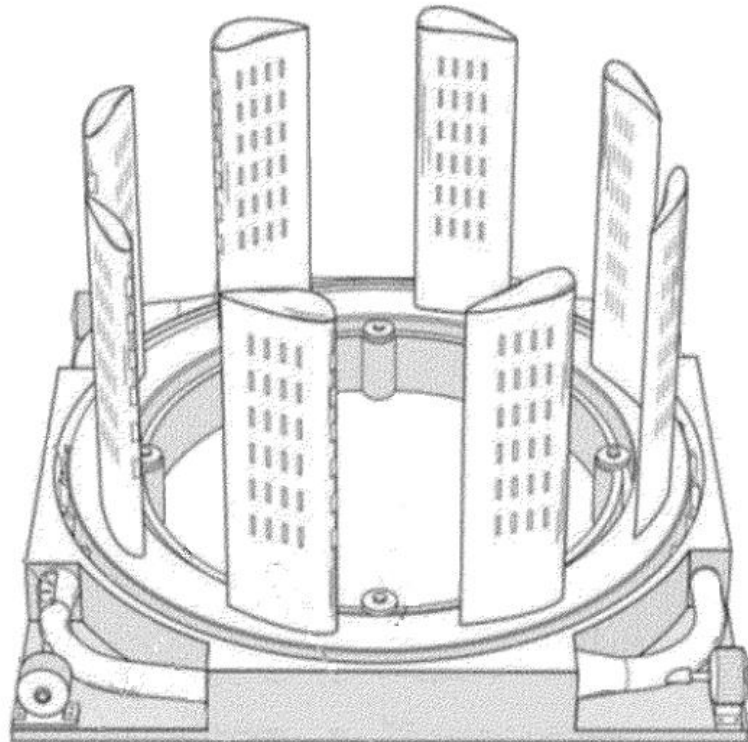
Figure 1.1: Water float rotor wind generator by Shenzhen Wind Water Wheel Technology Co. Ltd [19]

This wind generator which was installed in Shenzhen city in 2008 was designed with the intention of improving wind turbine energy yield. Also, as a result of its floating rotors its application could be extended to offshore wind harvesting. Much of the work presented here was motivated by the water float rotor wind generator (see Fig 1.1) [19] and the quest to determine if indeed the use of slots as a passive flow control device could improve the aerodynamic performance of a thick aerofoil in low Reynolds number flow condition. Thus, for this work, a similar slot layout was produced on a NACA 0018 aerofoil and wind tunnel test, smoke visualization and CFD studies were performed on both the slotted NACA 0018 and a plain NACA 0018 aerofoils in order to investigate the net effect of the slots on aerodynamic performance. The range of Reynolds number was chosen in correlation with the wind speed range in Malaysian cities.

1.1 Aims and Objectives

The broader aim of this work is to contribute substantially to the foundation of this barely explored aspect of applied aerodynamics in regards to passive flow control in aerofoils and small scale wind turbine rotors. The proposed slot configuration has never been experimentally or numerally studied. Therefore, this work is also aimed at investigating and verifying the effect of the slots on the aerodynamic performance of a NACA0018 aerofoil. The fundamental objectives are as follows;

- To investigate the effect of the slots on a NACA0018 lift and drag forces at low Reynolds number ($92x10^3$, $138x10^3$, $184x10^3$ and $230x10^3$) and angle of attack between 0° to 20°.

- To study the effect of the slot position on the aerofoil performance.

- To evaluate the influence of slot geometric parameters such as; multiple slot positions, slot width, span–length slot, spanwise patterned slots and slot slope on the aerodynamic performance of the slotted NACA0018 aerofoil at low Reynolds number.

- To compare the performance of the slotted NACA0018 aerofoils to a plain NACA0018 aerofoil.

1.2 Thesis Layout

A progressive and effective parametric approach was followed for a successful completion of this work. The series of works that constitute the main body of this thesis is divided into 6 chapters. A brief description of each chapter is given bellow;

1. **Introduction** – This chapter summarizes the current state of renewable energy resources with more emphasis on wind power generation. A brief insight into the slotted NACA 0018 is given with reference to its relevance to vertical axis wind turbine in low wind speed condition.

2. **Literature Review** – A review of literatures relevant to this work such as experimental and CFD works on wind turbines and aerofoil performance enhancement are summarized. More attention was given to recent publications.

3. **Experimental Methodology** – This chapter covers the entire wind tunnel experimental set up procedures from the wind tunnel calibration, data analysis, error analysis, turbulence intensity test, and wall boundary correction factors. The smoke visualization test and set up was also illustrated.

4. **Numerical Methodology** – The CFD set up procedure was discussed in this chapter. The entire process consists of; flow domain and mesh description, definition of boundary

conditions, and mesh independency tests. Also an illustration of the turbulence model of choice was given.

5. **Results and Discussions** – Discussion of experimental lift and drag results of four fabricated NACA0018 aerofoils; a plain aerofoil and three slotted aerofoils with side slots at three different locations. CFD parametric study of multiple slot combination, slot width and slot slope was carried out with the purpose of improving the slotted aerofoil performance.

6. **Conclusion and Recommendation** – The major findings from this work were summarized and recommendations for future work were suggested.

Chapter 2

2. Literature Review

In this chapter, literatures related to this research are reviewed with special emphasis on recent works. The scope of works reviewed covers research papers, reports, thesis and major areas of interest are; wind energy availability and cost, vertical axis wind turbines, small wind turbines, flow separation control, experimental and CFD studies on aerofoil performance at both low and high angles of attack, drag reduction, slotted aerofoil, dynamic stall etc.

2.1 Potential of low speed Wind Energy

The evolution of wind energy into a reputable and viable energy option currently makes it economically competitive with conventional power plants. Recent studies show that the capacity factor of wind can go up to 35% – 40% in favourable wind sites [20]. Therefore this puts it far ahead of other renewable energy option like solar. In the last decade, new turbine products have been developed and made available in the market [21]. Ezio Sesto et al [22] carried out a decade forecast and overview of wind exploitation for global electricity demands. From their observation, development in turbine (wind energy conversion system) which covers blade and rotor design and material selection, blade solidity and aerodynamics, state of the art technology (turbine size and capacity) are some of the main factors that have contributed to the advancement of wind power. Other factors include, roles of energy agencies in research and development, trends in the wind turbine market and factors boosting the market. Small-scale wind energy covers small wind turbines (SWTs) rated less than 50 kW [23] which are generally intended to supply electricity to buildings and also offer an economic option for electricity generation in off-grid remote regions of developing countries. Such systems are receiving increasing interest

globally as member of a class of microgeneration technologies with potential to reduce carbon footprint and for their ability to operate in low wind speed environment. In general, average wind speed of over 5 m/s is strong enough for a good operation of SWTs. For example, a high wind speed and power density of magnitudes 8.6 m/s and 458 W/m^2 respectively were reported at a height of 10 m in Jos city Nigeria [24]. Also, in El-Kef region Tunisia, a mean wind speed of 5.65 m/s and an average wind power density of 217 W/m^2 were recorded at a height of 40 m [25] . However, feasibility studies and measurement of regional or local wind resources is necessary to support the development of new wind energy projects especially in developing countries. A few existing evaluations show several regions of wind energy viability, but accessibility to reliable wind speed data remains a major challenge, since such estimates are not yet available globally.

2.1.1 Availability of Wind Energy in Malaysia

The increasing popularity of wind power has led several countries to explore their wind energy capability. However, in order to accurately predict the energy output or embarking on any wind power project in a site, it is imperative that adequate statistical data on wind be collected. Over the last few decades wind power meteorology has established itself as a core subject in applied meteorology and climatology. Some tasks that require good meteorological knowledge and expertise are wind turbine operation and design, resource assessment, wind power forecasting, etc. [26].

The stochastic nature of wind is a challenge in wind energy estimation and management. Taking the wind speed in peninsular Malaysia for example, the potential of wind energy resources is influenced by the monsoon seasons, turbine height, geographical site, among other factors. Malaysia has two main Monsoon seasons in a year, the Southwest monsoon (Mid-May to September) and the Northeast Monsoon season (November to March) with transition months in April and October. Wind speed varies across the months in a year [27]. Therefore, energy output estimation of a wind turbine at any particular site requires knowledge of the distribution of the

wind speed. Observed wind speed data over a particular period of time can be analysed, and information on the percentage of time for which the speed is within a specific range or above threshold value can be extracted [28]. Several probability density functions such as gamma, Rayleigh and Weibull distribution, can be used to present the wind speed frequency distribution. But in recent times, the Weibull distribution has become the most commonly used statistical distribution for representing and assessing wind energy potential [29][30]. Akorede et al [31] statistically analysed the wind speed time series data of six chosen sites across the Malaysia using the Weibull distribution. Data was collected for a period of 20 years from 1989 to 2008 at a height of 10m above the ground. The results obtained show that wind speed is strongest in the northeast Monsoon season. Of the six locations evaluated and many others sites studied by numerous researchers, Mersing has the highest monthly average wind speed of 5.4m/s, producing an average power density of 57.58 W/m^2 with a capacity factor of 4.39%. This is equivalent to 378 MWh energy production per annum, making Mersing the most viable [32][33]. Fig. 2.1 shows that the probability that the annual mean wind speed would be higher than 2 m/s in Mersing is 0.9.
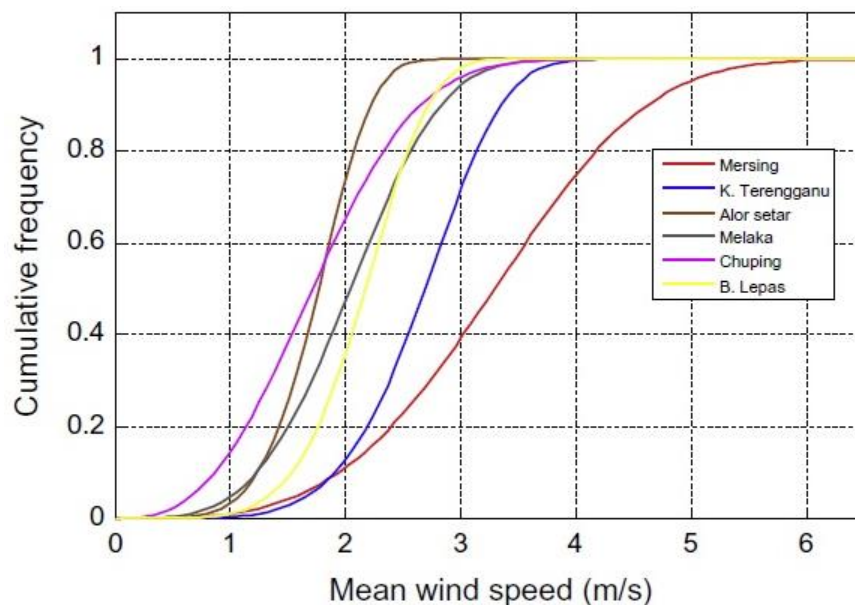
Figure 2.1: Cumulative frequency of annual wind speed at 10m hub height [31]

Generally, Malaysia can be classified as a low profile wind speed country. From investigations, wind turbine generator systems connected to the grid–network may not be commercially viable. Nevertheless small–scale wind turbine systems are more suitable, sustainable and may be economically viable in a few regions. Due to the low wind speed values (Fig 2.2), vertical axis wind turbines seem to be the best option to capture wind energy in Malaysia. The reason for this will be justified in section 2.2 below. At present, iWind Energy (M) Sdn Bhd has successfully installed 40 units of its iWind VAWT all over Malaysia [34].
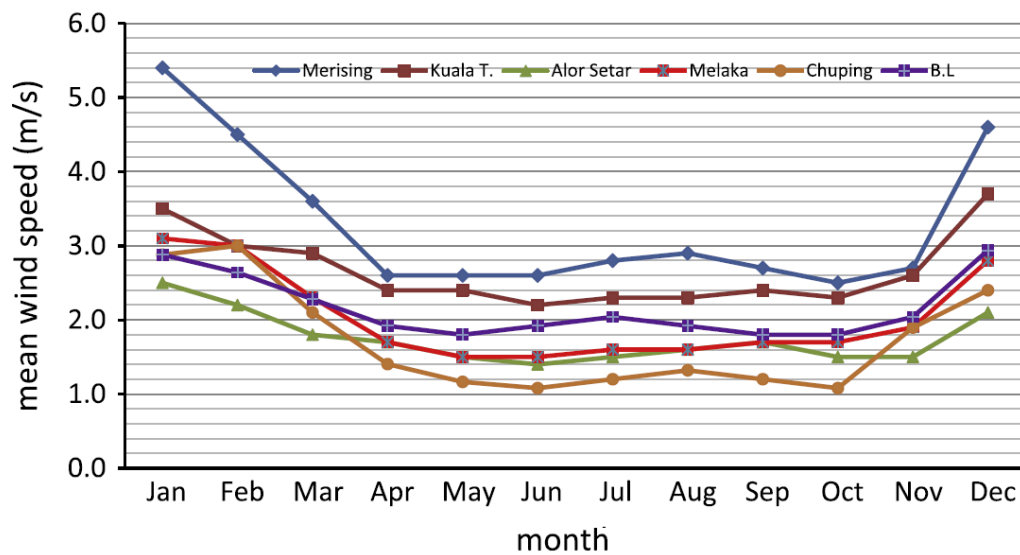
Figure 2.2: Monthly mean wind speed at 10m hub height for some selected sites [31]**.**

2.2 Vertical Axis Wind Turbines (VAWTs)

The VAWT configuration was the first ever wind turbine to be used for harnessing energy from the wind (in Sistan, Iran in the 7th century), modern researchers lost interest in it due to the initial perception that VAWT cannot be used for a large scale electricity generation [8]. For years, the horizontal axis wind turbine (HAWT) was the focus of all wind energy related research and presently a large portion of all major wind power plants are HAWT because its efficiency. However, there is a resurgence of interest regarding vertical axis wind turbines because they

possess some unique features that make them more preferable for smaller scale applications [35]. They also have a low environmental impact and can operate in a complex flow environment like urban areas especially on rooftops or for building integrated solutions [36]. VAWT does not need a yaw mechanism to align itself with the direction because it is omnidirectional. Its generator is mounted at ground level hence encouraging accessibility and easy maintenance [8]. Furthermore, recent studies show that VAWT can be installed much closer to each other compared to HAWT, so that the power density per square meter could be considerably increased [37]. For these reasons, VAWT is playing a greater role in wind power generation than ever before. A comparison between VAWT and HAWT is presented in Table 2.1 below.

Table 2.1: Comparison between VAWT and HAWT [37]

Property	Vertical Axis Wind Turbine (VAWT)	Horizontal Axis Wind Turbine (HAWT)
Tower sway	Small	Large
Yaw mechanism	No	Yes
Self-starting	No	Yes
Overall formation	Simple	Complex
Generator location	On ground	Not on ground
Height from ground	Small	Large
Blade's operation space	Less	Large
Noise produced	Less	Relatively high
Wind direction	Independent	Dependent
Obstruction for birds	Less	High
Ideal efficiency	More than 70%	50-60%

One particular VAWT that is receiving much attention is the Darrieus wind turbine due to its design simplicity, low cost and good maintenance properties. This configuration was one of the earliest VAWT designs and was first patented in 1931 by Georges Jean Marie Darrieus a French engineer who designed it in 1928. Among the various VAWTs, this design has the highest values of efficiency [38]. Darrieus rotors are lift force dependent VAWTs consisting of two or three thin curved blades. The blade configurations of this turbine can be categorized into curved and straight bladed types (Fig. 2.3), each having its own advantages and disadvantages. However, one major drawback of the latter is that it suffers from poor starting torque performance issues, but it is easier to manufacture and maintain than the former.

a   b   c
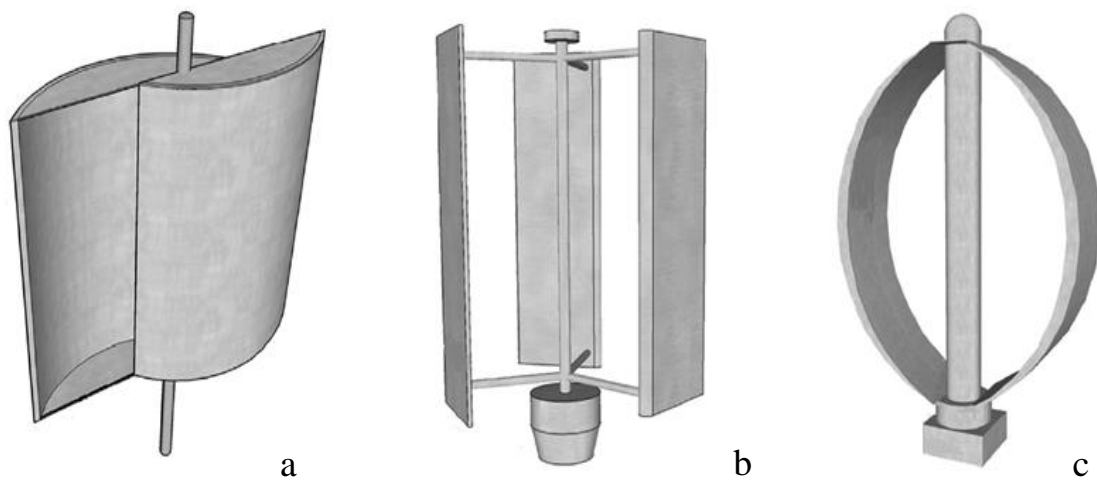
Figure 2.3: (a) Savonius rotor (b) Darrieus rotors-Straight blade   (c) Darrieus rotor-egg beater [37]

The performance of a VAWT is a measure of its power coefficient (C_p), a dimensionless factor expressed as the ratio of actual electric power produced by a wind turbine divided by the total wind power flowing into the turbine blades at specific wind speed. This factor depends on the aerodynamic characteristics of the turbine rotor blades. Therefore implementation of performance optimization techniques such as design or selection of aerofoils that are both aerodynamically and structurally efficient, as well as boundary layer control techniques, are essential in mitigating

dynamic stall, boundary layer separation, starting torque issues and other problems inherent in a turbine.

2.3 Dynamic Stall and Starting torque problem in VAWTs

Dynamic stall is one of the major problems affecting VAWTs due to its influence on operational limits [39] [40]. This phenomenon manifests itself on turbine rotors during rapid pitching or oscillatory motions in which the angle of incidence changes rapidly and exceeds the static stall limit [41]. The rapid change can cause a strong leading edge vortex (LEV) shedding which provides additional suction over the upper aerofoil surface as it travels downstream. This increased suction leads to performance gains in lift and flow attachment, but the LEV quickly becomes unstable and detaches from the aerofoil as soon as they pass behind the trailing edge. The LEV detachment is accompanied by dramatic turbine power reduction, loss of lift due to drag increase, sudden increase in pitching moment and large unsteady loads that compromises the structural integrity.

Studies have shown that dynamic stall is prevalent in Darrieus rotors operating at tip speed ratio (TSR) lower than 5 [42]. Dynamic stall at low tip speed ratios is mainly due to large incidence angle when rotors move across stall region during operation. This is a major problem for small VAWTs installed on buildings as they are required to operate at low tip speed ratios in order to reduce noise, hence spending much of their time in a stalled state. In 1998 Fujisawa and Takeuchi [43] used dye injection technology to visualize the flow field of a small Darrieus rotor during dynamic stall at a Reynolds number of 3000 and tip speed ratios of 1, 2, and 3. They also observed the development of vortices and their interaction with blade in the downwind pass. Ferreira et al [44][45][46] studied the effect of dynamic stall in a 2D single–bladed VAWT of NACA 0015 profile section at 3 tip speed ratios (2, 3, and 4), using PIV and CFD methods. The

study was conducted at Reynolds number of 50,000 and 70,000. The PIV experimental result shows that the clearest effect of dynamic stall was observed at the lowest tip speed ratio of 2. The leading edge separation vortex and trailing edge shed vorticity showed development of dynamic stall on the upwind suction side of the aerofoil. Reporting on the simulation accuracy of the turbulence models in predicting the dynamic stall development, the Detached Eddy Simulation (DES) turbulence model presented results that agreed with experiments and closely predicted the trailing edge shed vorticity development [44].

Improving starting torque ability can enhance the performance of a VAWT by reducing the turbine start–up time [47][48]. Therefore a longer interval of power production might be achieved which could contribute significantly to the energy yield. Several methods to overcome the Darrieus type VAWT inability to self-start have been studied. Many of these methods are centred on optimizing configurations of geometric parameters, such as: modification of turbine solidity, blade camber and thickness; blade offset pitch angle, inclined blades and blade lean forward angle, etc. [49]. For example, cambered aerofoils have been praised for their ability to increase the starting torque and produce more tangential thrust over a wider range of angle of attack than symmetric aerofoils [50][51]. Singh et al [48] investigated the self–starting characteristics of a three-bladed H-type Darrieus rotor equipped with unsymmetrical S1210 blades with different blade solidities (ranging from 0.8 to 1.2) at various azimuthal positions. On evaluation of the power coefficient (C_p), it was observed that there is an optimum rotor solidity at which power coefficient is highest, and that high blade solidity is in fact necessary for improving rotor performance. A maximum C_p of 0.32 was obtained for rotor solidity 1.0 and wind speed 5.7 m/s. Also designers are sometimes compelled to create a hybrid configuration by incorporating accessories devices to the wind rotors in order to spin it up and put it in operating condition. Example of such devices are; the electric motor, Savonius rotor (drag type VAWT), etc. A combined structure of Savonius and Darrieus Straight–bladed VAWT was fabricated by Fang Feng et al [52] to boost starting torque performance. The model was set up in such a way that

angle of attack where the static torque of the Savonius rotor is largest was fixed at the angle where the static torque of the straight–bladed VAWT is small. Aerodynamic analysis on static and dynamic torque performance data of both wind tunnel test and simulation results shows that the starting torque performance was improved significantly [52][53]. Though some of these methods contribute positively to starting torque, but increase in cost, design complications, reduction in peak efficiencies and operating range are some of the major problems that could be encountered.

2.4 Boundary Layer Separation Control

Boundary layer separation is the breakaway or detachment of fluid from the surface of a submerged body in a stream of flow, due to severe adverse pressure gradient which may be imposed on the boundary layer by the external pressure conditions [54][55]. For a flow body such as an aerofoil or a wind turbine blade, boundary layer separation can lead to high friction drag, lift loss and stall in severe cases. Armstrong et al [56] studied flow separation on a high Reynolds number, high solidity VAWT with straight blades. At peak operating power the blades showed large regions of flow separation on the upwind blade pass extending from early in the upwind pass from an azimuthal angle $\theta = 40°–50°$ (where the blade is moving directly upwind at $\theta = 0°$) to over 60° into the downwind pass. The overall separation behaviour of the straight blades showed the significance of dynamic stall and the interaction of the separated vortex with the blade as mechanisms in lift generation. Numerous studies have shown that the aerodynamic performances of wind turbine blades are strongly affected by the viscous effects concentrated in the boundary layer, and the practical benefits of boundary layer separation control in flow bodies are enormous [54]. There is a variety of boundary layer separation control methods employed in improving aerodynamic performances of wind turbine rotors. These methods are classified into two main classes: passive flow separation control and active flow separation control. Both are aimed at overcoming the adverse pressure gradient by either directly increasing the momentum in

the boundary layer by creating vortices or higher momentum fluid, or by suction of stagnant fluid from the separated zone.

2.4.1 Passive flow Control

Passive controls usually do not require auxiliary power or a control loop. Besides slots and flap systems, a renowned technique that has proven to effectively reduced drag on an aerofoil is surface texturing [57]. This usually involves the use of vortex generators or grooves in the form of riblets and waves in transverse or longitudinal direction to the flow stream. It is expected that for different incidence angles, these surface modifications could significantly alter the flow separation phenomena, vortex shedding, pressure and force coefficient of an aerofoil [58]. Some passive flow control devices such as vortex generators (VG's), slotted aerofoils and high lift devices are examined:

Vortex generators (VGs)

Some of the earliest experimental studies of basic flow-separation control were conducted at the NASA Langley Research Center 20–in x28–in shear flow tunnel in the late 1980s. Separation control capability of numerous types of passive flow-control devices were examined and compared [59][60]. The effectiveness of vortex generators (VGs) as passive flow control devices is well known. The heights of these devices are often set in orders below or above the boundary layer thickness δ. Several experimentally and numerically studies have been carried out over the last few decades to assess their potential. Notable among these studies are the experimental works of Lin [61][62] on low-profile VGs (between $h/\delta \approx 10\% \ to \ 50\%$) to control boundary layer separation. These low-profile VGs were just as effective in delaying separation as the conventional VGs with ($h/\delta \approx 80\%$). Kerho et al. [63] presented an experimental investigation of various low-profile VGs on a Liebeck LA2573A low Reynolds number aerofoil to reduce the separation bubble and hence reduce drag on the aerofoil. The chord Reynolds numbers Re_c of

the aerofoil examined was between 2 x10^5 and 5x10^5 at pre–stall AoAs, which represent typical operating conditions for a low–Reynolds number aerofoil. In order to control the laminar separation bubbles, the generators were located just downstream of the aerofoil's suction pressure peak (at 22% aerofoil chord), and are contained completely within the boundary layer.

Grooves and riblets can also be classified as vortex generators. These devices on the surface of an aerofoil can reduce drag by changing the near-surface flow structure. Notwithstanding the deficiencies of most numerical turbulence models in predicting characteristics especially at flow-separated regions, Lin et al showed the ability of numerical methods in reproducing realistic turbulent structures using a three–dimensional large eddy simulation for turbulent flow around a modified NACA0012 aerofoils with wavy surfaces [58]. The instantaneous flow patterns, time-averaged pressure fields, and force coefficients were captured at different angles of attack and compared with a smooth NACA 0012 aerofoil at Re = 1.6 x 10^5. The flow structures and surface pressure distributions on wavy aerofoils were found to be significantly different from those on the smooth NACA 0012 aerofoil. For angles of attack less than the baseline stall angle of a smooth NACA 0012 aerofoil, a slight decrease of lift coefficient was observed for the wavy aerofoils, but increases up to 20% greater than that of a smooth NACA 0012 aerofoil when the angle of attack is larger than the baseline stall angle of 13°. Also, the flow over the leading edge on the wavy aerofoil remained attached at post stall angles of attack. The mechanism of a relatively wide spanwise groove for laminar separation bubble on the suction side of a low speed highly loaded low pressure turbine blade (Re_c = 50,000) was investigated by Luo et al [64]. Compared with a smooth suction surface, the grooved surface was effective in shortening of the separation bubble, which contributed to the flow loss reduction, by thinning the boundary layer behind the groove and promoting earlier transition in the separation bubble.

On the other hand a V–groove riblet (Fig 2.4 b) reduces the skin friction drag, and the amount of the decrease varied with riblet geometry (height h and spacing s between the grooves) [65].

Measurement of the drag force using a three-component load-cell showed that the micro riblet film (MRF) grooves of $100\,\mu m$ reduces the drag coefficient by about 6% at Re $= 1.5$ x10^4, when compared with the smooth aerofoil. [57]. Flow visualization shows that, the momentum of the fluid particles is increased, resulting in a better resistance to flow separation [66]. Also, the near wake behind the MRF-covered aerofoil had a shorter vortex formation region and higher vertical velocity component compared with that behind the smooth aerofoil. The percentage of drag reduction by the riblets varied greatly and in some cases the riblets were found to be detrimental to the aerofoil. Partial riblet coverage appears in some cases to be more effective than its complete coverage counterpart.

(a)   **(b)**
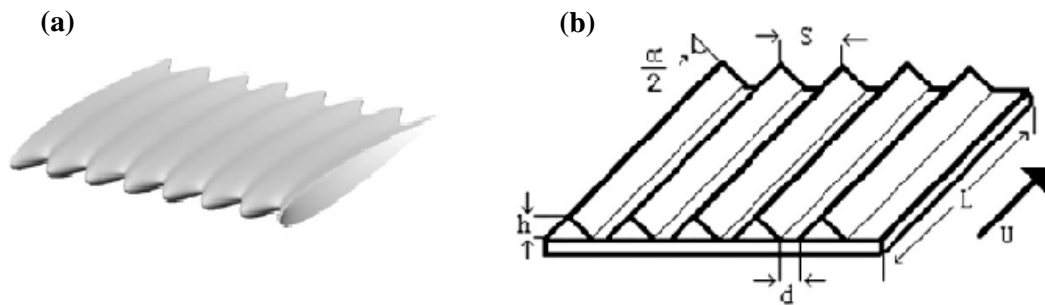
Figure 2.4: Micro Riblet Film aerofoils (a) Curvy grooves (b) V-groove riblets.

Slotted Aerofoils and High Lift Devices

Slots and high lift devices such as flaps and slats are aerodynamic features in the form of a spanwise gap on an aerofoil or aircraft wing, which diverts fluid from the lower surface of the wing element in a freestream to the upper surface. Figure 2.5 shows a schematic diagram of a section an aircraft wing consisting of a slat and a flap. Slots are fixed, non–closing gaps, while flaps and slats can open and close the gap (slot) which they create, thus they are termed moveable slots. Slats are situated at the leading edge of an aircraft wing, when deployed they allow the wing to operate at a higher angle of attack, thus producing a higher lift coefficient. Flaps on the

19

other hand are located at the tail end of an aircraft wing and they also aid in increasing lift coefficient.
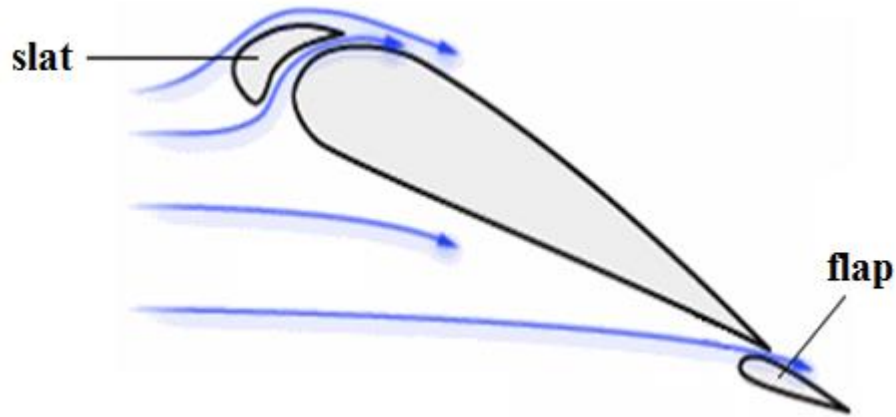
Figure 2.5 High lift device

The use of these devices for controlling flow was initially introduced by Lachman in 1924 [67], and their implementation on aircraft wings was probably the earliest and most successful application of passive flow control [68]. However, the first detailed experimental study was carried out by Weick et al in 1932 to examine their aerodynamic performance [15] [69]. In their study, an investigation of lift and drag characteristics of a Clark Y aerofoil (a cambered aerofoil) equipped with fixed slots (immovable slats and a trailing–edge flap) was conducted. Different combinations of slot locations were examined in order to identify the configuration with optimal aerodynamic performance (see Fig. 2.6). Results from the study shows that the slots aided in a large increase in maximum lift coefficient, but the minimum drag coefficient and structural integrity was compromised in some configurations.
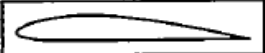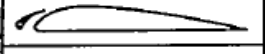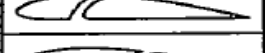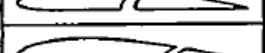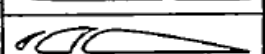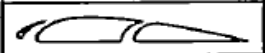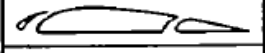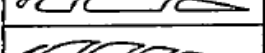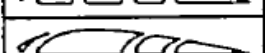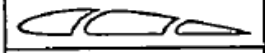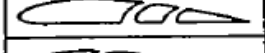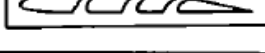
Slot combination	$C_{L_{max}}$	$C_{D_{min}}$	$\frac{C_{L_{max}}}{C_{D_{min}}}$	$\alpha_{C_{L_{max}}}$
				°
	1.291	0.0152	85.0	15
	1.772	.0240	73.8	24
	1.596	.0199	80.3	21
	1.548	.0188	82.3	19
	1.440	.0164	87.8	17
	1.902	.0278	68.3	24
	1.881	.0270	69.7	24
	1.818	.0243	74.6	23
	1.930	.0340	56.8	25
	1.885	.0319	59.2	24
	1.885	.0363	51.9	25
	1.850	.0298	62.1	24
	1.692	.0226	74.2	22
	1.672	.0214	78.2	22
	1.510	.0208	72.6	19
	1.662	.0258	64.4	22

Figure 2.6: Multiple stationary slots on a Clark Y aerofoil. Figure from [15].

The presence of a front slot led to a significant increase in maximum coefficient of lift compared to other configurations with no front slot. Also, the angle of attack at which the maximum coefficient of lift occurred was higher. For the single slot configurations, the maximum coefficient of lift and minimum coefficient of drag decreases as the slot location moves from front to rear. Overall, for a low cambered aerofoil like the Clark Y, no substantial gain in aerodynamic performance would be achieved by fitting more than one slot.

Gillis and McKee [70] investigated the aerodynamics characteristics of a NACA23012 aerofoil with an 18.05% chord Maxwell leading edge slat (a simple slat mechanism) and with a slotted

and split flap for the purpose of determining the optimum slot gap of the Maxwell slat, and the aerodynamics characteristics of the aerofoil with several deflections of both types of flaps. For all possible slot–flap combinations tested, the highest maximum coefficient of lift was obtained with slot gaps of 0.0175c and 0.02c (i.e. 1.75% and 2% of the chord length). However, as the slot gap was increased up to the optimum, the profile drag increased except in the range near maximum lift coefficient and the pitching moment became increasingly negative. Comparing the results with that of previous experiment on a 0.30c Maxwell slat, there was a more gradual loss in lift gradient at the angle of attack near the stall. This effect produced a rounded top on the lift curve and caused the angle of attack at maximum lift coefficient to occur at 3° higher for the 0.1805c slat than for the 0.303c slat even though the maximum coefficient of lift was lower. On the same aerofoil profile, pressure distribution over the upper and lower surfaces for various combinations of angle of attack and flap settings was investigated by Harris and Lowry [14]. Their data, which consisted of pressure diagrams and graphs of section coefficient showed that, the forces on the slat were smaller than the forces on the same portion of a plain airfoil (of the same profile) at low angle of attack, but the forces built up to very high values above the stall of the plain aerofoil. The loads on the flap on the slotted aerofoil were approximately the same as the loads on the flap on a plain aerofoil. Hence any conventional flap should show little change in load if similar leading-edge slot were added to the combination. Beri and Yingxue [71] investigated the performance of an aerofoil in a Darrieus 3-bladed turbine with a modified trailing edge flap inclined at 15° at low tip speed ratios using CFD (Fig. 2.9). Simulation results showed that the modified aerofoil exhibits better self-starting performance both in steady and unsteady flow conditions for the modelled turbine.
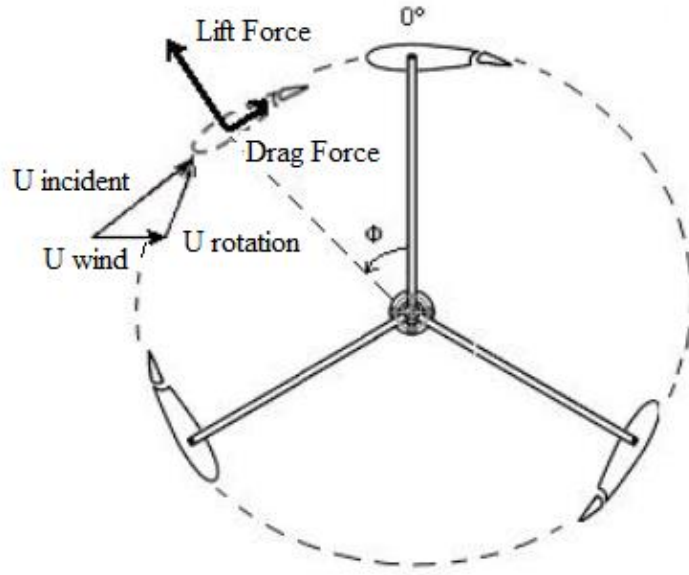
Figure 2.7: Topographic view of model with lift and drag component [71]**.**

By using two-dimensional CFD optimization approach, Gaunaa et al. [72] [73] quantified the effects of using slats on the inner part of a thick multi–megawatt rotor to boost power production. The result indicates that the advantages of using slats may be maximized if the slats and the main rotor blade are designed simultaneously. Ragheb and Selig [74] established that utilizing a multi-element aerofoil configuration at the root section of the wind turbine blade improves the aerodynamic characteristics and overall performance of the wind turbine. Narsipur et al. [75] studied the performance of a multi-element aerofoil for a megawatt-scale wind turbine using two-dimensional steady state CFD simulations. The aerofoil consists of one main element and two flaps by varying flap deflection, gaps and overhangs. Results show that increase in the flap gap, overhang and deflection can increase the aerodynamic efficiency of the multi-element aerofoil system. However, there is no fixed location of the flaps that is optimal for all operation regimes of the wind turbine blade.

2.4.2 Active Flow Control

Active flow separation control techniques involve putting energy into the flow usually with the help of actuators. These actuators are transducers that convert an electrical signal to a desired

physical quantity that create controllable disturbance. Active flow control techniques can be classified into: fluidic actuators, plasma actuator and moving object/surface, etc.

Fluidic Actuators

These devices use fluid injection or suction to produce oscillatory velocity or pressure perturbations in order to achieve a certain amount of control on the flow. The two most commonly used fluidic actuators are synthetic jets and boundary layer suction or blowing actuators. Synthetic jets are based on alternating momentary ejection of fluid into the flow to create vortices and a higher momentum boundary layer [76]. With boundary layer suction, low energy air in the fluid layer adjacent to the surface is removing through suction slots or a porous surface (Fig. 2.10), while boundary layer blowing directly adds momentum to the retarded fluid particles near the surface thus, modifying the velocity profile [77].
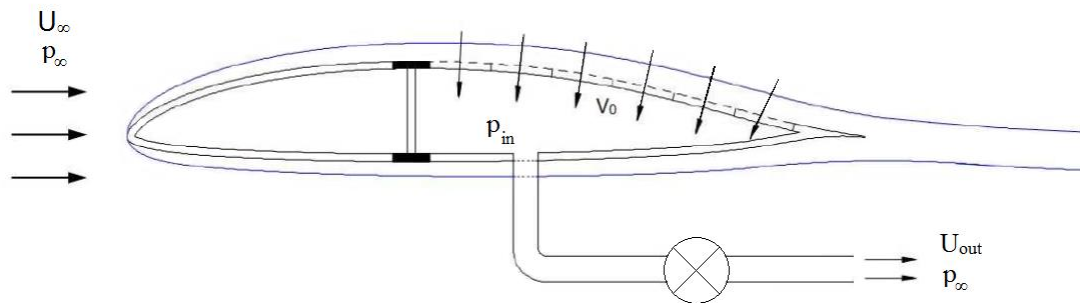
Figure 2.8: Working principle of boundary layer suction [78].

Chawla [79] experimentally applied surface-suction on the suction-surfaces of NACA 0012 and S814 aerofoils at Re 8×10^4 to 5×10^5 by drawing air into the aerofoils through a slit. The lift and drag coefficients as well as the stall characteristics were improved. Based on these improvements, an analysis of coefficient of power (C_P) versus input power for a small wind turbine blade with constant suction was explored. Amitay et al. [80] used a synthetic jet, positioned near the leading edge of a thick symmetric aerofoil, to reattach the separated flow on the upper surface of the aerofoil at stall. Improvement in computational fluid dynamics has made it possible to

numerically study synthetic jets [16] [81] and obtaining results that are in good agreement with experimental data [82]. Kim et al [83][84] analysed numerical simulation results of flow control using a synthetic jet on a NACA23012 aerofoil with a 20% plain flap at Reynolds number of $2.19x\ 10^6$ for various angles of attack, jet velocities and frequencies. For low frequency, a small vortex penetrated to the large separated flow at the leading edge, which led to a significant size decrease of the leading edge separation vortex. In contrast, for high frequency, the small vortex did not grow enough to penetrate into the large separation vortex. It is evident that synthetic jets and suction slots can contribute positively to aerofoil performance. However, effects of actuation on the flow depend on the position of the jet slot (separation point) and the magnitude of the jet velocity. However, most available literatures on slotted aerofoils are flight related (high Reynolds number). Therefore, there is still a lot to be done in the study of slots in aerofoils at low Reynolds numbers for VAWTs.

Plasma Actuators

Plasma actuators are available in different forms, depending on the technique used in obtaining plasma. Generally, ionization of the flowing air transpires by supplying voltage to an electrode or dielectric material. Thus localized momentum is added to the flow through a collision process of the travelling charged particles due to electric field gradient. Examples of plasma actuators are plasma sheet actuators and dielectric barrier discharge actuators. David Greenblatt et al [85] studied the performance of a high solidity VAWT with dielectric barrier discharge (DBD) plasma actuators installed on leading edges of the blades. On evaluation of results based on wind tunnel testing, turbine peak power coefficient showered a 38% improvement overall. N. Benard et al [86] investigated the effects of steady and unsteady actuations on the lift and drag coefficients of a NACA 0015 aerofoil using time-averaged force measurements. Results indicate that the drag coefficient is reduced and stall regime can be delayed by one or two degrees. However, like

fluidic actuators, the position of the plasma actuator from the separation line is crucial for effective flow control. Thus the higher this distance, the higher the intensity level required [87].

Overall, the advantages of plasma actuators as well as other active flow control techniques are that they are compact and easy to integrate into a functioning device, and are more effective means of controlling flow in most cases. However, the main cause for concern is the amount of energy needed for their continuous operation, especially when they are used in renewable energy applications where a reasonable positive net energy output is expected. On the other hand, passive control devices are usually more preferable because they are safer, less problematic, easily applicable and require an overall less operating cost, thus making them more interesting for renewable energy application.

2.5 Aerofoil at Low Speed

The study of aerofoil performance at low Reynolds number finds application in many fields, such as aerospace, marine industry, etc. It is also relevant in understanding small scale wind turbine performance at low wind speed conditions. In small–medium scale wind turbines, a Reynolds number range of 10^4 to 10^5 is of interest, and it is well–known that many significant aerodynamic problems occur in this range [88][89][90]. Laminar boundary layer on the upper surface of an aerofoil in a flow steam is susceptible to separation, even at low angles of attack, the resulting changes in the separated shear layer has a strong influence on the entire flow field [91]. Furthermore, nonlinear features emerge in the lift curve of symmetrical aerofoils; the maximum lift–to–drag ratio deteriorates rapidly when the chord Reynolds number decreases, hysteresis phenomena occurs in some cases in the lift characteristics of some aerofoils at low Reynolds numbers due to differences in laminar boundary separation and attachment as the aerofoil pitches up and down [92]. These problems can be fairly managed using thin aerofoils, but they are

generally not structurally viable for VAWTs due to the large centrifugal loads turbines have to withstand.

2.5.1 Wind Tunnel and Computational Fluid Dynamics Tests of Aerofoils

Decades ago when computational aerodynamics and analysis became prevalent, it was forecasted that wind tunnel tests will become inferior to numerical techniques. But presently numerical solutions to high viscous flow problems are still mired by large computational resource requirement, slow work pace, and inadequate turbulent flow models [93]. For the foreseeable future, the wind tunnel will remain a fundamental tool to study aerofoil performance, and also a means for validating prototypes and numerical techniques before implementation. Various experimental techniques have been employed in studying aerodynamic and boundary layer characteristics of aerofoil at low Reynolds numbers. The common techniques are: wind tunnel aerodynamic force data measurement procedures, which usually employs a force balance or pressure tapings, or a combination of both [94]; and flow visualization techniques such as particle image velocimetry (PIV) and smoke visualization. Selig et al [95] [96] carried out wind tunnel tests on 34 different aerofoils at low Reynolds numbers and obtained the lift and drag data. These aerofoils were categorized according to their applications, and within each group their performance was compared. The difference in performance between the aerofoils depended greatly on both Reynolds number and geometric profile. Usually, aerofoil prototypes to be tested are limited to the size of the wind tunnel test section, thus during operation they may not be expected to experience deep stall. Therefore, tests performed by Selig et al. and many other researchers are often restricted to low angles of attack (-10° to 20°, refer to Table 2.2) due to high level of uncertainties associated with tests at post stall angles. Consequently, to date, there appears to be a shortage of low Reynolds number aerofoil data in deep stall conditions for VAWT application.

27

Table 2.2: Wind Tunnel test of Aerofoils at low angles of attack.

Aerofoil	Reynolds Number	Incidence Range	Researchers
SM-4308	46×10^4 to 12×10^4	-4° to 15°	Sudhakar et al [97]
NACA 66_3-018	4×10^4 to 40×10^4	-16° to 16°	Mueller et al [98]
NACA0012	2.0×10^4 to 5.0×10^4	-6° to 6°	Kim et al [99]
S822	1.0×10^5 to 5.0×10^5	-10° to 20°	Selig et al [100]
E387	1.0×10^5 to 5.0×10^5	-10° to 20°	Lyon et al [101]
GA(W)-1	1.6×10^5	-4° to 20°	Yang et al [102]

In operation, a VAWT rotor continuously changes its angle of incidence over 360°. Therefore, in order to characterize the complete range of an aerofoil performance in VAWTs, it is imperative that the required aerofoil data at the appropriate Reynolds number range should accommodate both pre-stall and deep stall conditions. Sheldahl and Klimas [103] experimentally investigated the effect of aerofoil thickness on aerodynamic performance at low Reynolds number (36×10^4 to 1×10^7) for four symmetrical four–digit NACA profiles with thickness range from 9% to 15% for angles of attack up to 180°. The data were obtained were integrated with vertical axis wind turbines performance prediction computer codes. The results were also used to extrapolate performance data for three additional aerofoils of profiles thickness 18% to 25% using an aerofoil section characteristics synthesizer computer code. Wind tunnel tests, conducted for the purpose of performance prediction and data acquisition of some VAWT aerofoils at higher incidence angles [104]–[109] reveals that the lift curve normally exhibits a second lift peak at incidence angle of around 45° (second stall angle) and a maximum drag (or drag peak) at around 90°. For symmetric aerofoils, the test range is usually from 0° to 180°. Fig. 2.9 and Fig. 2.10 shows the lift and drag coefficient from some selected study of symmetrical aerofoils over a 180° range of AoA. In both figures, the results from Bergeles et al. [110], Critzos et al. [111], Massini et al. [112] and Sheldahl and Klimas [103] were obtained from NACA0012 aerofoils, while that of Pope [113] was from a NACA0015 aerofoil; results for which should be similar to NACA0012, particularly

in post–stall region. Results from NASA's AERODAS model (Spera [114]) for an infinite aspect ratio, 12% thick aerofoil, and thin aerofoil lift theory are also included. Further information regarding force measurements of the aerofoils, as well as factors that affect performance, such as the aspect ratio AR (a relevant consideration even when trying to reproduce two–dimensional flows) and the chord–to–height ratio, c/h, of the aerofoil and tunnel are given in table 2.3. The wall proximity of the wind tunnel test section (measured as chord–to–height ratio c/h of the aerofoil and tunnel) [115] had a significant effect on both post stall and deep stall measurements of lift and drag forces. The impact of wall proximity on measured data leads to an increase in measured forces; this is known as blockage effect, and the ratio c/h serves as an indicating factor. The data presented in Fig 2.9, Fig 2.10 and Table 2.3 suggests that higher blockage induces higher post–stall peaks. Blockage effect in wind tunnels cannot always be easily diminished; increasing tunnel size is impractical, and reducing model size leads to increased inaccuracies in profile reproduction and reductions in Reynolds numbers achievable in a given tunnel [116]. Alternatively, computed results from closed wind tunnels are processed with blockage correction equations [117]. However, the limits of existing wind tunnel corrections for closed test sections seem to be exceeded under deep–stall, probably as a result of inadequate consideration of the effect of downwash on streamline curvature under the bluff–body conditions of deep–stall. A less commonly used method to mitigate blockage effect is the use blockage tolerant test sections, these types of test section provide low blockage effect for test models by replacing the conventional solid side and ceiling walls with porous walls, allowing flow to exit and enter the main channel [118]. Other factors that can affect aerofoil force measurements taken in wind tunnels are; turbulence intensity [103] and length–to–height ratio L/H, of the tunnel test section. An effective means of managing these problems is to ensure that a good wind tunnel of minimal turbulence intensity and a test section length which allows sufficient distance between the tunnel contraction and models under test is used.
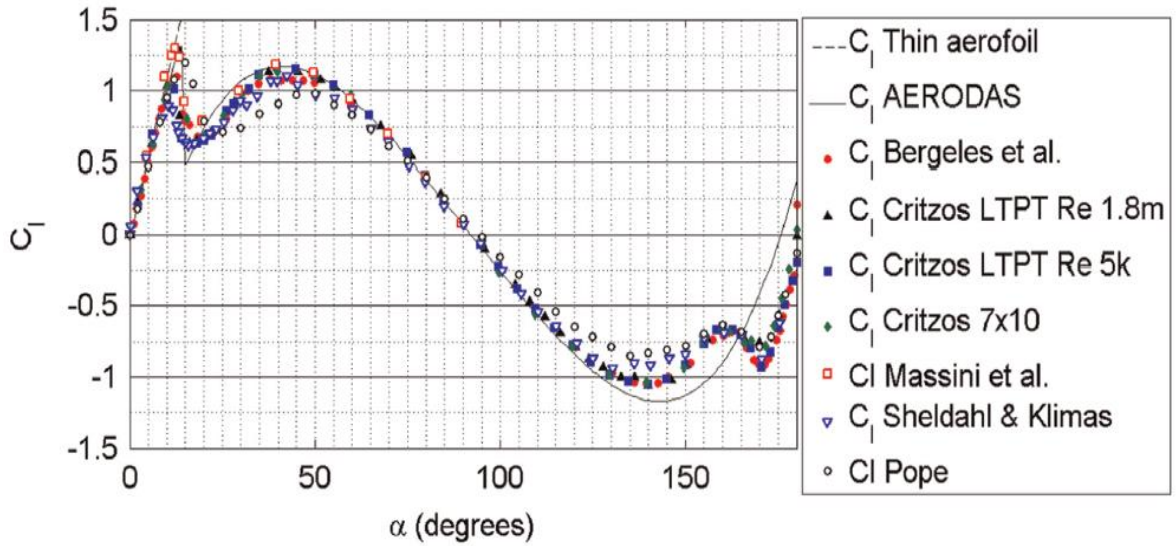
Figure 2.9: Lift coefficient of symmetrical aerofoils by Bergeles et al. [110]**, Critzos et al.** [111]**, Massini et al.** [112]**, Sheldahl and Klimas** [103] **and Pope** [113]**. Extracted from** [116]**.**
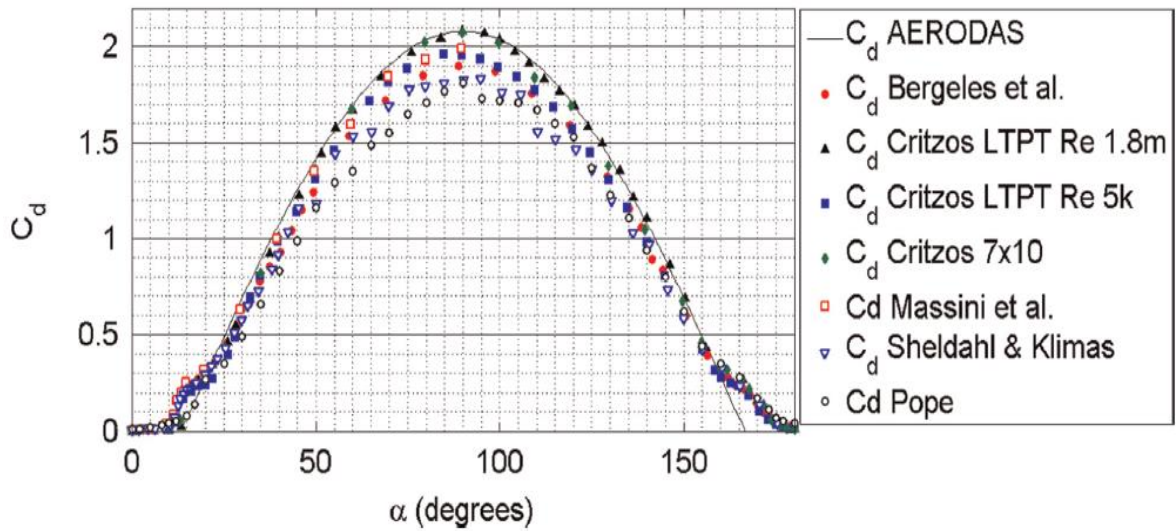
Figure 2.10: Drag coefficient of symmetrical aerofoils by Bergeles et al. [110]**, Critzos et al.** [111]**, Massini et al.** [112]**, Sheldahl and Klimas** [103] **and Pope** [113]**. Extracted from** [116]

Table 2.3: Summary of symmetrical aerofoil data at post-stall. Extracted from [116]

Source	Aerofoil	Post–stall peak		Re (x10^6)	c/h	AR
		C_l	C_d			
Bergeles et al. [110]	NACA0012	1.08	1.90	0.76	0.14	1.70
Critzos et al. LTPT [111]	NACA0012	1.13	2.08	1.80	0.07	6.00
Critzos et al. LTPT [111]	NACA0012	1.15	1.96	0.50	0.07	6.00
Critzos et al. [111] Langley 7 x 10	NACA0012	1.14	2.07	1.36	0.10	7.00
Massini et al. [112]	NACA0012	1.18	1.99	0.96	0.13	2.00
Sheldahl and Klimas [103]	NACA0012	1.10	1.83	0.36	0.07	6.00
Pope [113]	NACA0015	0.98	1.81	1.23	0.17	1.67

CFD study of aerofoils and wind turbines have some key benefits over wind tunnel tests: they are essential in estimating optimum design parameters and performance before fabrication, thus saving time and money; when studying aerofoils, *c/h* ratio of the specified flow domain can be reduced to a feasible extent, so as to eliminate blockage effects. Wind turbine coefficient of power (Cp), starting torque characteristics and other relevant aerodynamic properties for various geometric configurations can be estimated in both 2D and 3D scenarios. A typical CFD package has several turbulence models, each with its strengths and weaknesses with regards to solving a specific flow problem. These models supplement the Navier–Stokes equations with an additional turbulent viscosity term, but differ in their method of computation. Yao et al [119] analysed the influence of turbulence model changes on aerodynamic performance of a three–bladed H type VAWT. The turbulence models used were the standard k–epsilon (k–ε) and Re–Normalisation Group k–epsilon (RNG k–ε). A two dimensional model of the H type VAWT was studied using SIMPLEC algorithm combined with sliding grid methodology in FLUENT. The total torque

extreme value changed periodically while the velocity and pressure gradients were significant around the blades. In another study (Fig. 2.11), Yao et al [120] examined the lift and drag coefficient of a NACA0018 aerofoil under 4 different turbulence models (k–ε, RNG k–ε, shear stress transport SST4, and Reynolds models). The lift coefficient curves of the four turbulence models were much in agreement with the experimental data, while drag coefficient curves differed significantly from the experimental data. The discrepancy in the drag result was attributed to the roughness of the front edge of the aerofoil, flow separation, and other factors. However, the five equations Reynolds stress model (RSM) had best result among the four turbulence models. Such an outcome was expected because, the RSM accounts for the effects of streamline curvature, swirl, rotation, and rapid changes in strain rate in a more rigorous manner than one-equation and two-equation models, it has greater potential to give accurate predictions for complex flows [121].

(a) Lift coefficient
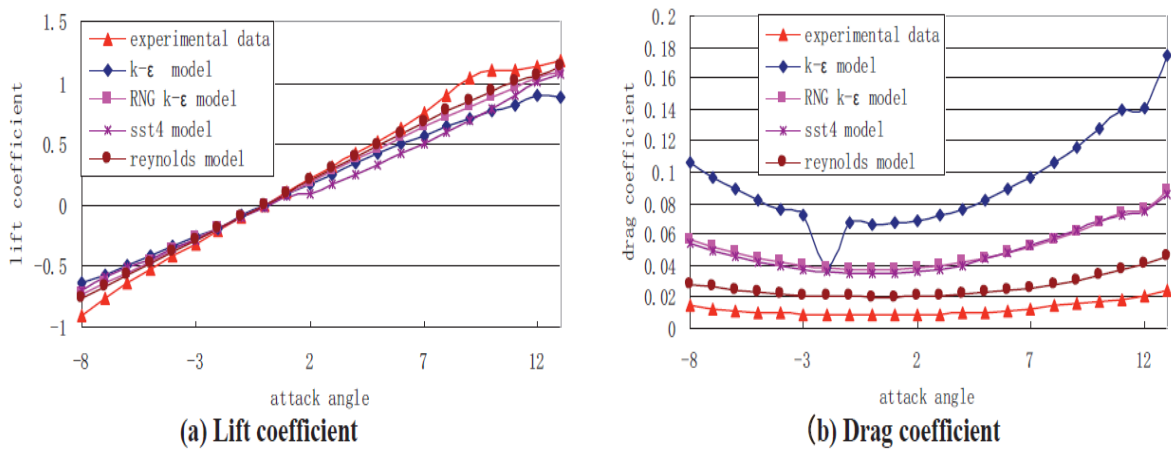
(b) Drag coefficient

Figure 2.11: Variation of lift and drag with angle of attack for different turbulence models [120]**.**

In another study, Howell et al. [122] compared 2D and 3D CFD simulated performance coefficients results of a small scale VAWT with its experimental results over a range of operating conditions. The 3D simulations were shown to be in reasonably good agreement with the experimental measurements. On the other hand, the 2D simulations showed a significant increase in performance compared to the 3D simulations and this was shown to be mainly due to the

presence of the large tip vortices present in the real turbine and the 3D simulations. Debnath et al. [123] carried out a CFD analysis to predict performance characteristics such as power coefficient (C_p), torque coefficient (C_t), and tip speed ratio of a combined three–bucket Savonius and three–bladed Darrieus rotor for various overlap conditions, namely, 16.2%, 20%, 25%, 30%, and 35%. The results were successfully compared with experimental results for all the overlap conditions and show good agreement. The aforementioned studies show that with the right experience and knowledge of the various turbulent models, CFD is a well capable tool for predicting performance characteristics of both aerofoils VAWTs.

2.6 Summary

Key issues pertaining to wind energy in low wind speed conditions and boundary layer control techniques as a means of improving the performance of aerofoils and VAWT have been reviewed in this chapter. Experimental and CFD numerical evidence from the numerous studies of aerofoils considered in this literature review suggests that turbulent boundary layer separation and its associated aerodynamic adverse effects (dynamic stall, loss in turbine power coefficient, etc.) can transpire at low Reynolds number flows. While significant developments have taken place during the last decades in terms of mitigating these occurrences, little have been done with regards to flow control in low wind speed conditions, and application of flow control methods in wind turbines. Thus the author intends to contribute to the study of flow control in airfoil and turbine rotor at low Reynolds number by using passive flow control technique. Evidence from literatures in this chapter suggest that active flow control techniques such as fluidic and plasma actuation can improve the aerodynamic performance of an aerofoil or wind turbine rotor, but a passive control method (used of slots) was chosen for this work because passive control devices are simpler in design, easily applicable and require lesser operating cost than active control devices. The low Reynolds number range (Re=92x10^3 to Re=230x10^3) in this work was chosen in

correlation with the yearly average wind speed in Malaysian cities. Weibull probability density distribution and cumulative frequency of wind speed across cities in Malaysia indicates that, Malaysia is a low wind profile country. Thus, small scale vertical axis wind turbines will be more viable in harnessing wind energy in Malaysia cities because of their low noise levels, simplicity, low maintenance and independence on wind direction.

Chapter 3

3. Experimental Methodology

This chapter addresses a number of activities that are essential to a successful execution of the wind tunnel test. Detailed descriptions of the low–speed wind tunnel lift and drag measurement techniques, data acquisition, wall correction, error analysis, equipment, smoke visualization and data reduction procedures are presented. The wind tunnel test procedure in this work involves the use of a force balance to obtain the lift and drag forces of the aerofoils. Fig. 3.1 shows a representation of the data flow in the wind tunnel test.
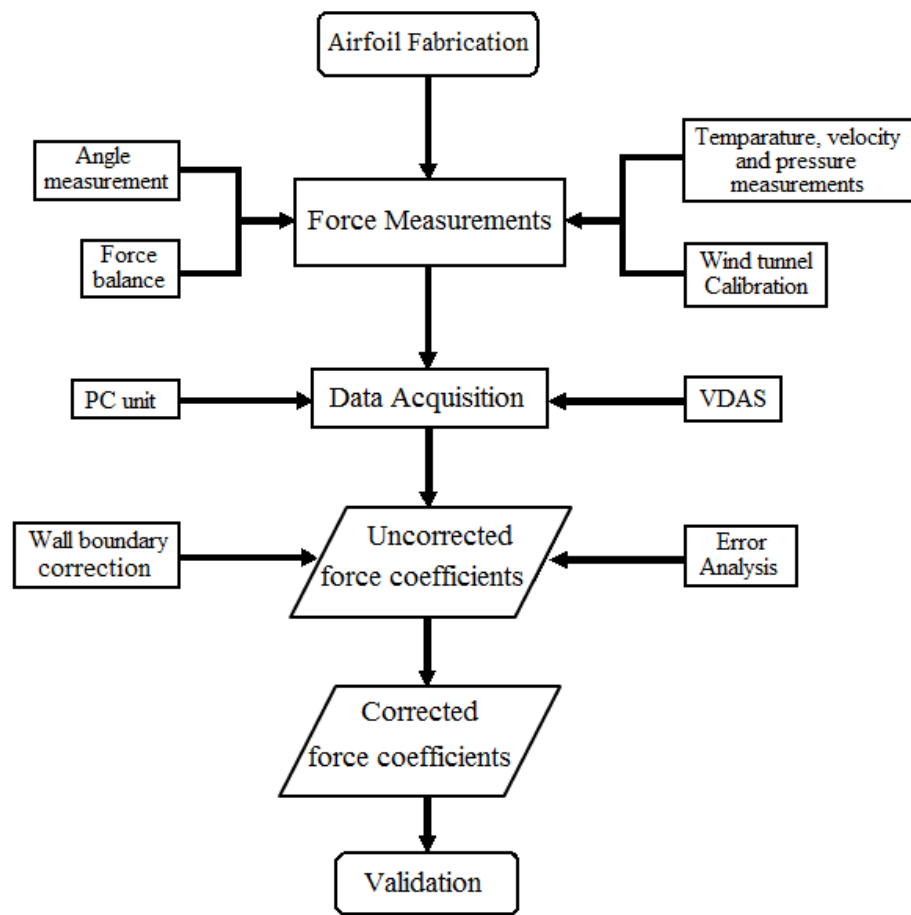
Figure 3.1: Wind tunnel test methodology flow chart.

Smoke visualization was also carried out on both the pain and slotted NACA0018 aerofoils. All experiments were performed in the University of Nottingham Malaysia Campus (UNMC) Department of Mechanical Engineering subsonic wind tunnel facility. The purpose of the experiment is to extract and compare lift and drag data of both plain and slotted NACA0018 aerofoil at low Reynolds number (92×10^3, 138×10^3, 184×10^3 and 230×10^3) and angle of attack between 0° to 20°. The entire test results are presented and discussed in chapter 5.

3.1 Aerofoil Selection and Fabrication

The system of designating aerofoils varies according to standards. In the first half of the 20th century, an empirical approach was used in the design of early aerofoils. The aerofoils were made based on the builder's personal discretion and past experience with known shapes and experimentation with modifications to those shapes. The earliest standardized and reliable aerofoils were developed by National Advisory Committee for Aeronautics (NACA). However, the contemporary approach to aerofoil design is analytically based. There are three series of NACA aerofoils; four–digit, five–digit and six–digit aerofoils. The aerofoil used in this work is the NACA0018. This aerofoil belongs to the first family of aerofoils in the NACA four–digit series. The first digit stands for the maximum camber (m) in percentage of the chord (aerofoil length), the second indicates the position of the maximum camber (p) in tenths of chord, and the last two numbers represents the maximum thickness (t) of the aerofoil in fractional percentage of the chord length. Therefore '00' indicates no camber, '18' indicates that the aerofoil has an 18% thickness to chord length ratio, thus the NACA0018 aerofoil is a symmetrical aerofoil.

The equations for a NACA four-digit symmetric aerofoil profile is:

$$\pm \, y_t = 5tc \left(0.2969 \sqrt{\frac{x}{c}} - 0.1260 \, \frac{x}{c} - 0.3516 \left(\frac{x}{c} \right)^2 + 0.2843 \left(\frac{x}{c} \right)^3 - 0.1015 \left(\frac{x}{c} \right)^4 \right) \qquad (3\text{-}1)$$

where c is the chord length, x is the position along the chord from 0 to c, y_t is the half thickness

36

at a given value of x (centreline to surface), and t is the maximum thickness as a fraction of the chord in percentage.

Equation 3.1 above gives the shape of the aerofoil with the thickness distribution above (+) and below (–) the chord line when the value of t is substituted into it for each x coordinate. The coordinates of the upper aerofoil surface (x_U, y_U) and the lower aerofoil surface (x_L, y_L) are expressed as; $x_U = x_L = x,$ $\quad y_U = +y_t,$ $\quad and \quad y_L = -y_t.$

The thinner and more popular NACA four–digit series aerofoil sections such as NACA0012 and NACA0015 have been studied more extensively compared to the NACA0018 aerofoil, due to data availability and wide range of application. Nevertheless, thicker aerofoils are renowned for their good aerodynamic performance at low Reynold number; they are capable of withstanding large centrifugal loads and can achieve higher stall angles [124]. Furthermore, when utilized as a wind turbine rotor, symmetric aerofoils are capable of increasing the maximum power output and operating range (tip speed ratio range) than non-symmetrical aerofoils [125], due to delay of stall activities on the rotor. With regard to the fabrication process of the slotted aerofoil, the NACA0018 has a thickness to chord ratio that gives the model a good structural strength, and allows for easy handling and slot creation. Therefore, for these reasons the NACA0018 aerofoil was selected for this work.

3.1.1 Spanwise Slotted NACA0018 Aerofoil

The slotted aerofoil model is a 300mm span by 250mm chord (c) aerofoil fabricated from high–density Styrofoam and conforms to the NACA 0018 profile. An initial total of 4 aerofoils were manufactured; one Plain and 3 slotted aerofoils consisting of span–length slots. On each slotted aerofoil, the exit of the slot channel on the top and bottom surface were located at X=15% (0.15c), X=45% (0.45c) and X=70% (0.7c) respectively, relative to the aerofoil leading edge. For the sake of convenience, the aerofoil with slot at X=15% was named LS (Leading edge Slot),

likewise the other two with slots at X=45% and X=70% are named MS (Mid slot) and TS (Trailing edge Slot). These assigned names will be used to represent the slotted aerofoils throughout this report. The slots were strategically positioned before and after the aerofoil maximum thickness (x/c=18%) to effectively deliver air into the separation zone which grows progressively towards the leading edge as AoA increases. During fabrication, X=15% and X=70% were the closest locations the slots could be placed to the leading and trailing edges respectively without compromising the structural integrity of the model. The slots all had uniform width (2% of the chord), and were continuous in the spanwise direction. A 2% chord (5mm) slot width was deliberately chosen so as to minimize the maximum drag [67] and reduce 3D effects [79]. All slots exiting from the top and bottom surfaces of the aerofoils are inclined to an angle of 55° with respect to the chord line (Fig. 3.2). The slot layout was inspired by the arrangement of gills in a fish, and their function is intended to mimics the ram ventilation in a scombrid fish, which on its forward momentum opens its mouth and gills to allow water flow continuously through without pumping—an action that helps in delaying boundary layer separation [126]. A pictorial illustration of the slotted NACA0018 aerofoil with all slots in their designated location is shown in Fig 3.2.
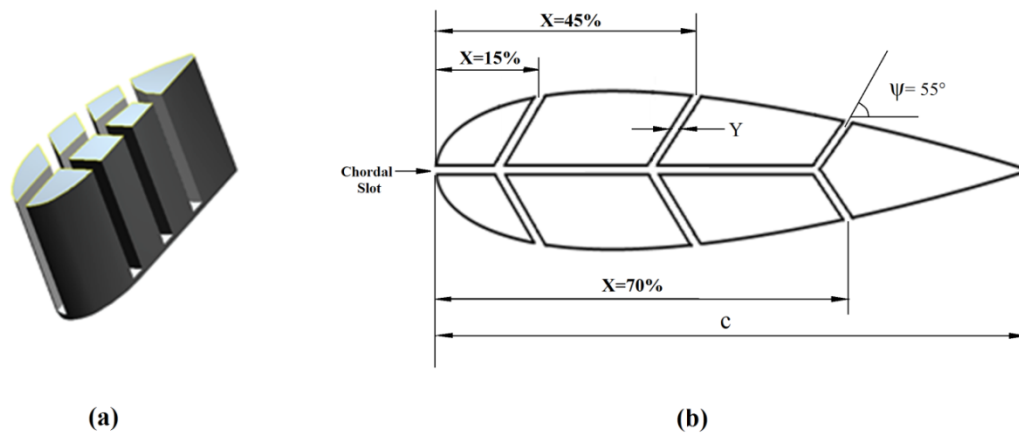
Figure 3.2: The Slotted NACA 0018 Aerofoil (a) 3D Cross-section of aerofoil with all slots in place. (b) Slot geometric characteristics (X: Slot location, Y: Slot width ψ: Angle between slot axis and chord.

The manufacturing process of the aerofoils is explained in Appendix A. Before Styrofoam was selected as the aerofoil material, other materials like aluminium and plastic were considered. The main factors that influenced the selection of Styrofoam was its; weight, malleability, and cost. An initial trial model (plane aerofoil) was made from an aluminium block, but it was very heavy and way out of shape (Fig 3.3). Consequently, for the purpose of precision and fine surface finishing, the use of CNC machine and 3D printer was explored. However, after a detailed cost inquiry, they were abandoned due to high production cost.

Figure 3.3: Aluminium Aerofoil.

The roughness of an aerofoil can sometimes be detrimental or beneficial to aerofoil performance data in so many ways. But the degree of their influence depends on their size relative to the boundary layer thickness, Reynolds number and aerofoil type [122]. Roughness in this case refers to surface irregularities like bumps and scratches that can be felt by touch. The effect of surface roughness was not studied in this work, but considerable effort was taken to smoothen out the surface protuberances resulting from the manufacturing process. The aerofoils were smoothened by hand with the aid of a fine sand paper, in order to achieve a fine surface finish with consistent surface roughness. Extreme caution was taken to avoid altering the shape of the aerofoil during sanding. Finally, a thin plastic lamination sheet (0.2mm thick) was glued onto the entire sanded

surface, to produce a smooth surface finish and for protection of the aerofoil. An image of the fabricated aerofoils in their finished state is shown in Fig 3.4.
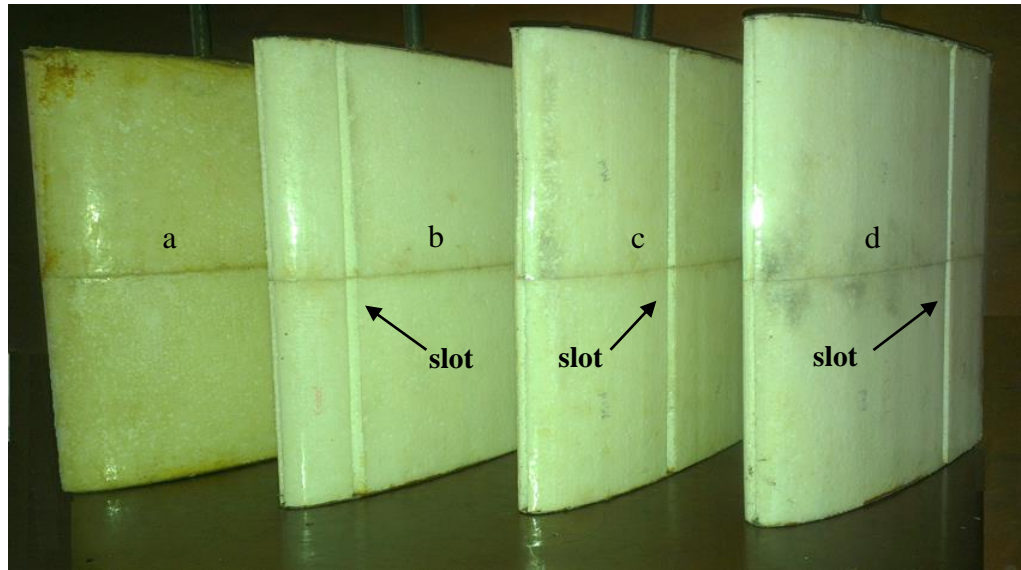
Figure 3.4: The fabricated NACA0018 aerofoils; (a) Plain, (b) leading edge slot (LS), (c) mid slot (MS), and (d) trailing edge slot (TS) aerofoils in their right order from left to right.

3.2 Experimental Set-up and Force Measurement

The wind tunnel test facility is a closed working-section, open-return suction type. It is supported on a tubular steel framework that encourages easy mobility of the apparatus. The test-section wind speed is variable up to a maximum of 36 m/s via a three-phase AC motor connected to a six-bladed axial fan. During operation, air enters the tunnel from the surrounding through an aerodynamically designed inlet cone that accelerates the air in a linear manner through a flow straightener at the test section inlet. The air flows through the test section, and exits it via a metallic mesh into a diffuser. From the diffuser, it goes through the axial fan and the silencer and finally, back into the surrounding. The mesh protects the fan from damage by loose objects. A schematic diagram of the subsonic wind tunnel is shown in Fig 3.5. The speed of the axial fan (and therefore the air velocity in the working section) is controlled by an electronic drive control

in the separate control and instrumentation unit. Details of the wind tunnel technical data are summarised in Table A-1 (in appendix A).
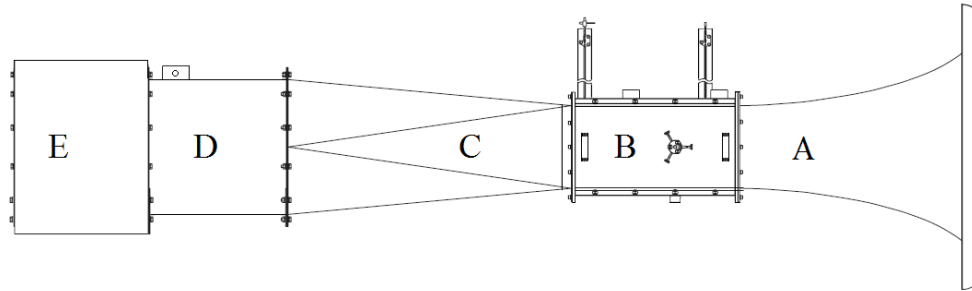
Inlet Cone (A)   Working Section (B)   Diffuser (C)   Axial Fan (D)   Silencer (E)

Figure 3.5: Schematic diagram of the subsonic wind Tunnel.

The working section of the wind tunnel is a 360 mm x 305 mm x 600 mm rectangular acrylic box with aluminium frame. The side walls in the working section are removable with special holders to support a variety of tunnel models. The test is 2D; therefore before testing commences, the model is placed horizontally in the tunnel in such a way that it completely spans the width of the test section, however a gap of about 2 mm is left at both ends so as to allow free movement of the model. The model is attached to the balance system by inserting the models' 12mm supporting shaft through the hole in the middle of the balance, which was already fastened to the side of the tunnel working section. Then the model is set to 0° AoA and clamped to the balance assembly by means of thumbscrews (refer to Fig 3.6). Thereafter, the protractor is fitted to the model shaft, set to 0° and tightened with the protractor clamp screws. At this point the angle of attack can be altered to any desired value by unscrewing the thumbscrews and rotating the shaft to the desired angle on the protractor. Upon adjusting to the desired angle, the thumbscrews are re-tightened. The other end of the model was set free to move with no connection that could compromise the load reading.

3.1.1 Lift and Drag Force Measurement and Data Acquisition

Lift and drag forces were measured from 0° to 20° angle of attack (2° intervals) at 92×10^3, 138×10^3, 184×10^3 and 230×10^3 chord Reynolds number. The Reynolds number range was chosen in correlation with the wind speed range in Malaysia cities, where the mean monthly wind speed in is between 1m/s to 5m/s [31][7]. The plain aerofoil was initially tested with the intention of using it as a baseline for the rest of the slotted aerofoils. The aerofoils are set-up at negative angles of attack in the subsonic wind tunnel because of the mechanical layout of the single force balance, and the need to eliminate the effects of gravity in the system. Since a symmetric aerofoil is employed, by definition the characteristics at positive angles of attack should match the curves at negative angles [127]. Angle of attack was only increased; therefore hysteresis effects were not investigated. Lift and drag measurement procedures were relatively similar, both were measured by means of a balance system to an uncertainty of ±0.2 N. The only difference is that for drag measurement, the force balance is required by design to be rotated 90 degree in the clockwise direction from an initial upright position which was used for lift measurement (Fig. 3.6).
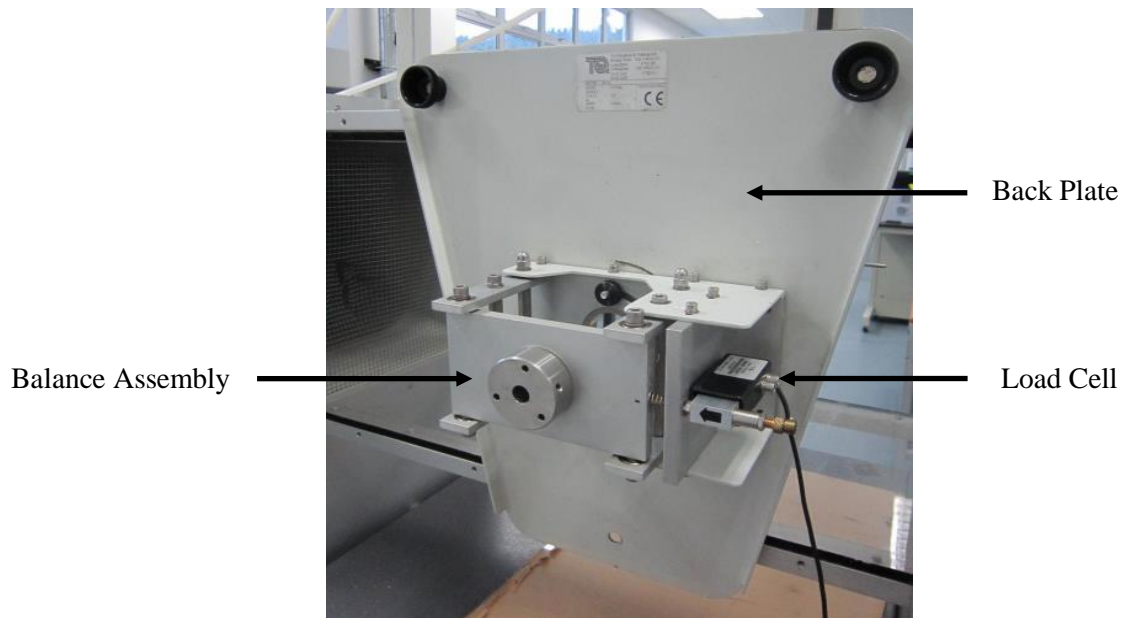
Figure 3.6: Single Force Balance in Drag Measurement Position.

The force balance used in this case is a single component balance, which implies that at any instance it can only measure either a lift force or a drag force. The balance is made up of two parts:

1. The Balance Assembly (Fig.3.6) is an articulated parallelogram (a simple hinged rod mechanism) which is linked to a load cell. The parallelogram resists bending moments, so that only the force (not the moment) on the model is transmitted to the load cell.

2. The display unit Fig A.4 in (in Appendix A) displays the force measured by the load cell.

The force balance, through the load cell was connected to a Data acquisition system (VDAS-Versatile Data Acquisition System) on the control unit of the wind tunnel which allows force measurements to be displayed on a PC, tabulated, and exported into any spread sheet package for further processing. Before the commencement of force measurement, the display unit which is connected to the load cell is allowed to stabilize for 5 minutes, and then the zero button is press and held for at least four seconds to re-zero the force reading. The forces were recorded at each reference velocity and angle of attack at a rate of 1 sample per second for 30sec after a period of settling. At low wind tunnel speeds, there exists a small time-dependent fluctuation in the wind speed at the moment the fan is switched on, caused by inertia of both the fan drive system and the surrounding air. Therefore, the velocity is allowed to stabilize in the working section before readings were taken. The data acquisition process was digitised, and the following quantities; differential pressure, lift, drag and velocity were measured simultaneously. The VDAS acquires data by converting an electrical generated signal such as a voltage from a device known as a transducer. This system offers many advantages over traditional (manual) methods because it enables high speed and real-time data collection, and eliminates errors that arise from manually inputting data to a computer. The raw data appeared tabulated in VDAS software were exported as HTML file format and later saved and analysed in excel. This automated data acquisition system of obtaining wind velocity from the pitot-static tubes employs the same basic principles as

manual computation: The differential pressure transducer measures the dynamic pressure ΔP_1 by computing the difference between the stagnation pressure and static pressure of the incoming wind from the Pitot tube at the section inlet. According to Bernoulli's equation, the wind velocity at the point of measurement was calculated as follows;

$$V = \sqrt{\frac{2 \times \Delta P_1}{\rho}} \tag{3.2}$$

The VDAS calculated the air density ρ_{atm} using the input ambient temperature T at the time of measurement, obtained from an external thermometer (accurate to within 0.5°). From the ideal gas law;

$$\rho_{atm} = \frac{P_{atm}}{RT} \tag{3.3}$$

where P_{atm} is the pressure at T and R is the ideal gas constant

The dynamic viscosity μ of air at the input ambient temperature T was calculated using the Sutherland viscosity law [128] [129] expressed as;

$$\mu = \mu_{ref} \left(\frac{T}{T_{ref}} \right)^{3/2} \left(\frac{T_{ref} + S}{T + S} \right) \tag{3.5}$$

where T_{ref} is a reference temperature, μ_{ref} is the viscosity at the T_{ref} reference temperature and S is the Sutherland temperature (a constant) for air. A graphic illustration of the versatile data acquisition system is shown in Fig 3.7.
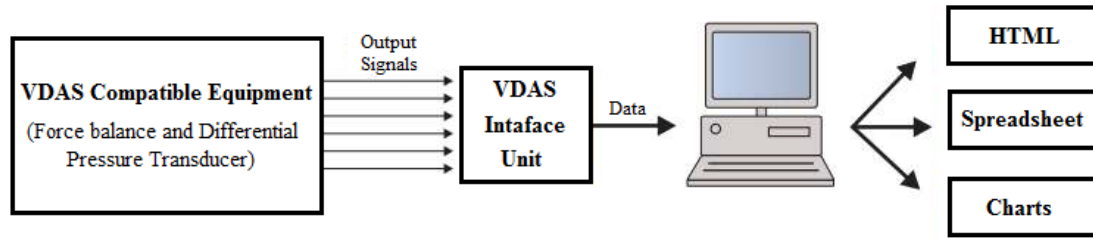
Figure 3.7: VDAS system.

3.3 Uncertainty Analysis in Force Measurement

Uncertainties in force measurements in a wind tunnel test are caused by numerous factors such as velocity fluctuation, model deformation under load, roughness, turbulence intensity, equipment inherent uncertainties, etc. [130]. The total uncertainty in the measured forces (lift and drag) is a combination of random and systemic uncertainties. Random uncertainty which is also known as precision was computed using standard statistical tools. Systemic errors on the other hand are more difficult to detect because they are caused by uncontrollable factors [117]. A large amount of data was taken for the entire work, leading to a variation of uncertainty between successive data collection points. The fluctuating forces recorded at a specific velocity (Reynolds number) and angle of attack was averaged to obtain a representative value (the sample mean). This fluctuation is the largest source of error in the load readings taken from the force balance. Equation (3.6) below was applied to obtain the limits of the standard error in the measured forces.

$$\bar{x} - \frac{s}{\sqrt{n}} < x < \bar{x} + \frac{s}{\sqrt{n}} \quad \text{for } n \geq 30 \tag{3.6}$$

Where n is the sample size, $\bar{x}$ and s are the sample mean and standard deviation respectively.

The error in the system tends to increase with increase in velocity and angle of attack due to vibration of the model, resulting from an increase in blockage and aerodynamic load. From

calculations, the error in the system between 0° to 10° AoA was approximately 2.1%. But in the post stall region where the stall phenomena and blockage increased, the uncertainty between repeated observations went as high as 7.5%. However, the average uncertainty limit within the entire range of AoA was 4.5%. Fig.3.8 displays the scattered plot and frequency distribution histogram of lift collected at 10° AoA and Reynolds number of 230×10^3. The spread of the lift force appears to be within limits that could be assumed a normal distribution.
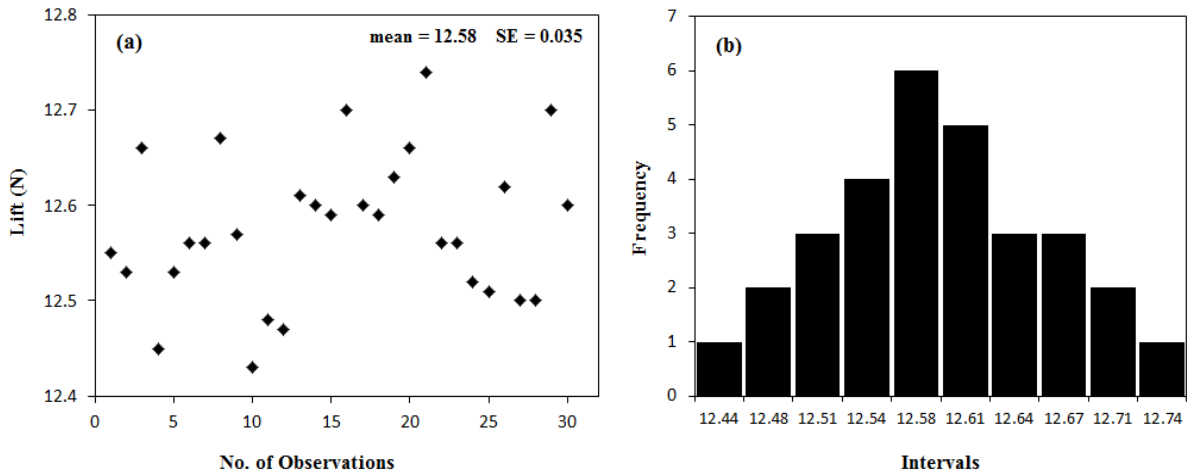
Figure 3.8: (a) A lift force scattered plots and (b) Frequency distribution histogram of lift forces for the Plain NACA 0018 aerofoil for 30 samples at 10° angle of attack and Re=230x10³.

Note - Refer to Appendix A.2 and A.6 for calibration procedures and turbulence intensity test of the wind tunnel test section respectively.

3.4 Wall Boundary Interference and Correction of Measurements

The tunnel constriction at the inlet, volume of the test model, and the proximity of the test section walls to the model causes some abnormalities that impact on the corresponding flow-field in such a way that the measured forces cannot be directly extrapolated to free stream conditions [131][132]. Hence the following sources of inaccuracy manifest; solid and wake blockage, streamline curvature, and buoyancy drag if the tunnel has a negative longitudinal static pressure gradient. Consequently, these effects lead to an increase in the velocity, lift, and drag of the

measured data. Standard wind tunnel wall correction methods for 2D test in a close test section were applied to the measured data in accordance with literature [117][133][134][135].

Solid Blockage

The presence of a model in the test section leads to a decrease in the effective area through which the air can flow and by continuity and Bernoulli's equation increases the velocity of the air as it flows over the model [136][117][132].

Solid blockage factor:
$$\varepsilon_{sb} = \frac{K_1 \cdot V_m}{C^{3/2}} \tag{3.7}$$

where $K_1 = 0.74$ for a wing spanning the test section horizontally and V_m is the volume of the aerofoil. C is the working section area; but if greater accuracy is desired, the section area is computed with the boundary layer displacement thickness subtracted around the perimeter of the section exit [137]. For boundary layer displacement calculation, refer to Appendix A.5.

$$V_m = 0.7 * t * c_{airfoil} * b \tag{3.8}$$

where t and b represents the aerofoil thickness and span respectively.

The approximation of the aerofoil model volume is only appropriate at a 0° angle of attack [136]. For any other angle of attack, the aerofoil thickness becomes;

$$t = c * \sin(\alpha) + 0.045 \tag{3.9}$$

0.045 is the thickness of the NACA0018 aerofoil due to its chord length of 0.25m. Taking into account the angle of attack, the aerofoil chord becomes [136][137];

$$c_{airfoil} = c * \cos(\alpha) \tag{3.10}$$

Wake Blockage

Wake blockage arises from decreased velocity within the wake of the aerofoil. The effect of wake blockage is proportional to the wake size and the measured drag force on the model [117][133].

Wake blockage: $\quad\quad\quad\quad \varepsilon_{wb} = \dfrac{c}{2h} C_{du}$ $\quad\quad\quad\quad\quad\quad\quad\quad\quad\quad\quad\quad\quad\quad$ (3.11)

Where c is the aerofoil length, C_{du} is the uncorrected 2D drag coefficient and h is the height of the test section.

Note: The velocity outside the wake must be larger than the freestream speed for a constant mass flowrate within the test section. By definition, the total blockage coefficient is the sum of the wake blockage and solid blockage [138].

Total blockage: $\quad\quad\quad\quad \varepsilon = \varepsilon_{sb} + \varepsilon_{wb}$ $\quad\quad\quad\quad\quad\quad\quad\quad\quad\quad\quad\quad\quad\quad$ (3.12)

Buoyancy

This arises as a result of negative static pressure along the axis of an empty test section, due to thickening of the wall boundary layer as the flow progresses towards the section exit. Buoyancy artificially increases the drag, thus it is subtracted from the measured drag [117]. The buoyancy drag D_B is expressed as;

$$D_B = \frac{6h^2}{\pi} \Lambda \sigma p'$$ $\quad\quad\quad\quad\quad\quad\quad\quad\quad\quad\quad\quad\quad\quad$ (3.13)

where p' is the static pressure gradient along the test section (see Appendix A.5 for p' calculation), Λ and σ are the aerofoil shape factor and streamline curvature factor respectively.

$$\sigma = \frac{\pi^2}{48} \left(\frac{c}{h} \right)^2$$ $\quad\quad\quad\quad\quad\quad\quad\quad\quad\quad\quad\quad\quad\quad$ (3.14)

Streamline Curvature

This refers to the alteration of the expected streamline curvature of the flow over a test model due to the presence of the top and bottom walls of a wind tunnel test section. The model appears to have more camber than it actually has, causing an artificial increase in lift [117]. The change in the lift coefficient due to streamline curvature effect is given as;

$$\Delta C_{lsc} = -2\pi \left(\frac{\pi}{2} \right) \sigma C_l = \sigma C_l \tag{3.15}$$

The complete low-speed wall boundary corrections for velocity, lift coefficient and drag coefficient for the two-dimensional wind tunnel testing are summarised below;

$$V = V_u (1 + \varepsilon) \tag{3.16}$$

$$C_l = C_{lu} (1 - \sigma - 2\varepsilon) \tag{3.17}$$

$$C_{d0} = C_{d0u} (1 - 3\varepsilon_{sb} - 2\varepsilon_{wb}) \tag{3.18}$$

where V_u, C_{lu} and C_{du} are the uncorrected free stream velocity, 2D lift and drag coefficient respectively.

Lift and drag forces were corrected in their non-dimensional forms to account for blockage, buoyancy, as well as streamline curvature effects. Overall, the corrections to the force measurements typically range from an average of 10% in C_d and 18% in C_l between 0° to 10° AoA to 41% and 55% respectively at 20° AoA. This difference between the corrected and uncorrected forces was chiefly attributed to high blockage effect due to the high chord length to section height ratio (c/h=0.694). Fig. 3.9 shows one of the slotted NACA0018 aerofoils in the wind tunnel test section, in a horizontal position.
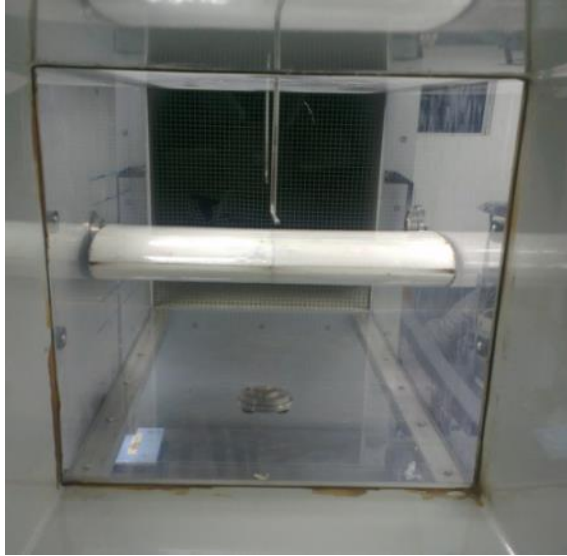
Figure 3.9: Aerofoil in test section.

3.5 Smoke Visualization Apparatus and Set up procedure

The use of smoke to study flow patterns or streamlines around and over a model in a wind tunnel is one of the oldest and reliable flow visualization techniques. Smoke visualization was used in this work to further understand the reason for the disparity in the lift and drag forces (of the plain and slotted aerofoils) extracted from the wind tunnel tests at both pre–stall and post–stall AoAs. In addition, it was used to study the effect of the slots on the flow field around the slotted NACA0018 aerofoil. Smoke visualization can be classified mainly into two forms, namely; smoke wire and smoke generator techniques. For this work, the smoke generator method was chosen over the smoke–wire method because studies have shown that the latter is constrained to lower wind tunnel velocities [139]. For smoke–wire method, the applied oil coat on the wire which vaporises (due to electrically controlled resistive heating) to produce smoke lines, which rapidly loses attachment from the smoke wire at the test section inlet when the wind tunnel velocity exceeds 4m/s. Thus the smoke duration is shortened and it becomes difficult for the observer to adequately monitor or capture a fully developed flow field [140]. A velocity of 4m/s

is lower than the least reference chord Reynolds number in this work. However, in a state of improved lighting, visualization by smoke generator can be extended to about 9m/s which in this experiment represent a chord Reynolds number of 138×10^3. But it would not produce clear smoke filaments like smoke wires would. Similar results are obtained by using either fog and vapour [141].

The smoke visualization was performed in the same subsonic wind tunnel, that was used for the lift and drag force measurement. The apparatus used were; 1300watt Viconcept smoke generator (which consists of a smoke oil reservoir, heat exchanger and an external CO_2 gas cylinder), an Olympus Tough TG–4 digital camera (lens specification: 4x wide optical zoom 4.5–18.0mm 1:2.0–4.9) and a lamp for lighting. To activate the smoke visualization process; the wind tunnel fan was switched on and set to the reference velocity using the control nob on the control unit, then the valve of the cylinder was opened and the paraffin mineral oil was propelled into the heat exchanger by the CO_2 gas (any inert gas should be adequate). In the heat exchanger, the oil is vapourized and delivered as a dense white, non-toxic smoke into the test section via a custom smoke rake (made from 2 inch PVC pipes) placed just outside the inlet of the test section. The smoke follows the air current generated by the wind tunnel fan, allowing the observer to visualize the flow. After 2 minutes, the valve was closed, but the fan was allowed to run for a while in order to eject the smoke from the test section in preparation for the next test. The quality of the observed or photographed smoke depends on the property and position of the illumination system, usually high contrast is required in order to enhance smoke visibility. The reflection of the images on the acrylic test section wall due to the black background on the farther test section wall opposite the digital camera poses a major problem. Several tests were performed in a dark room with various lighting arrangement and sources with the aim of producing clearer images. However, a single 18W light source from a florescence lamp position over the top of the test section in combination with daylight gave sufficient illumination and produced the best images

without reflection. The camera was positioned about 0.8m from the test section window. The angle and elevation of the camera with respect to the aerofoil was adjusted to give 2D view of the flow. Fig. 3.10 shows the smoke visualization set-up with the test section, aerofoil, lighting and camera arrangement.
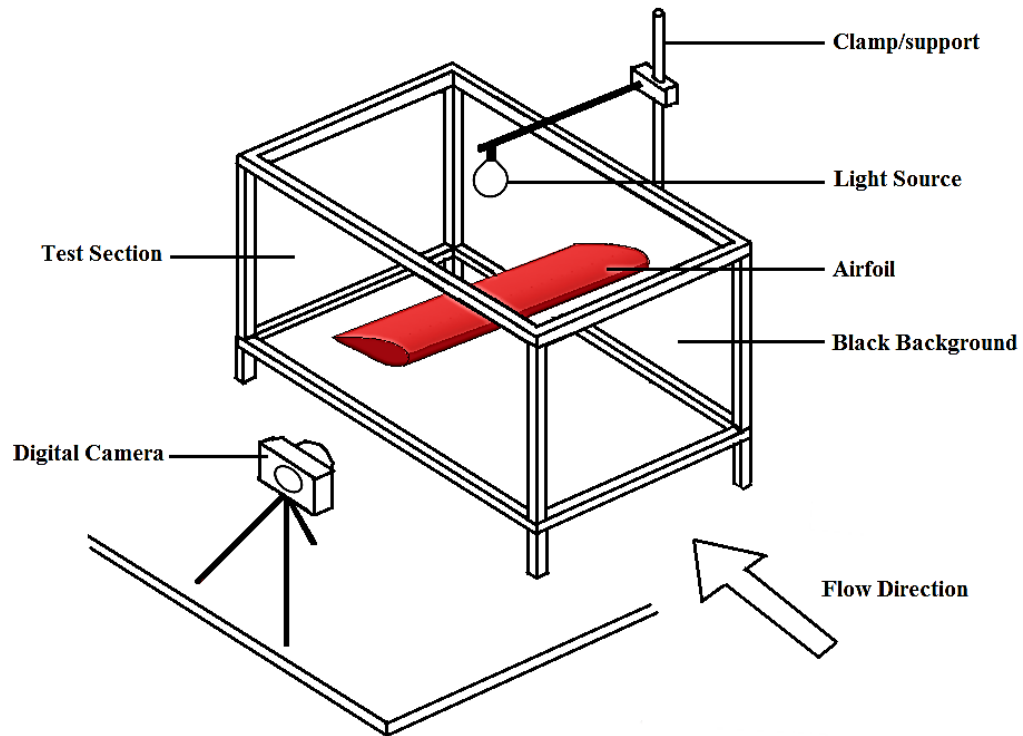
Figure 3.10: Smoke Visualization Set-up

3.6 Summary

The experimental methodology and set-up adopted in this work has been discussed in this chapter. A pictorial illustration in the form of a flow chat was made to summarize the entire experimental procedure involved from aerofoil fabrication to result validation. The average standard error in the force measurement within the entire range of AoA was 4.5%. Systemic errors were checked by wall interference correction of measurements, and calibration of the wind tunnel before commencement of measurements. The procedures adopted in this chapter were in

accordance with standard practices in 2D wind tunnel experiments involving the use of a force balance.

Chapter 4

4. Numerical Methodology

The accuracy and effectiveness of numerical methods in resolving flow problems have been well established. However, numerical study of passive flow control devices on aerofoils presents new levels of challenge to CFD modelling proficiency. Often a pragmatic approach is needed regarding the level of detail required in achieving acceptable results. Computational fluid dynamics (CFD) techniques are often used when the nature of the study in question makes it too difficult or expensive to conduct an experimental investigation. An example of such a case is the study of the effect of the slot parameters on the NACA0018 aerofoil performance in this work. CFD method was adopted due to the tedious effort that would be required to fabricate and test numerous slotted NACA0018 aerofoils of different slot geometric parameters (multiple slot positions, slot width, span–length slot and slot slope). This chapter expounds, the numerical (CFD) methodology involving the slotted NACA0018 aerofoils in low Reynolds number flow. Four aerofoils were initially studied before parametric alterations were done to their slot geometry. These aerofoils were; the Plane, LS, MS, and TS aerofoils. However, the Plain and MS aerofoils (see Fig 4.1) were randomly selected for the purpose of illustrating the numerical method. Therefore the discussion and diagrams in this chapter are based on these two aerofoils.

Figure 4.1: 2D Section of Plane and Mid slot (MS) NACA0018 aerofoils.

4.1 Computational Scheme

Simulation in 3D is known for delivering a more detailed and accurate representation of the complexity in transition and turbulent flow problems. It also enables visualization of the interaction between fluid flow and the model. These advantages mentioned, together with the continuous increase in computational capability, means that 2D numerical calculations is becoming a lesser choice for simulating complex flow problems [142]. Most often, the use of 3D analysis is justifiable if the main objective is to study a specific problem for a particular application or to expand the level of understanding beyond the limits of 2D study. However, 2D analyses are essential in summarizing conceptual study and fundamental behaviour of flow; they are relatively faster, support frugal computer power usage and permit a wide range of tests and analyses that broaden understanding [143]. Therefore, since one of the aims of this work is to expansively analyse the effects of the NACA0018 aerofoil slot parameters (such as slot position, width and slope) on its aerodynamic performance over a specified range of low Reynolds number and AoA, a 2D steady state, incompressible turbulent flow simulation is considered adequate.

Numerical Methodology flow chart

Geometry construction
- Construction of 2D geometry to represent aerofoil flow domain.
- Assignment boundary names

Mesh generation
- Discretization of flow domain.
- Aerofoil wall boundary refinement.

Setup and solution
- Boundary conditions are specified in FLUENT.
- Solve governing equations with boundary conditions.

Validation
- Specific set of results were validated with their corresponding experimental results.

Post processing
- Extraction and analysis of desired flow properties (e.g lift, drag etc.).

Figure 4.2 Numerical methodology flow chart.

The entire computational procedure was carried out in ANSYS 16.0 workbench, and the process required five steps; Geometry construction, Mesh generation, Setup and Solution, Post processing and Result validation. The first three steps have an immense impact on the accuracy and convergence of the numerical calculation.

4.2 Flow Domain and Mesh Description

Creating the geometry and flow domain is always the first step in modelling a flow problem. The 2D NACA0018 aerofoil coordinates consisting of 150 points (Appendix B) was imported into the ANSYS Design Modeler where tools such as sketch, line, Boolean, and other surface operations were used to create slots (at required locations), and complete the flow domain. The coordinates obtained was for an open trailing–edge type aerofoil. Therefore, the two loose end points at the trailing–edge were linked by changing their x and y coordinates to 1 and 0 respectively. The coordinates of the 2D aerofoil were proportional to the chord length, as shown in figure 4.3. Figure 4.4 shows the flow domain around the aerofoil. A four quadrant C-type grid topology consisting of a semicircle upstream and a square downstream (trailing edge) was used to represent the flow domain. The tip of the aerofoil trailing edge was located at the centre of the semicircle.
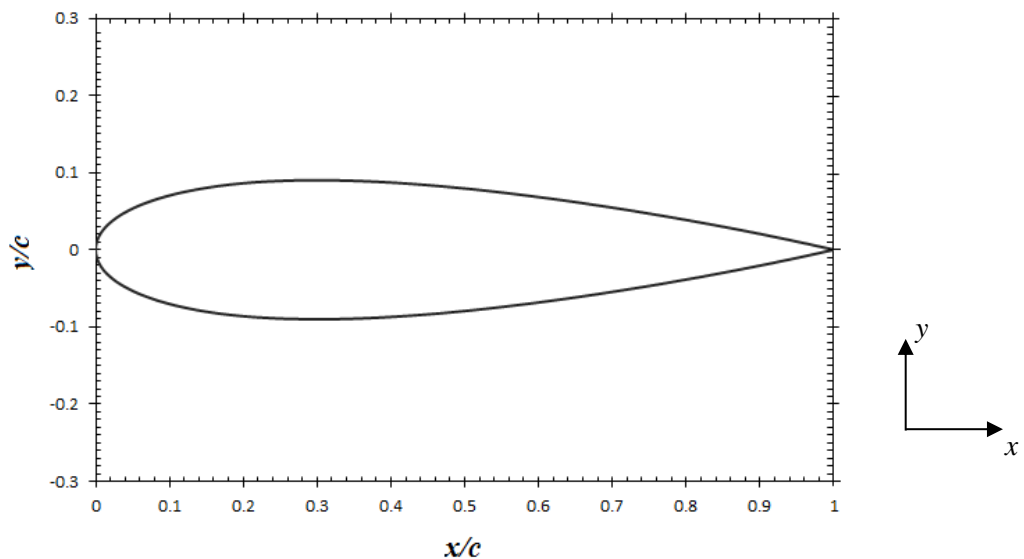
Figure 4.3 NACA0018 aerofoil geometry.
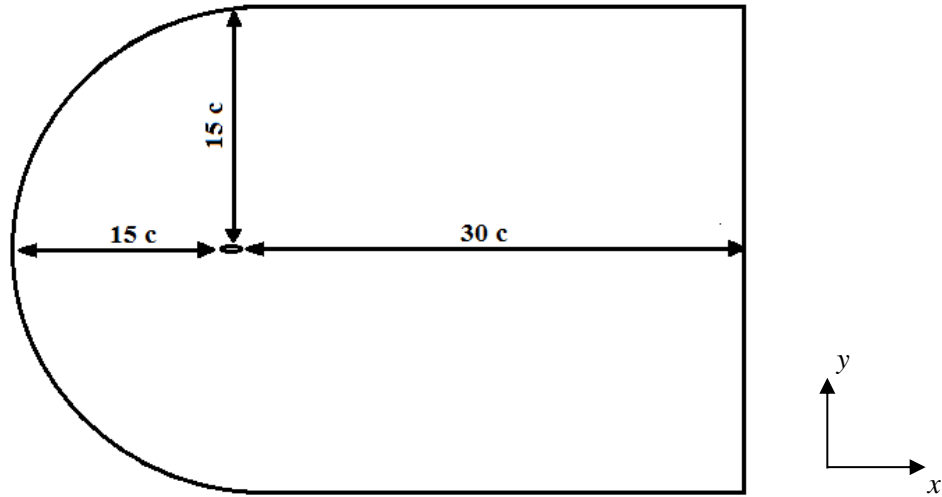
Figure 4.4 Flow domain.

The Boundaries of the computational domain around the aerofoils were positioned far enough so as to avoid them influencing the simulation results at the aerofoil boundary. The dimensions of the flow domain was denoted in units of chord length; the domain extends 15 chords upstream to 30 chords downstream and the upper and lower boundary extends 15 chords away from the aerofoil profile.
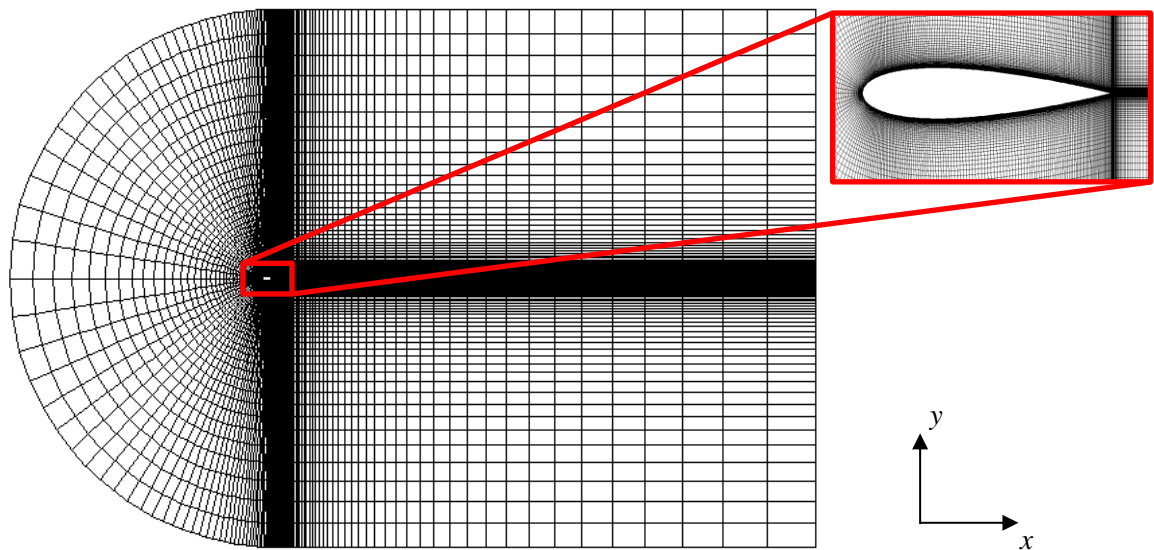
Figure 4.5: Meshed Domain.

The flow domain was discretized into a grid (Figure 4.5). The grid (mesh) generation involves defining the structure and topology (in this case, a four quadrant C-type topology) and then generating a grid on that topology. A good grid is important as it helps in achieving a converged solution that takes into consideration key parameters in a simulation. It also has a direct influence on the speed and accuracy of the CFD solution [121]. Grid generation was done with the ANSYS Mesher in the work bench. Mapped scheme quadrilateral structured mesh elements were used for the entire flow domain (slots inclusive). Before grid independency study, 200 elements were modeled on the surface of the aerofoils (both for plain and slotted), and in stream–wise direction; the wake was modeled with 150 cells, 100 cells upstream and normal to the aerofoil surface, thus leading to a cell count of 28,000 in the domain. In order to adequately capture the pressure gradients, velocity gradients and flow separation near the aerofoil boundary, the mesh was created by placing sufficient inflation cells (so that $y^+ \approx 1$) within the boundary layer. Edge sizing with smooth transition cell growth rate of 1.1 was employed to cluster more cells around the aerofoil wall boundary. Hence the meshed domain becomes progressively coarser from the aerofoil towards the far-boundary (since the flow gradients approach zero far-field). The boundary refinement changes the wall y^+ (y-plus) value, which is a non-dimensional value that represents the thickness of first cell from the wall. It determines whether the influences in the wall-adjacent cells are laminar or turbulent, hence indicating the region of the turbulent boundary layer resolved [144]. Based on theoretical and experimental derivations, the near-wall region in a turbulent boundary layer can be divided into viscous sub-layer ($y^+ \leq 5$), buffer layer ($5 < y^+ \leq 30$), log-law region ($30 < y^+ \leq 500$), and outer layer [54][145].

$$y^+ = \frac{u_\tau y}{v} \qquad\qquad (4.6)$$

$$u_\tau = \sqrt{\frac{\tau_w}{\rho}}$$

(4.7)

where u_τ is the friction velocity, y represents the height of the grid to wall, v is the kinematic viscosity, τ_w denotes the wall shear stress, and ρ is the air density.

Adopting a suitable inflation mesh for the geometry strongly depends on the choice of the turbulence model and the flow behaviour. For the k-ω SST model the wall-functions perform particularly well in the viscous and buffer sublayer. Therefore the wall y^+ range in the order of 1 ($y^+ \approx 1$) was adopted for all aerofoils [121] (see figure 4.6(a)). After a successful grid formulation, the mesh quality was checked and the geometry was transferred to FLUENT to solve the flow problem using the designated flow equations. Thereafter, the y-plus value is examined and modified if necessary through the spacing option in the pre-mesh parameters in ANSYS Mesher. Fig.4.7 below shows the mesh domain of both the Plain and MS NACA0018 aerofoil.

(a) wall y^+ plot

(b) Standard wall
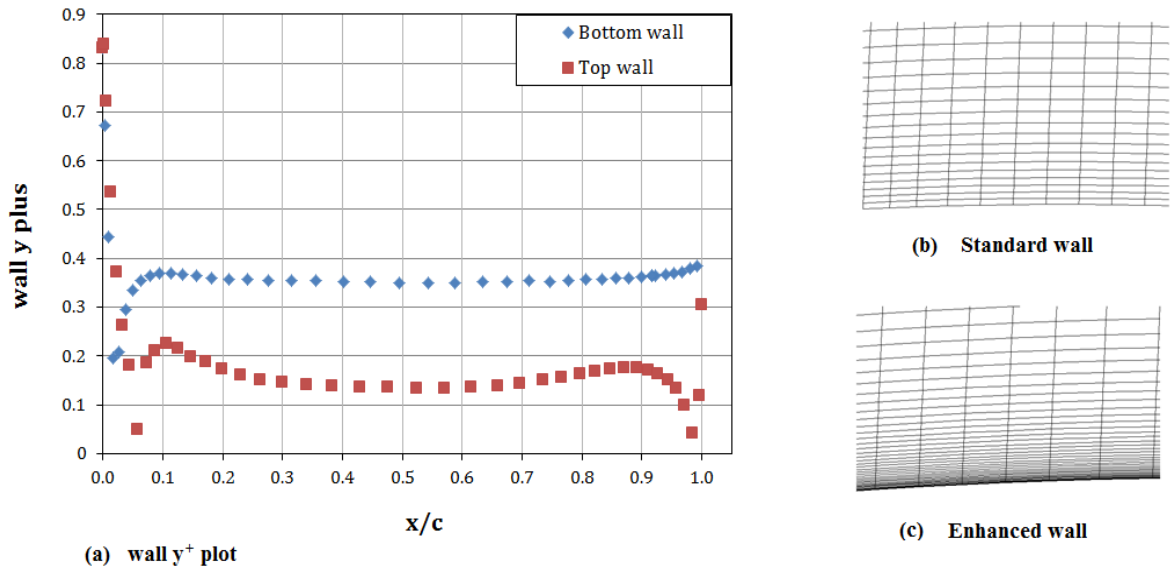
(c) Enhanced wall

Figure 4.6: y–plus and grid on Plain aerofoil wall (a) y–plus value at 10° and Re=230x10³ (b) standard wall (c) enhanced wall.
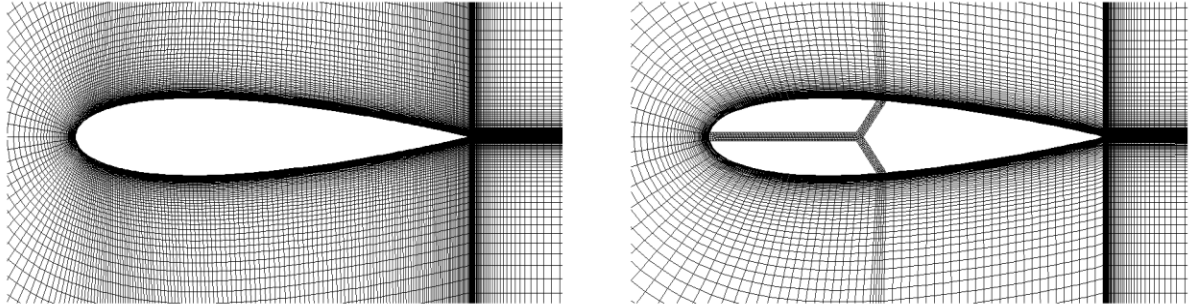
Figure 4.7: Enlarged mesh of the Plain and MS NACA0018 aerofoil.

4.2 Setup and Solution

The commercial FLUENT 16 software in ANSYS workbench 16 was adopted to perform the RANS CFD simulations. FLUENT is a finite volume method based solver which offers a wide range of applications in practical flow problems such as, turbo machinery, heat transfer, etc. In FLUENT, the Reynolds Averaging Navier Stokes (RANS) shear stress (SST) k–ω turbulence model was preferred over Detached Eddy Simulation (DES) and Large Eddy Simulation (LES) models mainly because of the low computational effort required in using it compared to the others. The k–ω SST turbulence model is a very popular and reliable RANS turbulence model that has been validated in numerous numerical studies of aerofoils [146][147]. Its capability to resolve complex aerodynamic flows associated with passive flow control over aerofoil has been praised by researchers [148]. The k–ω SST model possesses two extra transport equations which accounts for the turbulent properties and transition over geometries in complex aerodynamic flow conditions. It is accurate and robust for a wide range of boundary layer flows with large adverse pressure gradient and flow separations.

4.2.1   Governing Equations

Navier–Stokes equations are fundamental equations that describe transported quantities in a moving fluid. These equations arise when Newton's second law is applied to fluid motion, together with the assumption that the fluid is a continuum. The fluctuations of momentum and

60

energy in a velocity field can lead to variation of other transported quantities. Most often, these fluctuations are of a very small scale and high frequency, thus resulting in huge computational expense for practical engineering calculations. To remedy this situation, the instantaneous quantities in the equations are time–averaged to remove the small scales, leading to a modified set of computationally less expensive equations with additional unknown variables. Thus the two-dimensional steady state incompressible flow equations for conservation of mass and momentum were solved with zero gravity and body force terms using the Reynolds-averaged Navier-Stokes (RANS) equations. The momentum and continuity equations are summarized as follows;

Continuity equation:

$$\frac{\partial u}{\partial x_i}\left(\rho u_i\right)=0 \tag{4.1}$$

Momentum equation:

$$\frac{\partial u}{\partial x_j}\left(\overline{\rho u_i u_j}\right)=-\frac{\partial \overline{P}}{\partial x_i}+\frac{\partial}{\partial x_j}\left[\mu\left(\frac{\partial \overline{u}_i}{\partial x_j}+\frac{\partial \overline{u}_j}{\partial x_i}-\frac{2}{3}\delta_{ij}\frac{\partial \overline{u}_i}{\partial x_j}\right)\right]+\frac{\partial}{\partial x_j}\left(-\overline{\rho u_i' u_j'}\right) \tag{4.2}$$

In Equations (4.1) and (4.2), $\overline{P}$ represents the mean pressure, ρ is the mean density, μ is the molecular viscosity, δ_{ij} is the Kronecker delta function, and $-\overline{\rho u_i' u_j'}$ is the Reynolds stresses. The Reynolds stresses are additional unknowns introduced during the time-averaging process; hence they must be resolved in terms of known quantities using the turbulence model of choice in order to close the system of governing equations. A common method is to employ the Boussinesq hypothesis to relate the Reynolds stresses to the mean velocity gradients within the flow. Therefore the Reynolds stresses are expressed as:

$$-\overline{\rho u_i' u_j'} = \mu_t\left(\frac{\partial \overline{u}_i}{\partial x_j}+\frac{\partial \overline{u}_j}{\partial x_i}\right)-\frac{2}{3}\left(\rho k+\mu\frac{\partial \overline{u}_i}{\partial x_i}\right)\delta_{ij} \tag{4.3}$$

In Equation (4.3) above, μ_t is the turbulent (or eddy) viscosity and k is the turbulent kinetic energy. For a two–equation turbulence model such as SST k–ω, the turbulent viscosity is computed through the solution of two additional transport equations for the turbulent kinetic energy k, and the specific dissipation rate, ω.

4.2.2   SST k-omega Turbulence Model

The shear stress transport (SST) k–ω turbulence model was used to solve the turbulence equations. Basically, two turbulence models are merged in a numerically effective manner: the standard k–ω model formulation is used in the near–wall region and in the fully turbulent far-field region the k–ε model is kept due to the free-stream independence [121]. The SST k–ω differs from the standard k–ω model in the sense that it incorporates a damped cross-diffusion derivative term in the equation. Also the turbulent viscosity definition is modified to account for the transport of the turbulent shear stress. The transport equations for SST k–ω model are:

specific turbulent kinetic energy k (m^2 s^{-2});

$$\frac{\partial}{\partial t}(\rho k) + \frac{\partial}{\partial x_j}(\rho k u_j) = P_k - \beta^* k\omega + \frac{\partial}{\partial x_j}\left((\mu + \sigma_\kappa \mu_t)\frac{\partial k}{\partial x_j}\right) \tag{4.4}$$

specific turbulent dissipation rate ω (s^{-1});

$$\frac{\partial}{\partial t}(\rho \omega) + \frac{\partial}{\partial x_j}(\rho \omega u_j) = \alpha \rho S^2 - \beta \omega^2 + \frac{\partial}{\partial x_j}\left((\mu + \sigma_\omega \mu_t)\frac{\partial \omega}{\partial x_j}\right) + 2(1 - F_1)\sigma_{\omega 2}\frac{\rho}{\omega}\frac{\partial k}{\partial x_i}\frac{\partial \omega}{\partial x_i} \tag{4.5}$$

The two terms on the left hand side of the Eqs. (4.4) and (4.5) relate to the rate of change of k or ω and the transport of k or ω by convection, respectively. The three terms on the right hand side represent the transport of k or ω by turbulent diffusion, the rate of production of k or ω and the rate of dissipation of k or ω, in this order. The last term in the ω equation (4.5) signifies the

cross-diffusion, which arises as a result of the transformation of the ε equation into an ω equation.

4.2.3 Solver Settings

In the solution set–up, the steady–state option was selected in order to eliminate time marching in the flow equations. The flow domain was specified as fluid (air), and a constant density and dynamic viscosity of 1.16kg/m^3 and 1.8861Pa.s respectively were applied. Both assigned fluid properties correspond with the ambient temperature (T=31°C) during the wind tunnel testing. Since the flow was assumed incompressible, the pressure based solver was used, together with the SIMPLE implicit segregated algorithm for pressure-velocity coupling. A cell–centred control volume space discretization approach was used in solving the flow equations in the fluid domain. The Green–Gauss Node–Based and the PRESTO! pressure Interpolation method were adopted for solution gradient and cell–face pressures calculations. Second–order upwind interpolation schemes were employed for momentum, turbulent kinetic energy and specific dissipation rate to achieve second–order accurate solutions at the cell faces. The lift and drag coefficients as well as the scaled residuals of all variables were monitored to ensure adequate convergence. Fig. 4.8(a) shows the residuals below the specified tolerance (10^{-6}) while 4.8(b) shows the lift coefficient of the Plain aerofoil at 10° 138x10^3 Reynolds number. An adequate number of iteration was specified to enable convergence. Thus convergence was achieved when residuals decreased below the specified tolerance (10^{-6}). However, at higher incidence, the flow around the aerofoil becomes unstable due to vortex shedding in its wake causing fluctuation of results and convergence difficulty. The pressure–velocity coupling algorithm was enabled to address the unsteadiness in order to obtain a solution. To facilitate faster computation, the simulation was performed in parallel mode with 4 processors on a desktop system with an Intel^R Core^{TM} i7 quad core processor with 8 GB of RAM.
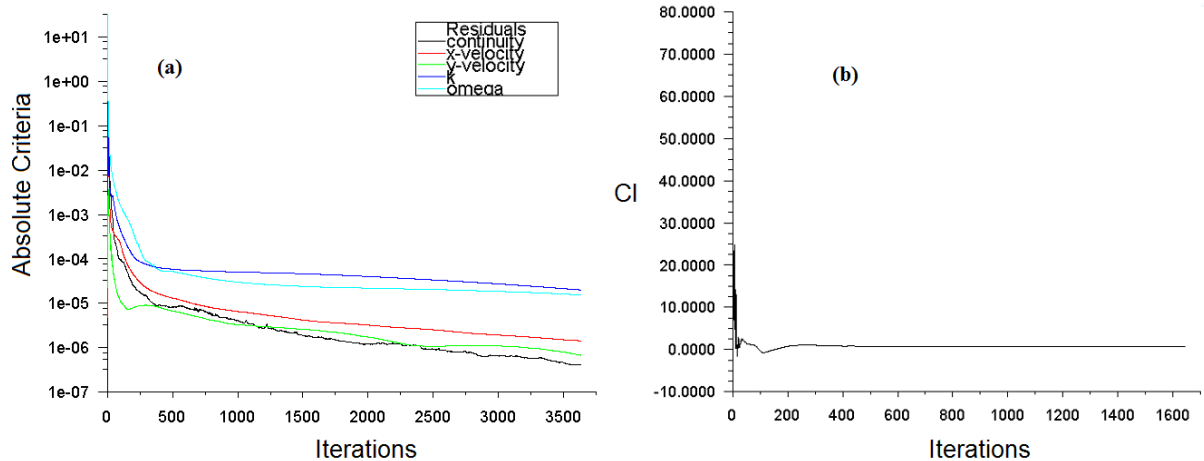
Figure 4.8: Scaled residuals and Lift coefficient monitor for the Plain Aerofoil at 10° AoA and 138x10³ Reynolds number (a) Residual plots show when the residual values have decreased below specified tolerance b) Lift coefficient monitor.

4.2.4 Boundary conditions

The boundary conditions were kept similar to that of the experiments, thus air was the flow medium with a density and viscosity which correspond to an ambient temperature T of 31°C. Fig. 4.6 shows the flow domain with specified boundary names. The boundary conditions adopted are illustrated below;

- The far–field semicircle together with the horizontal square edges of the flow domain was specified as "inlet", and the velocity boundary condition with magnitude and component values was set to achieve the flow Reynolds number and angle of attack adopted in the experiment. Likewise, the inlet turbulent specifications were set at a turbulent intensity of 0.81%, which also corresponds to the turbulence characteristics of the low speed wind tunnel used in the experiment.

- Pressure outlet boundary condition was used for the outlet boundary which on the domain is the right vertical edge of the square. Both the inlet and outlet were given ambient pressure condition of 101325 Pa.

64

- A no–slip boundary condition was assigned for the aerofoil surface (top and bottom) and slot walls of the aerofoils.
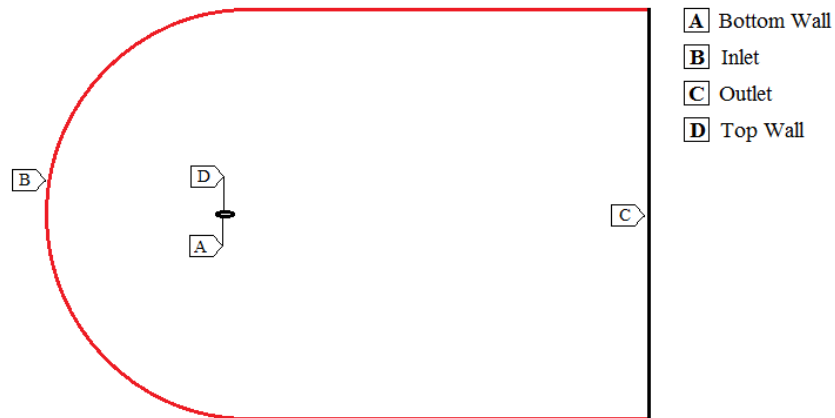
Figure 4.9: Boundary Conditions.

4.2.5 Grid Independence Study

It is always essential to investigate the effect of the mesh size on numerical solutions [149] because the complex flow field in a flow problem is accurately resolved when more nodes are used. A grid independent solution is achieved by increasing the number of nodes in the domain until the mesh is sufficiently fine so that further refinement has a negligible influence on the solution. Using additional nodes increases the computational memory and time required to complete numerical simulations. Therefore, in problems involving large domain and flow separation, a good mesh is usually a compromise between desired accuracy and computational cost. By keeping the flow domain size fixed, the grid independency study was carried out on the numerical result of the plain aerofoil at Re=230x10^3 and incidence angle $\alpha = 12°$ for four different grid sizes. The grid sizes were 28,000, 45,000, 64,000 and 7,200 elements, while the choice of angle of attack and Reynold number was arbitrary. The grid independence analysis was done only for the plain aerofoil because the same domain size was used for the numerical study of

the slotted aerofoils, therefore the mesh sizes was approximately the same [148]. A summary of the grid independency study is shown in Table 4.1.

Table 4.1: Mesh independency test at 10° and Re=123x10^3.

No. of Elements	Lift Coefficient C_L	Drag Coefficient C_D
28,000	0.784	0.052
45,000	0.852	0.047
64,000	0.888	0.043
72,000	0.882	0.043

The result from Table 4.1 shows that refinement of the grid size from 28,000 to 45,000 cells led to a significant difference in the C_L and C_D values (8.7% and 10.6% respectively). Further increase in grid size to 64,000, and later to 72,000 resulted in a decrease in the difference between the successive C_L and C_D values; a mere 0.7% and 1.2% difference in C_L and C_D respectively between 64,000 and 72,000 grid size was noted. Consequently, within this range of grid sizes the solution can be considered grid independent due to the negligible difference in the force coefficients. Giving the grid independency test result, the grid size of 64,000 cells was adopted for the sake of reducing the calculation time.

4.3 Summary

In this chapter the procedures involved in setting up the numerical flow problem in ANSYS 16.0 have been explained. The 2D flow domain around the NACA0018 aerofoil was represented by a four–quadrant C–type grid topology, and on its boundaries and that of the aerofoil the boundary conditions were assigned accordingly. Furthermore, the mesh was generated and a grid independency test was carried out at Re=230x10^3 and incidence angle $\alpha = 12°$ for four different grid sizes. The governing equations as well as the chosen viscous model (SST k-omega) with regards to steady state conditions were discussed. Overall, the numerical procedures discussed in

this chapter were applied to both the Plain and slotted NACA0018 aerofoils. The results from the

numerical simulations and their validation will be discussed in the next chapter.

Chapter 5

5. Results and Discussion

Over the past decades, a great deal of research effort has been put into optimising aerofoil performance. In other words, researchers attempt to control boundary layer separation with the intention of achieving one or both of the following primary objectives; increase lift or reduce drag. The process of realizing these objectives has led to advancements in the field of low Reynolds number flow research such as in; aerofoil design, aerofoil selection, aerofoil optimization, wind energy and unmanned aerial vehicles (UAVs). In this chapter, low wind speed aerodynamic performance data of the slotted NACA0018 aerofoils in the form of lift and drag coefficient curves was presented and analysed. The stationary slots on the aerofoil were employed as a passive flow control device to mitigate local separation, and aerodynamic losses especially at high AoAs where they are more obvious. The entire work presented in this chapter was categorized into experimental and numerical subsections. The experimental section dealt with analysis of the results from the 2D wind tunnel test discussed in chapter 3. On the other hand, the numerical section which is an extension of chapter 4 was devoted to the use of 2D CFD calculations to validate the experimental results and also to provide additional information and explanation regarding the physics of the flow around the aerofoils and within the slots. In addition, further slot parametric study to investigate the aerodynamic performance and flow control capability of a variety of slot configurations on the NACA0018 aerofoil was performed, with the aim of identifying an optimal slot configuration. In both experimental and numerical categories, the plain NACA0018 aerofoil was used as a reference or baseline to evaluate the performance of each slotted aerofoil investigated.

5.1 Experimental Set-up Validation

In order to confirm the validity of the present experimental set–up, the results obtained was compared with two other published studies on the same aerofoil. The present lift coefficient curve of the plain NACA0018 aerofoil at Re=230x10^3 is compared with those published by Daniele [137] and Sheldahl and Klimas [103]. In the case of Daniele, the lift and drag coefficient data were acquired by means of a force balance at Re=230x10^3. The lift and drag coefficient data of Sheldahl and Klimas were acquired by means of a balance and wake survey method respectively at Re=300x10^3. The Reynolds number differed but it is still within an acceptable range (Re=10^5).
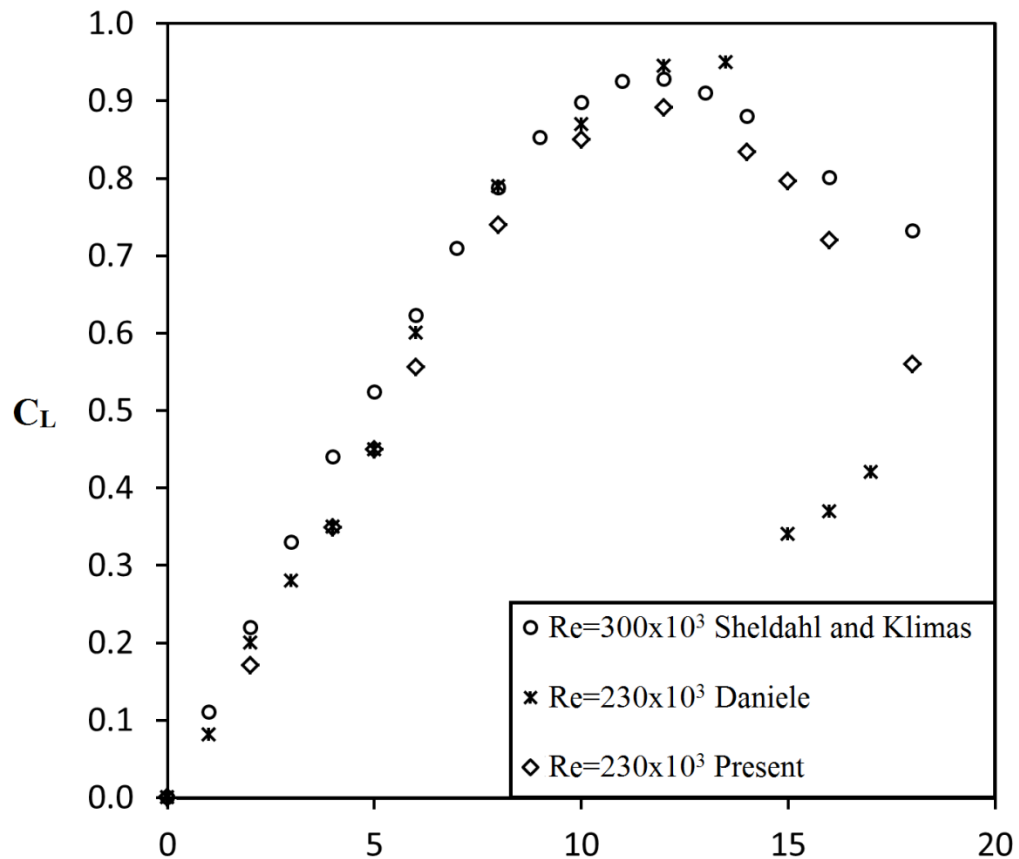
Figure 5.1: Comparison of lift coefficient of plain NACA 0018 with previous published Data.
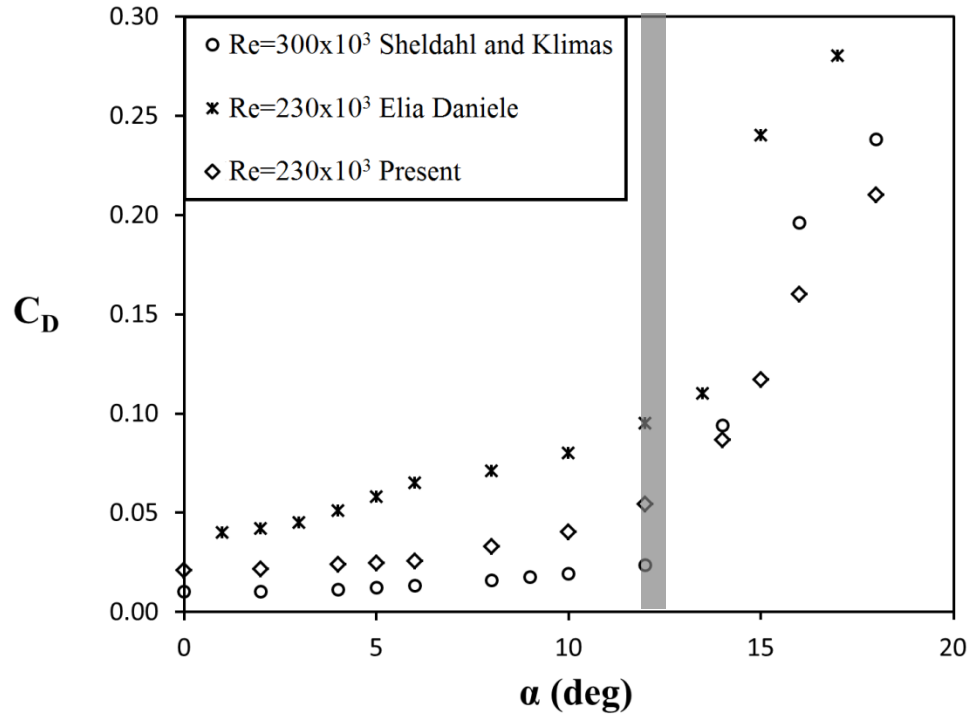
Figure 5.2: Comparison of drag coefficient of plain NACA 0018 with previous published Data.

Fig. 5.1 shows the validation of the present lift coefficient with reference works. It is clear that the lift coefficients obtained by Daniele and Sheldahl are consistent with the present case. There exists an increase in lift between 0° to 12° in the present case as well as in theirs. The maximum lift coefficient for the present measurements as well as that of Sheldahl was at 12° AoA, but that of Daniele was at 14° AoA. There is a slight misfit in the lift coefficient curves between $0° \leq \alpha \leq 12°$; an average difference of 4% was noticed. Also, there is an obvious difference between the present lift coefficients values and the reference cases in the post stall range ($14° \leq \alpha \leq 20°$). These discrepancies may be attributed to variations in experimental conditions, secondary separation, model mounting technique and arrangement or turbulence intensity in the wind tunnel. These occurrences are well known to significantly affect flow development over an aerofoil as AoA increases low Reynold number flow [150][151]. A comparison of the drag coefficient of the present case and the referenced works is shown in Fig. 5.2. The trend of the drag distribution curves and the point of onset of stall ($\alpha \approx 12°$) were consistent. The difference in the drag

coefficient values between the present case and the referenced works was as a result of the difference in chord length to test section height (*c/h*), and the length of the test section in each case. A higher *c/h* leads to high wake blockage in the test suction which subsequently raises the measured drag coefficient. A short test section length on the other hand, causes negative static pressure and high buoyancy drag D_B in the test section [117].

5.2 Experimental investigation of the effect of slot location

In the process of selecting an aerofoil among the slotted aerofoils fabricated, the aerofoil with an operational output that is more likely to satisfy design requirements is chosen for optimization while the less satisfactory ones are discarded. This process is carried out by examining the lift and drag coefficient curves of the respective aerofoils. The aerodynamic performance of the slotted aerofoil is affected by the position of the slot (X). In this section, the influence of this parameter (slot position) was determined by fixing the slot width (Y) at 2.0% of the chord length and slot slope (ψ) at 55°. The analysis is carried out on 3 slot locations; X=15%, X=45% and X=70%. Lift and drag forces of the aerofoils were extracted from the balance at 92×10^3, 138×10^3, 184×10^3 and 230×10^3 chord Reynolds numbers between 0° to 20° angles of attack at 2° intervals with additional data taken at 5° and 10. The corresponding force coefficients were computed using Eqn (5.1) and Eqn (5.2) together with the aerofoil geometric parameters and air properties (refer to Table 5.1) at different angles of attack and Reynolds number

$$C_L = \frac{L}{\frac{1}{2}\rho V_\infty^2 bc} \tag{5.1}$$

$$C_D = \frac{D}{\frac{1}{2}\rho V_\infty^2 bc} \tag{5.2}$$

Where ρ is the mass density of air, V_∞ is the free stream velocity, *b* and *c* the span and chord of

the aerofoil respectively. L and D represent the measured lift and drag forces, while C_L and C_D are their corresponding lift and drag coefficients.

Table 5.1: Aerofoil geometric property and air property

Geometric property of Aerofoil		Property of Air	
Geometric Property	Dimension	Air Property	Value
Chord of Aerofoil	0.25m	Density	1.16 kg/m^3
Span	0.30m	Viscosity	1.896 Pa.s
Slot Size	0.05m x 0.30m	Temperature	31°C
Maximum Thickness	18% x 0.25	Reynolds Number	92x10^3 to 230x10^3

Fig. 5.3 shows a 2D section of the plain and slotted aerofoils with their respective slot positions. With the aid of lift coefficient (C_L) and drag coefficient (C_d) characteristics curves an observation of the effect of slot location on the aerodynamic characteristics of the NACA 0018 aerofoil was given. Also an investigation of the relationship between the maximum lift coefficient and Reynolds number was carried out. Fig. 5.4 below shows the direction of the wind, lift (L) and drag (D) forces with their corresponding tangential and normal components.
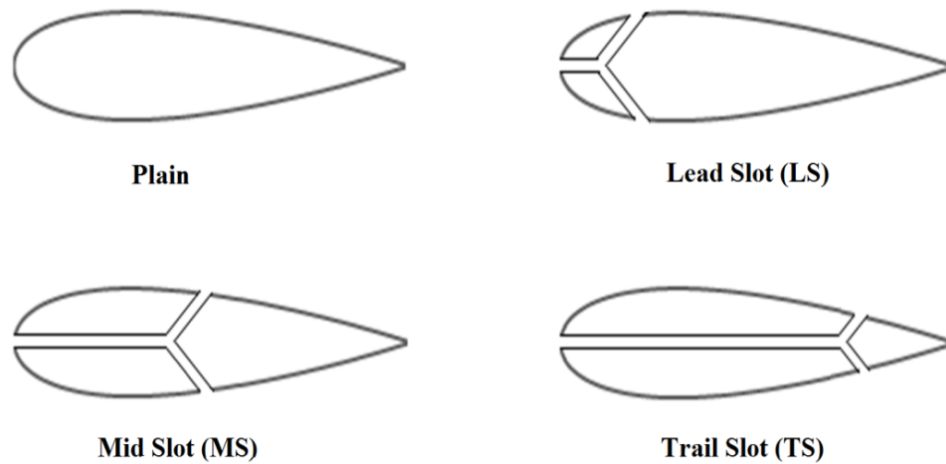
Figure 5.3: 2D section of experimental studied; Plain, leading edge slot (LS), mid slot (MS), and trailing edge slot (TS) NACA0018 aerofoils.
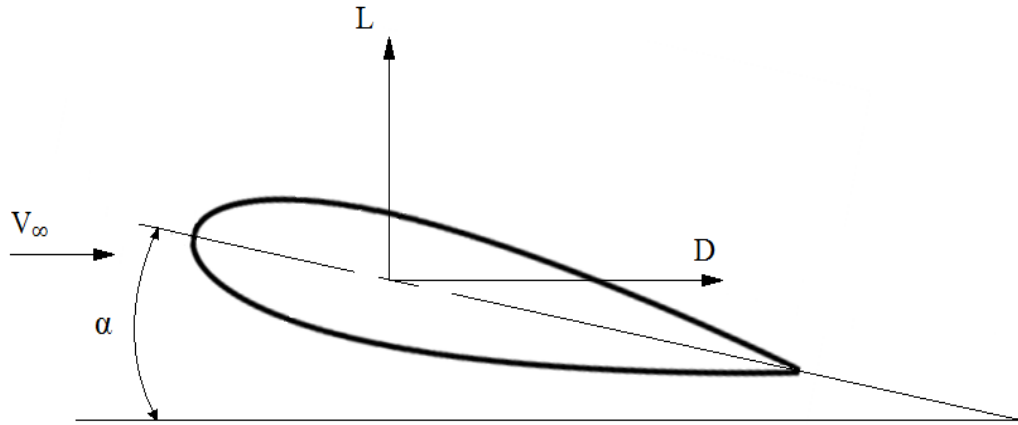
Figure 5.4: Aerofoil showing force components.

5.2.1 Lift Coefficient Analysis

The LS, MS, and TS aerofoils consisting of span–length slots at X=15%, X=45% and X=70% respectively were compared with the plain aerofoil configuration, i.e. the NACA0018 aerofoil with the absence of boundary layer control slots (baseline aerofoil). Fig 5.5 to 5.8 illustrates this comparison at the designated Reynolds numbers. The figures show that at low angles of attack (0° to 8°), the lift coefficient of the aerofoils increased linearly with AoA, indicating favourable pressure gradient. However the stall angle and maximum lift coefficient (C_{Lmax}) differed; the stall angle (S_α) of the Plain and TS aerofoil (X=70%) was at 12° AoA, but the presence of the slots at X=15% and X=45% in the LS and MS aerofoils increased the stall angle beyond that of the baseline aerofoil to 15° and 14° AoA respectively. This may have occured as a result of flow attachment on the upper surface of these aerofoils (LS and MS) at and within the vicinity of 15° and 14° AoAs, caused by the stimulation (turbulent mixing) of the boundary layer by to high momentum flow jet emanating from the slots. A summary of the maximum lift coefficients and stall angles of the plain and slotted aerofoils at the designated Reynolds numbers is given in Table 5.2. The lift curve of the Plain aerofoil is characterized by a steep decrease in lift gradient between 12° to 20° AoA (post stall region) due to large increase in boundary layer separation. On

the other hand, the slotted aerofoils exhibited a lesser decrease in lift gradient, a desirable quality for a wind turbine blade. Once more, the lesser steep lift gradient in the post stall AoAs could be attributed to boundary layer stimulation by slot flow jet. It was obvious that the lift coefficients of the Plain aerofoil were higher than those of the slotted aerofoils in the AoA range between 0° to 16°. Ensuing the baseline aerofoil was the TS and MS aerofoils, while the LS aerofoil exhibited the least C_L values in the entire range of AoA. To further illustrate this disparity; at 5° AoA the values of C_L for the LS, MS, and TS aerofoils were 324%, 95% and 87% respectively lower than that of the plain aerofoil, but at 12° AoA the difference between the C_L values of these slotted aerofoils (LS, MS, and TS) and the plain aerofoil were reduces to 134%, 41%, and 31% respectively. However at the post stall AoAs where the slotted aerofoils exhibited a slower rate of decrease in lift gradient; the difference between C_L values of the TS, MS and Plain reduced enormously at 18° and 20° AoAs, the C_L value of TS was 4% lower than the plain aerofoil, while MS was 3% higher than the plain aerofoil. Finally, it was noted that the change in Reynolds number had only a minor effect on the lift coefficient values, since a difference of about ± 0.02 was observed in the entire range of angle of attacks. Fig 5.9 shows the variation of maximum lift coefficient as a function of Reynolds number for Plain and slotted aerofoils at their representative stall AoAs. This figure shows that the maximum lift coefficient of the plain, MS and TS aerofoils increases linearly with increase in Reynolds number, but for the LS the reverse is the case, its maximum lift coefficient reduced linearly from $92x10^3$ to $230x10^3$. Lift coefficients computed from the wind tunnel test of LS, MS, and TS aerofoils consisting of span–length slots at X=15%, X=45% and X=70% respectively have each been compared with the plain NACA0018 aerofoil. The results clearly show that the slot presence at each specified location was ineffective in improving the C_L over the entire range of AoA. For the purpose of clarification, a further investigation into this outcome will be carried out in the numerical investigation later in this chapter
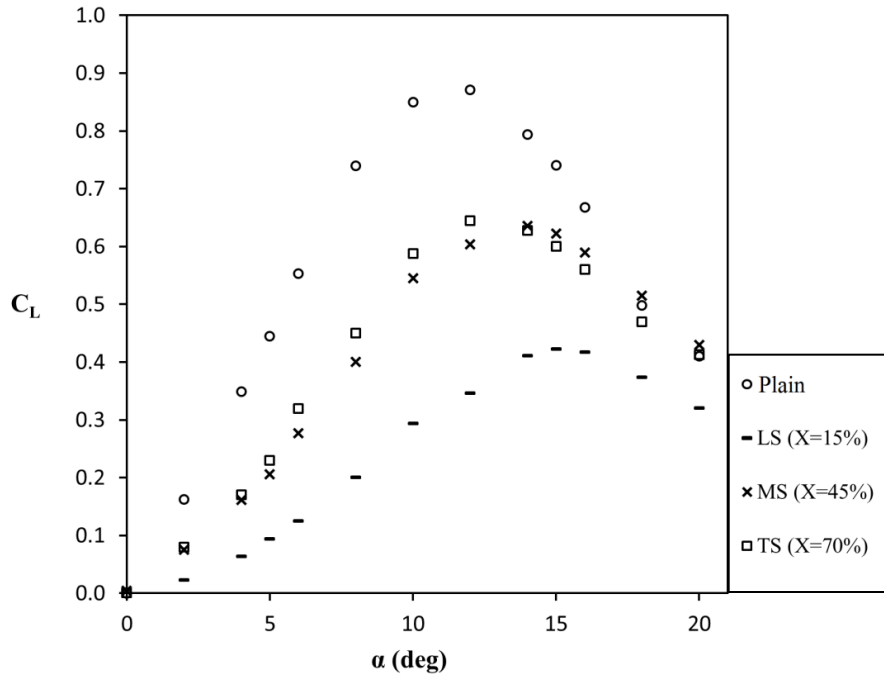
Figure 5.5:Comparison of experimental Lift coefficient measurements vs AoA for Plain and Slotted aerofoils at Re=92x10³.
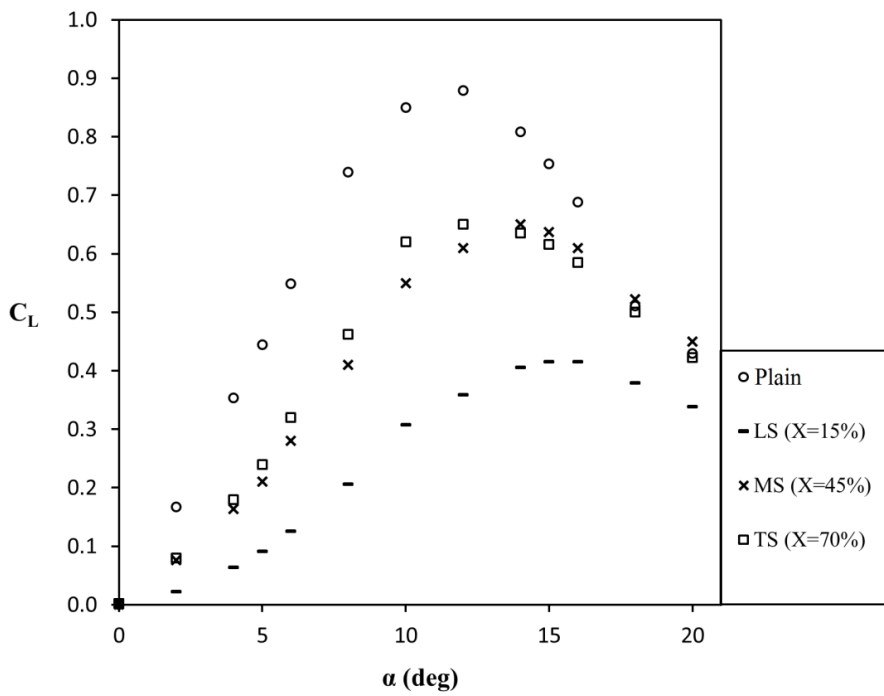
Figure 5.6: Comparison of experimental Lift coefficient measurements vs AoA for Plain and Slotted aerofoils at Re=138x10³.
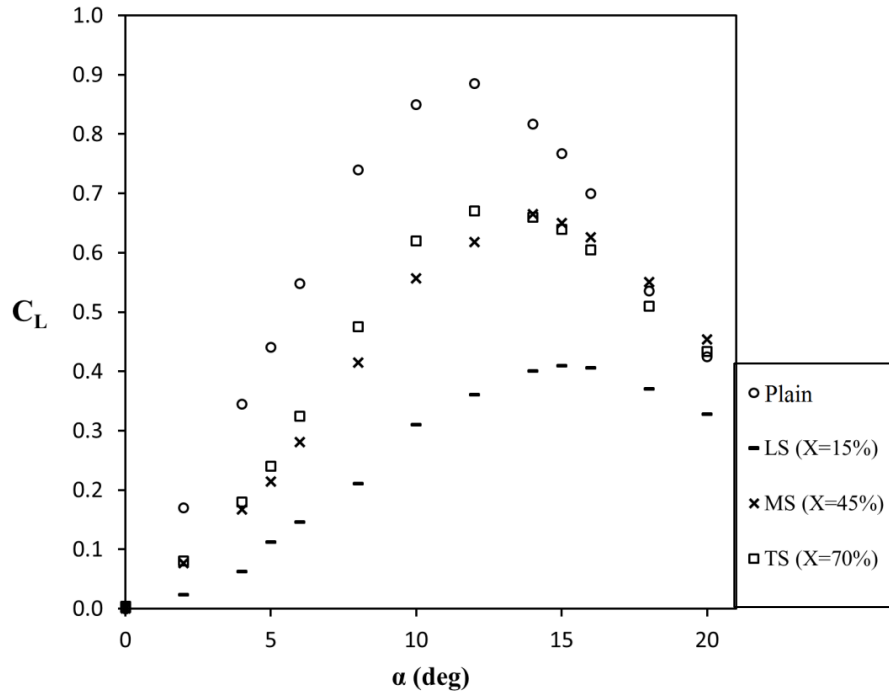
Figure 5.7: Comparison of experimental Lift coefficient measurements vs AoA for Plain and Slotted aerofoils at Re=184x10³.
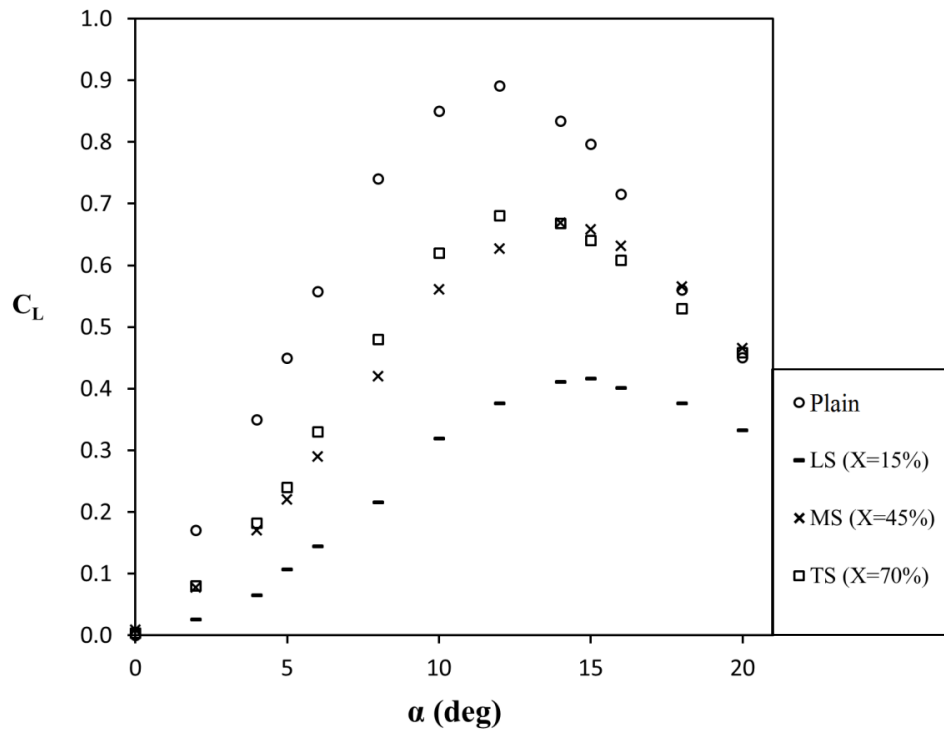
Figure 5.8: Comparison of experimental Lift coefficient measurements vs AoA for Plain and Slotted aerofoils at Re=230x10³.
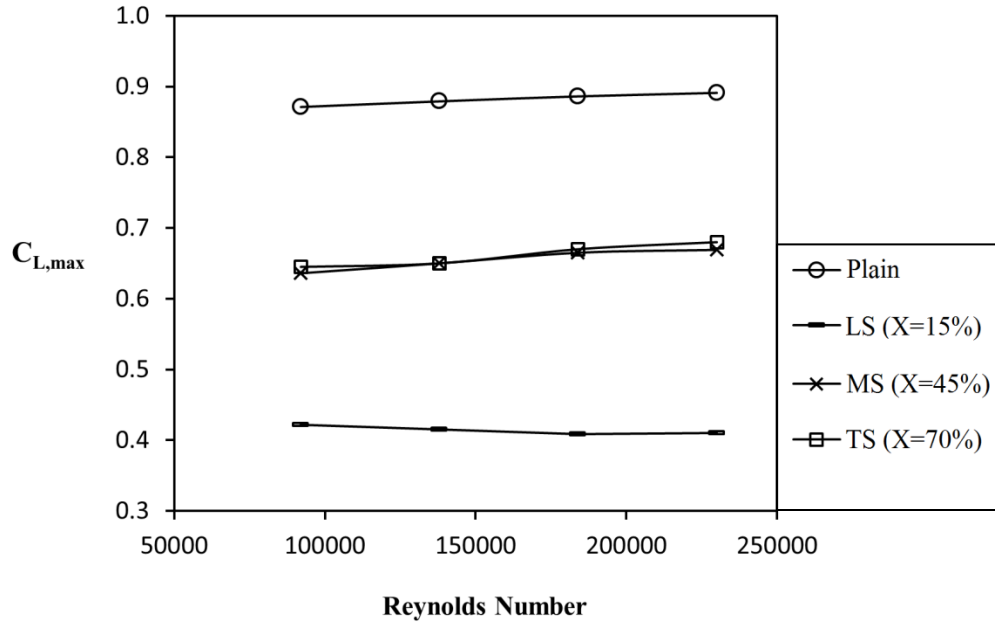
Figure 5.9: Variation of maximum lift coefficient with Reynolds Number for Plain and Slotted aerofoils.

Table 5.2: Stall angle and Maximum lift coefficient of Plane, LS, MS and TS aerofoils.

Re (10^3)	Plane		LS		MS		TS	
	C_{Lmax}	S_α	C_{Lmax}	S_α	C_{Lmax}	S_α	C_{Lmax}	S_α
92	0.87	12	0.42	15	0.64	14	0.64	12
138	0.88	12	0.41	15	0.65	14	0.65	12
184	0.89	12	0.41	15	0.67	14	0.67	12
230	0.89	12	0.41	15	0.67	14	0.68	12

5.2.2   Drag Coefficient Analysis

Fig 5.10 to 5.13 compares the drag coefficient curves of the slotted aerofoils; LS (X=15%), MS (X=45%) and TS (X=70%) with the plain aerofoil for Re=92x10^3 to Re=230x10^3. It was evident from the figures that within the chosen range of incidence (α =0° to α =20°) the slots altered the drag characteristics. For each aerofoil, the change in Reynolds number resulted in an average of $\pm$4% change in drag coefficient values (at each data point) between successive Reynolds

numbers over the entire range of angle of attack. Nevertheless, the trend of the C_D curves was consistent for all Reynolds number. The plain aerofoil exhibited a gradual increase in drag coefficient gradient at low angle of attack (between $\alpha = 0°$ to $\alpha \approx 10°$). This is due to the fact that within this range of AoA, the flow is dominated by viscous forces. A similar trend was observed in the drag coefficient curves of all the slotted aerofoils. Beyond this range of incidence the drag gradient increases rapidly due to stall phenomena associated with boundary layer flow separation. Within the range of AoA ($\alpha = 0°$ to $\alpha \approx 15°$) the slotted aerofoils clearly exhibited higher drag coefficients than the plain aerofoil. At $\alpha = 5°$ for example, the LS, MS and TS aerofoils were 140%, 70% and 20% higher than the plain aerofoil respectively. Likewise at $\alpha = 12°$, the LS, MS and TS aerofoils were 60%, 27% and 12% higher than the plain aerofoil. Thus for the designated Reynolds numbers the LS aerofoil (X=15%) exhibited the largest drag coefficients in the range $\alpha = 0°$ to $\alpha = 15°$. It is obvious from the C_D curves that there is a correlation between the large drag coefficients and the low lift coefficients of the slotted aerofoils between the incidence range of $\alpha = 0°$ to $\alpha \approx 15°$. The large drag in this range of incidence ($\alpha = 0°$ to $\alpha \approx 15°$) may be attributed to additional drag induced by slot flow. However, further clarification regarding this problem will be discussed in the numerical investigation later in this chapter.

In the region of 18° to 20° AoA, the drag coefficient values of MS (X=45%) was 6% lower than the plain aerofoil while TS was 7% lower than the plain aerofoil at 20° AoA, making X=45% and X=70% the only slot positions that were effective in reducing drag below that of the plain NACA0018. The drag coefficient of LS (X=15%) was larger than the MS, TS and the Plain aerofoil over the entire range of incidence. Despite the fact that MS had the lowest C_D between 18° to 20° AoA, in the entire range of AoA, TS(X=70%) aerofoil exhibited an average C_D that was lower compared to the other slotted aerofoils.

Figure 5.10: Comparing the Lift to Drag Ratio vs AoA for Plain and Slotted aerofoils at Re=92x10³.
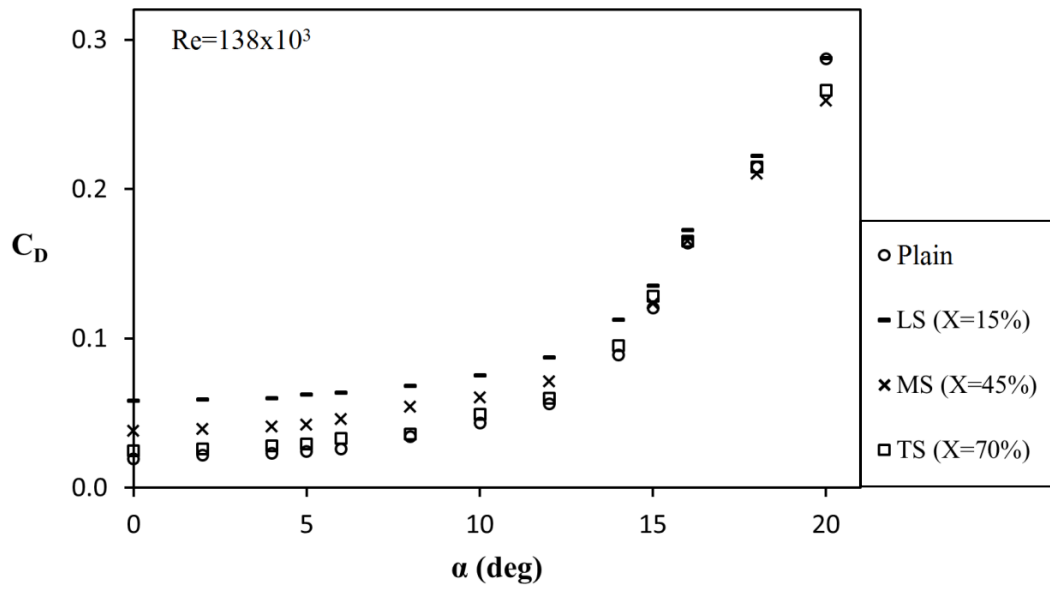
Figure 5.11: Comparing the Lift to Drag Ratio vs AoA for Plain and Slotted aerofoils at Re=138x10³.
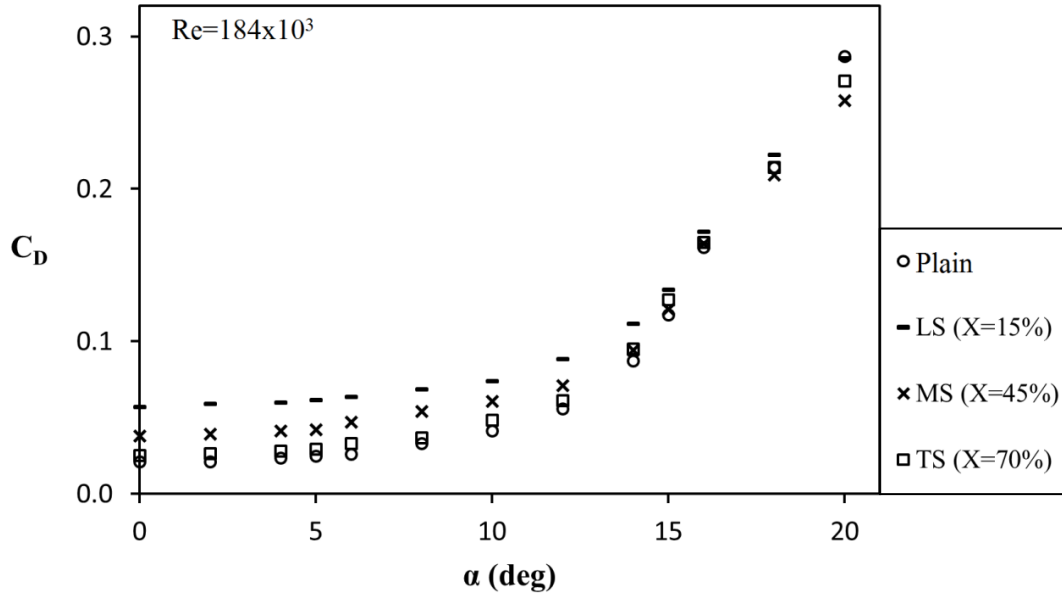
Figure 5.12: Comparing the Lift to Drag Ratio vs AoA for Plain and Slotted aerofoils at Re=184x10³.
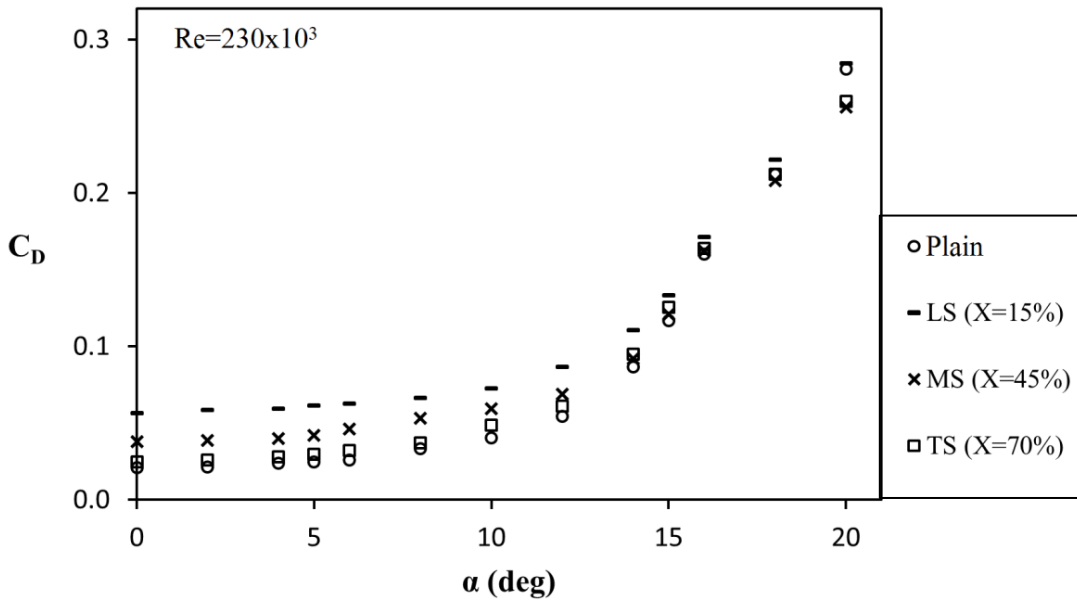
Figure 5.13: Comparing the lift–to–drag ratio vs AoA for plain and slotted aerofoils at Re=230x10³.

5.2.3   Lift to Drag Ratio

Typically a higher lift–to–drag ratio (L/D) is one of the main objectives when designing a wind turbine rotor; hence, in some way L/D serves as an efficiency factor that influences the preference

of a particular aerofoil over another [152]. Fig. 5.14 to Fig. 5.17 below compares the L/D versus

AoA of the plain and slotted aerofoils at the designated Reynolds numbers. The features of the

L/D curves are a direct result of lift and drag characteristics of the respective aerofoils already

discussed in section 5.2.1 and 5.2.2. From the figures the values of the L/D ratio of the slotted

aerofoils were significantly lower than those of the plain aerofoils between $\alpha = 0°$ to $\alpha = 15°$.

This implies that the plane aerofoil had the highest maximum L/D ratio (≈ 22 at $\alpha = 8°$). Thus

the TS aerofoil which was the slotted aerofoil with the highest maximum L/D (≈ 12.9 at $\alpha = 8°$)

was about 40% lesser than that of the plain NACA0018 aerofoil. However between $\alpha = 16°$ to α

$= 20°$, the difference between the plain and slotted aerofoils diminishes; at $\alpha = 18°$ and $\alpha = 20°$

the L/D ratio of the MS aerofoil (X=45%) surpassed that of the plain aerofoil, it was 4% higher at

$\alpha = 18°$ and 15% higher $\alpha = 20°$. Nonetheless, the LS had the least L/D performance over the
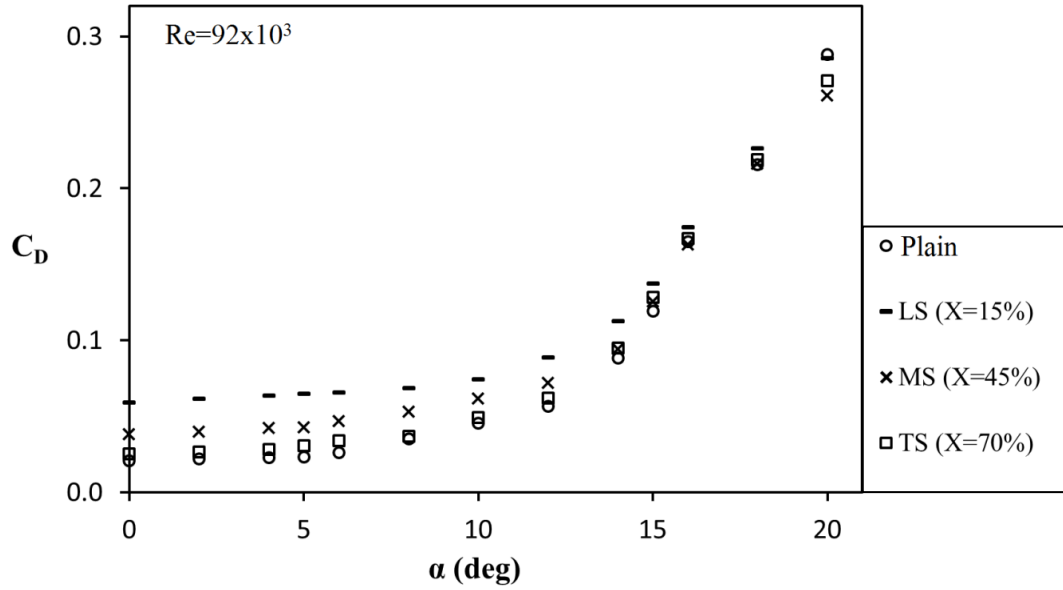
entire range of incidence.
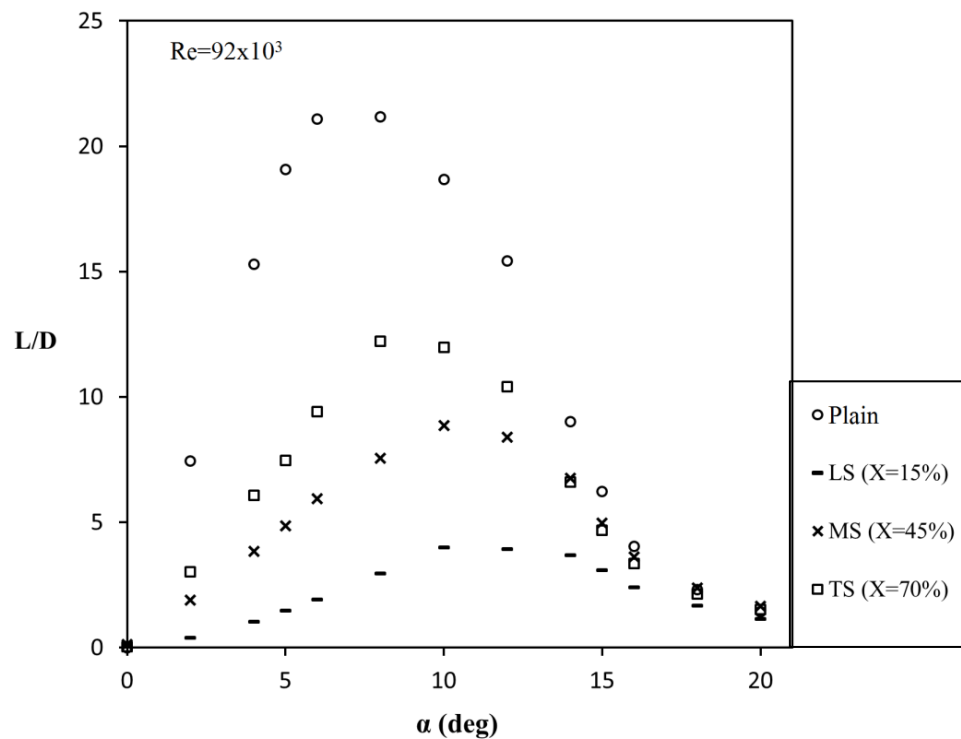
Figure 5.14: Comparison of lift to drag ratio vs AoA for Plain and Slotted aerofoils at Re=92x10³.
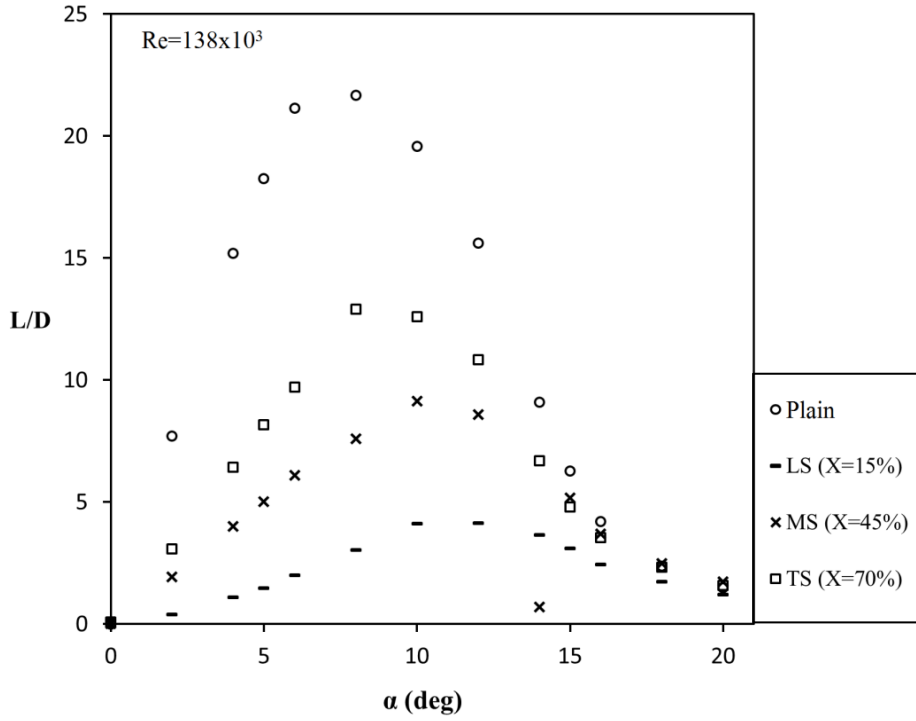
Figure 5.15: Comparison of lift to drag ratio vs AoA for Plain and Slotted aerofoils at Re=138x10³.
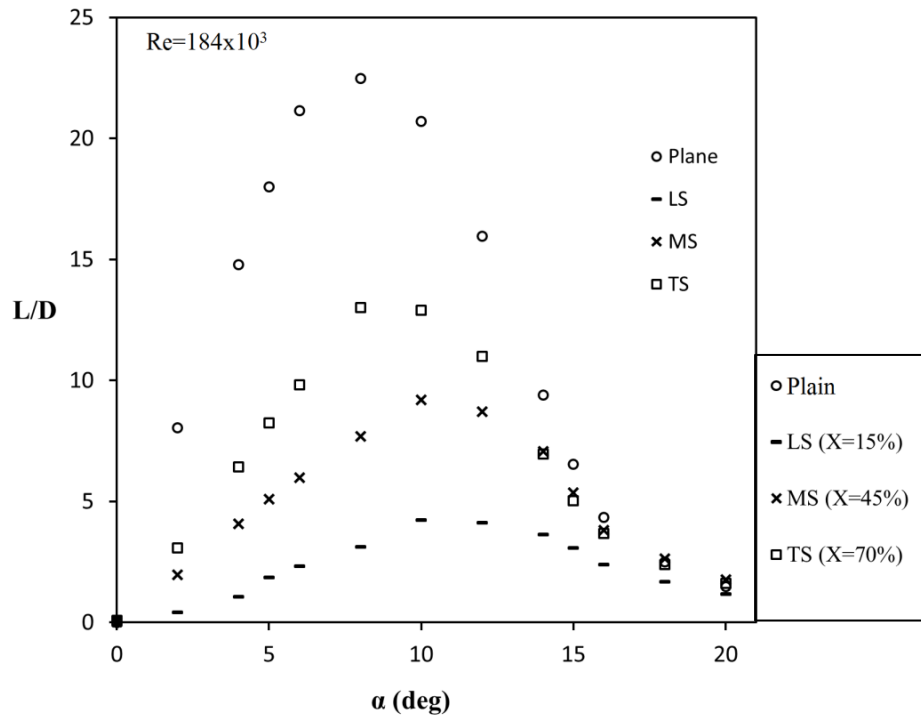
Figure 5.16: Comparison of lift to drag ratio vs AoA for Plain and Slotted aerofoils at Re=184x10³.
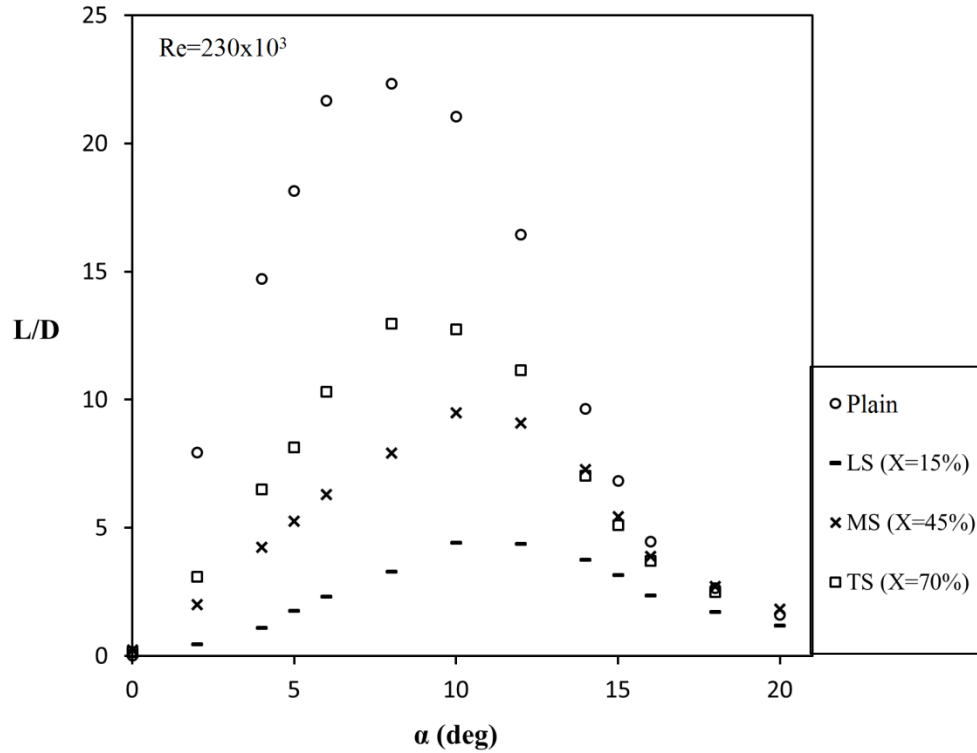
Figure 5.17: Figure 5.16: of lift to drag ratio vs AoA for Plain and Slotted aerofoils at Re=230x10³.

In conclusion, the effect of slot position has been investigated from the wind tunnel test results. From the analysis of the force coefficients and L/D ratios of the plain and slotted aerofoils, it is correct to state that the span–length slots at X=15%, X=45% and at X=70% were ineffective in improving the aerodynamic performance of the NACA0018 aerofoil especially within the range of $\alpha = 0°$ to $\alpha = 15°$. The L/D of the slotted aerofoils decreased substantially in this range of incidence compared to the plain aerofoil. The overall effect of slot induced drag was identified as one of the main reasons for the drop in performance. However, about 4% and 15% increase in L/D ratio was detected in the MS aerofoil at $\alpha = 18°$ and $\alpha = 20°$ (with respect to the plain aerofoil). Finally, it was observed that closer the slot position is to the leading edge on the NACA0018 aerofoil the worse the overall performance of the aerofoil becomes. Therefore further changes to the geometry of the slots are needed in order to increase the aerodynamic efficiency of the slotted aerofoils.

5.3 Smoke Visualization Results and Discussion

The results of the smoke visualization experiments introduced earlier in section 3.5 are discussed here. The aim of this smoke visualization experiment was to study the flow stream around the plain and slotted aerofoils by investigating the effect of the slots positions on flow stream in relation to angle of attack, substantiate the measured lift and drag characteristics, especially at post stall AoA, and monitor the extent of the separation regions and vortexes on the upper surface of the aerofoil in both low and high angles of attack. The main advantage of this procedure is that, it explains the flow characteristics over these aerofoils without incorporating complicated data reduction and analysis [153]. In Fig. 5.18 to Fig. 5.21 the flow stream over the plain and slotted NACA0018 aerofoils at a Reynolds number of 138×10^3 and angles of attack 4°, 8° and 16° are compared. As already explained in section 3.5, the smoke visualization test was limited to a Reynolds number of 138×10^3 in order to prevent difficulty in observing and capturing the flow field. During the smoke visualization process, the smoke stream approaching the aerofoil stagnation point is deflected over the top surface of the aerofoil. But at the established Reynolds number, it was difficult to capture distinct smoke lines or filaments over the aerofoil. Instead, the smoke filaments break down and disperse across the test section. Dark sections over the upper surface of the aerofoils signify regions of flow separation. The characteristics of the separated region which forms on the aerofoils is influenced by Reynolds number, angle of attack, and as well as the slot positions [154][155]. The key observations from the experiment are as follows;

At $\alpha = 4°$ there seem to be no visible indication of flow separation for both the plain and slotted aerofoils. The pressure gradient at this AoA is still favourable, thus the smoke streamlines conform to the shape of the aerofoil.

At $\alpha = 8°$ a small separation zone was noticed by the displacement of the smoke stream from the upper surface of the plain aerofoil (see Fig. 5.18(b)). The boundary layer separates at $0.8c$ (x/c=80%) and never reattaches. Usually separation starts from the trailing edge and advances

progressively towards the leading edge as AoA increases. In other words, throughout the range of moderate to high AoA, a forward progression of separation in a continuous and gradual manner is expected [155]. Considering the slotted aerofoils, the pressure difference between the slots outlets was significant enough to initiate a change in the boundary layer. Thus, smoke jet escaped from the slot on the top side of the aerofoil with enough momentum to overcome the adverse pressure gradient and fill up the separated zone downstream (see Fig. 5.19(b) Fig. 5.20(b) Fig. 5.21(b)) hence, separation was unnoticed on at 8°.

At $\alpha = 16°$ the difference between the smoke stream over the top surfaces of the plain and slotted aerofoils was very obvious. At this AoA the flow is overwhelmed by a large pressure gradient which resulted in a dramatic rise in drag. For the plain aerofoil there was a large region of flow separation covering almost the entire upper surface, the separation started from $0.21c$ (x/c=21% from the aerofoil leading edge) downstream without reattachment (see Fig. 5.18(b)). For the slotted aerofoils LS MS and TS, a leading edge separation point was detected. The slot outlets were located in the inner region of the actual separation zone thus, smoke jets emanating from the slots filled the separation zone forming a pseudo–reattachment zone within the separation zone. The pseudo–reattachment zone emerged as a result of turbulent mixing of smoke molecules in the separation zone. The turbulent mixing enables stimulation of the boundary layer on the suction side of the slotted aerofoils thus, it can be inferred that turbulent mixing was responsible for the less steep lift gradient in the post stall AoAs of the slotted aerofoils. Table 5.3 below summarizes the position of separation points on both the plain and slotted aerofoils at $\alpha = 8°$ and $\alpha = 16°$.

Table 5.3: Separation Point at 8° and 16° angle of attack.

Aerofoil	8° AoA	16° AoA
Plain	80%	21%
LS	—	12%
TS	—	12%
MS	—	13%
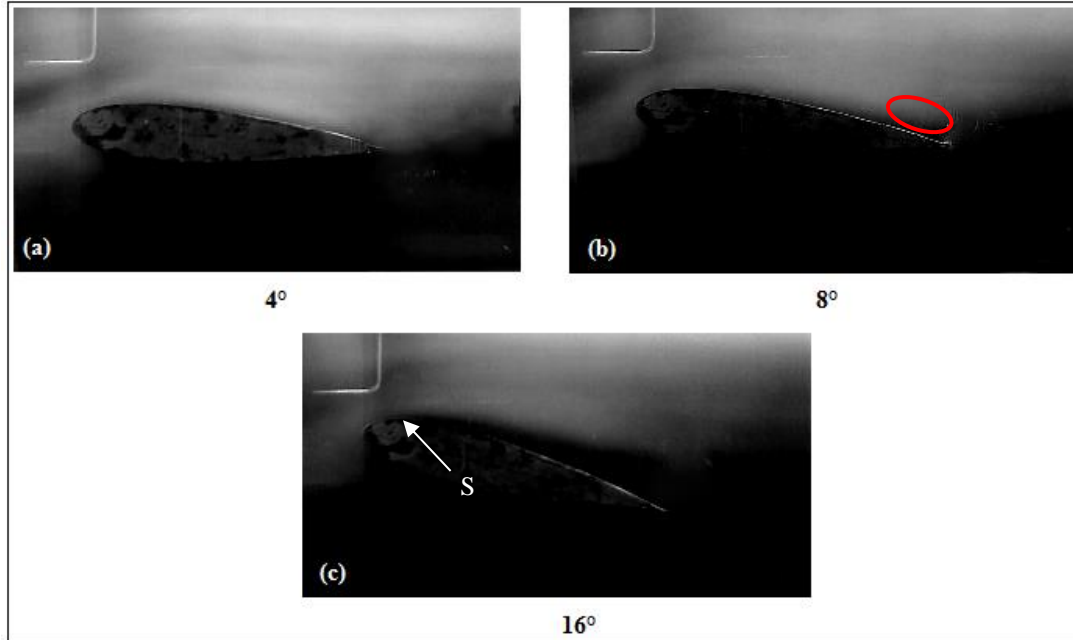
Figure 5.18: Smoke visualization of plain aerofoil at Re= Re=138x10³ (a) 4° AoA (b) 8° AoA (c) 16° AoA.
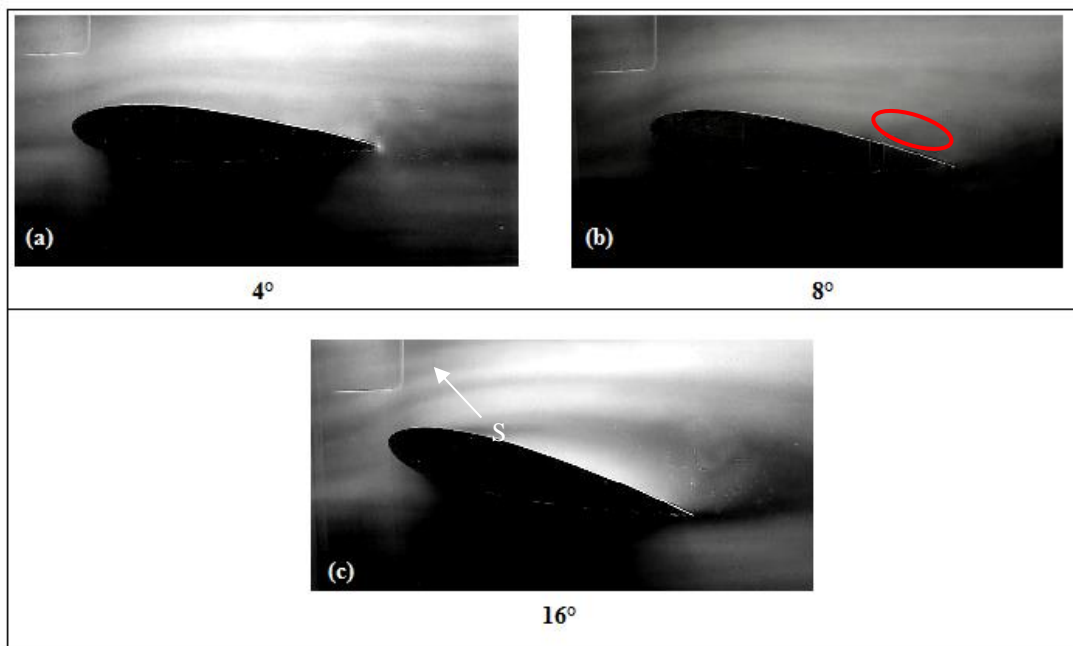
Figure 5.19: Smoke visualization of LS aerofoil at Re=138x103 (a) 4° AoA (b) 16° AoA.
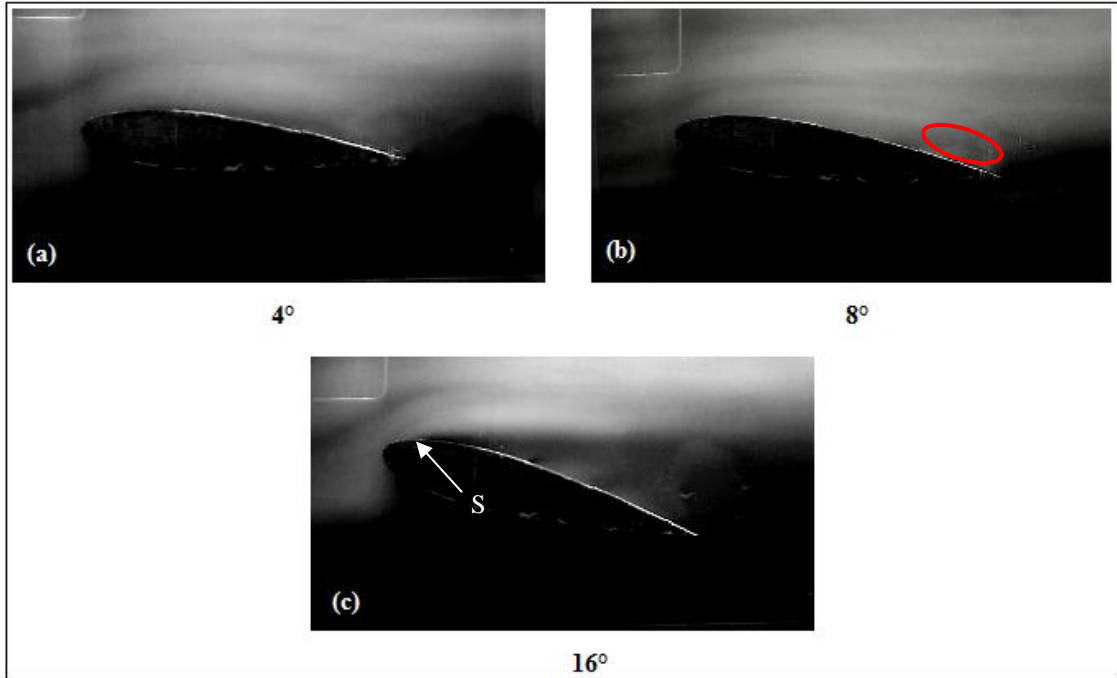
Figure 5.20: Smoke visualization of MS aerofoil at Re= Re=138x10³ (a) 4° AoA (b) 8° AoA (c) 16° AoA.
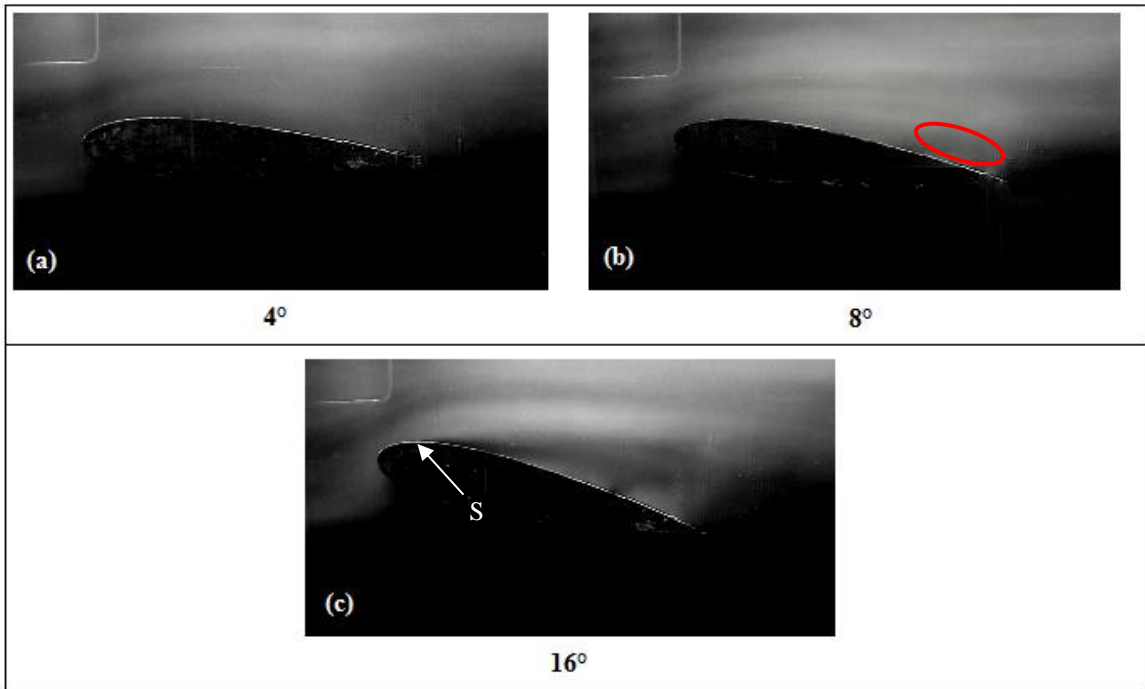
Figure 5.21: Smoke visualization of TS aerofoil at Re=138x103 (a) 4° AoA (b) 16° AoA.

5.4 Numerical Investigation

So far, the experimental investigation of the effect of slot location (at X= 15%, X= 45% and X= 70%) on the NACA0018 has indicated that at low and moderate AoAs the slots caused an enormous deficit in aerodynamic performance. Therefore, further sensitivity study on the effect of slot geometric alterations on aerodynamic performance was carried out. These alterations were; slot combination, slot size, and slot slope. The changes were made to the NACA0018 aerofoil without changing the overall slot configuration. Numerical simulation was adopted for this sensitivity study for the purpose of saving aerofoil fabrication cost, and time required for wind tunnel test, data reduction and analysis. It was expected that by performing the sensitivity study numerically, a deeper understanding of the flow physics inside the slots can be achieved. Furthermore, critical fluid phenomena and pattern changes around the aerofoil could be revealed. About 200 simulations were performed, and it is expected that the outcomes from these tests would form a useful information base for future designs of aerofoil control mechanisms.

5.4.1 Validation of Numerical Results

The numerical results were compared with their corresponding experimental measurements for the purpose of validating the turbulence model. Fig.5.22 and Fig.5.23 compares the lift and drag coefficients of the plain and TS aerofoils obtained by numerical simulation and experimental measurements at Reynolds number of 230×10^3. For the lift coefficient (Fig. 5.22), there was good agreement between the numerical results and experiment. The maximum lift coefficient C_{Lmax} and stall angle S_α were well predicted for the plain and TS aerofoils. This implies that the turbulent shear and flow separation are modelled by the SST k–ω turbulence model to an acceptable accuracy in each case [156]. The trend of the drag coefficient curves was consistent, but the numerical C_D was lower than the experimental C_D by an average of 15% for both plain and TS aerofoils. This difference was mainly as a result of the high wake blockage in the wind tunnel test due to the close proximity between the aerofoil and the test section walls (c/h=0.694).
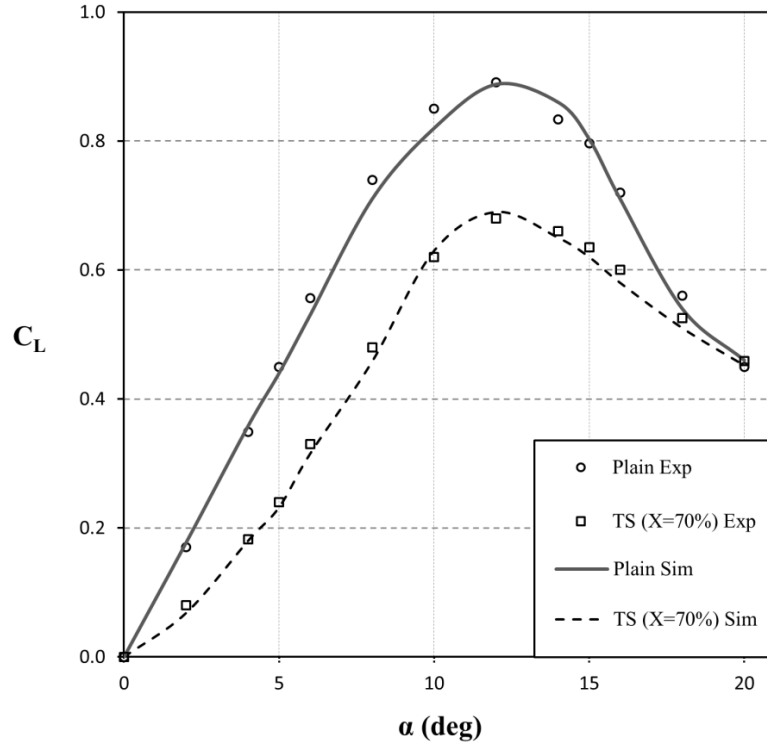
Figure 5.22: Experimental and Numerical comparison of lift coefficient for plain and TS aerofoils.
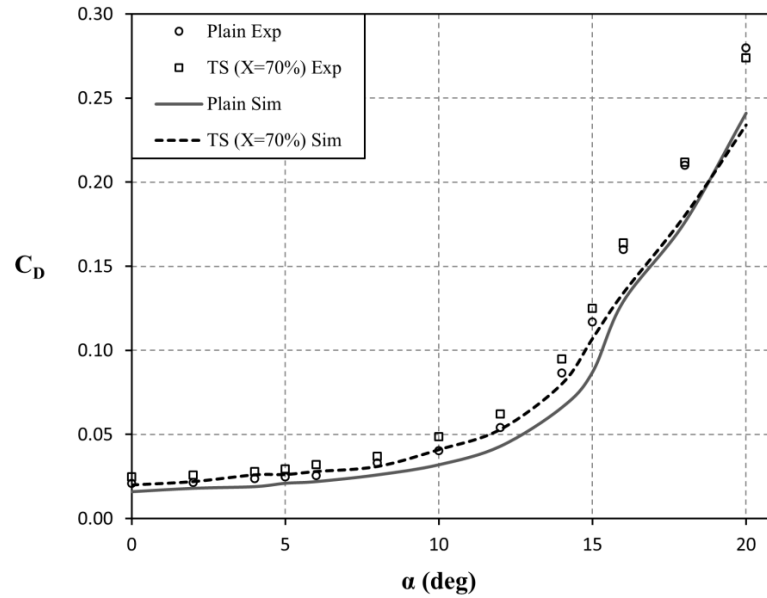
Figure 5.23: Experimental and Numerical comparison of drag coefficient for plain and TS aerofoils.

Theoretically for steady 2D flows, the separation point is defined as the point where the wall shear stress τ_w equals zero [157]. Thus a plot of x–component of wall shear stress along the wall

of an aerofoil relative to the chord (x/c) is used to determine the exact flow separation point in both slotted and unslotted cases [158]. Also by plotting pressure coefficient versus positions on the wall relative to chord length (x/c), flow separation zone on the suction side of the aerofoil is identified by a flat out region (also refered to as plateau) of the curve indicating constant pressure. To futher illustrate this, flow separation on the suction side of an aerofoil begins when the pressure gradient increases in the direction of the flow. During this process the outer streamline adjusts in such a way that pressure within the boundary layer remains approximately constant. In the region close to the wall the velocity gradient reduces, and at the separation point the wall shear stress is brought to zero. From this point downstream the wall shear stress τ_w becomes negative, C_p relatively constant, the flow reverses, and a region of recirculating flow develops. However, in some cases, the flow may reattach forming a separation bubble as a result of model geometry or a variety of other factors.

Fig.5.24 shows a graph of the shear stress versus x/c along the wall of plain, MS and TS aerofoils at 8° and 16° AoAs for Re=138x10^3. The τ_w versus x/c graph was chosen over the C_p versus x/c graph because for the former it is easy to identify the separation point, but for the latter the separation zone could be well represented but the separation point is usually not so clear. From the figure it can be deduced that at 8° AoA, the separation point was at x/c=82% for the plain aerofoil, x/c=40% for MS and x/c =64% for TS. At 16° AoA it was observed that the separation point had moved to x/c=24% from the leading edge on the plain aerofoil, and on the slotted aerofoils MS and TS the separation point moved upstream to x/c=15% and x/c=14% respectively. However for MS and TS a small region of flow attachment (+ve τ_w) was noticed in the vicinity of the slot on the top walls. Therefore it was confirmed that the separation point shifts upstream as AoA increases, and the shift in separation point is consistent with that observed in the smoke visualisation on the Plain, MS and TS aerofoils in Table 5.3.
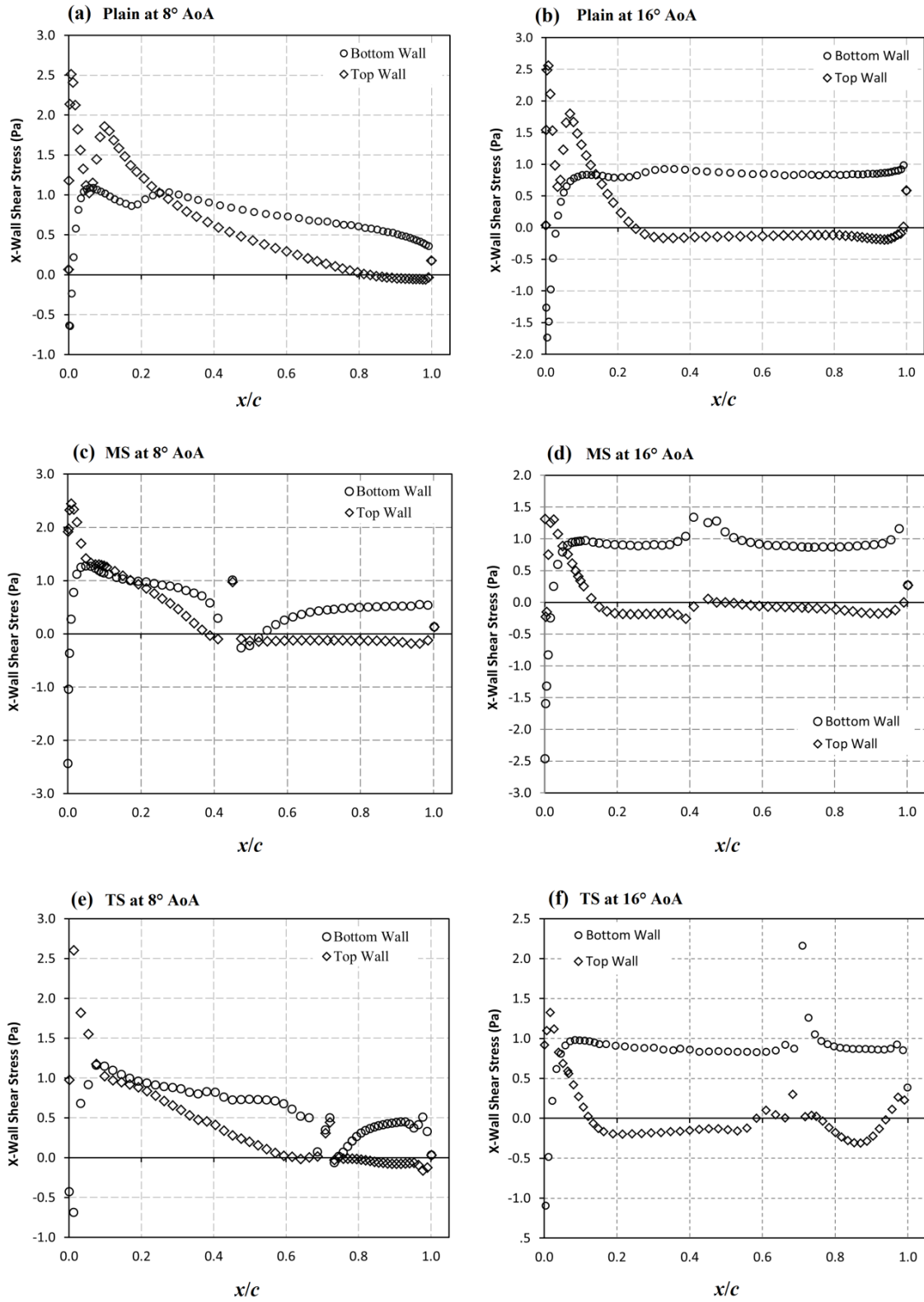
Figure 5.24: x-component of wall shear stress along the wall versus relative chord for AoA = 8° and 16° Re=138x10³.

In order to investigate the cause of the poor performace of the slotted aerofoils at low angles of attack, the velocity contour around the aerofoil was produced from Fluent, and analysed. Fig 5.25 below shows the velocity contours of the plain, LS, MS and TS aerofoils showing the velocity variations around these aerofoils at 8° AoA for Re=138x10^3. The colourmap represents the range of velocity magnitude; where the colours red and blue at both extremes of the coulourmap indicate maximum and minimum velocity respectively.
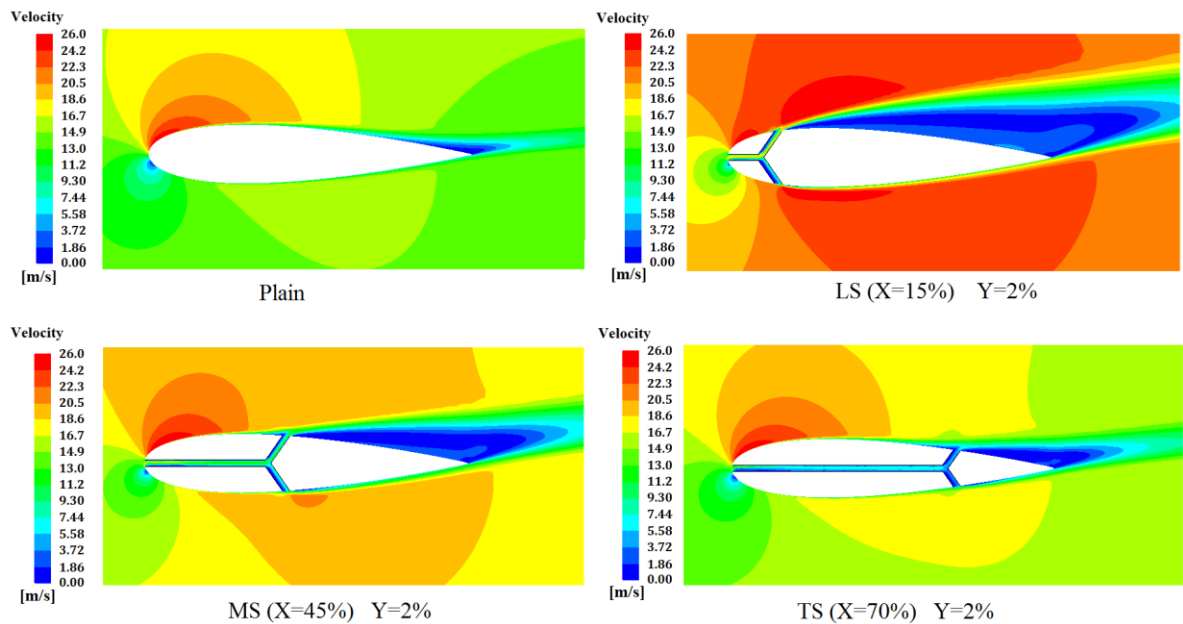
Figure 5.25: Velocity contours for Plain, LS, MS and TS aerofoils at Re= Re=138x10^3; AoA Y=2%; 8° AoA.

Considering the plain aerofoil for example; the separation point is at *x/c*=80% of the chord (Fig. 5.25), from this point downstream the flow was completely separated from the suction side, and the separated zone is denoted by a small wake region with low velocity (blue colour). For the slotted aerofoils, pressure difference between the outlets of the chord slot, bottom wall slot and the top wall slot actuates a jet on the suction side, which disturbs the velocity profile around the aerofoil. At 8° AoA, the position of the slots on LS (X=15%), MS (X=45%) and TS (X=70%) were upstream from the separation point (*x/c*=80%) on the plain aerofoil. In other words, the slots were located outside the separation zone (which was from *x/c*=80% downstream) of the plain

NACA0018 aerofoil. Hence the momentum generated by the jet emanating from the slots at this incidence angle led to an early transtion from laminar to turbulent flow which produced a large wake downstream of the slot. Therefore, this resulted in a large increase in drag and poor aerodynamic performance. As angle of attack increases, it was noticed that less fluid flows (lower velocity) into the chordal slot, and out of the side slots into the boundary layer due to the vertical movement of the leading edge away from the direction of the flow stream. As shown in Fig 5.26, at $\alpha = 16°$, the slots on MS and TS were within the separation zone of the plain aerofoil, therefore the jet emanating from their slots had a positive impact on the boundary layer—thereby improving their aerodynamic. However for LS, its slot was still outside (upstream) the separation zone and the result of this is evident in its poor performace over the entire range of AoA. In the following sections of this report, the objective was to optimize the slotted NACA0018 aerofoil by investigating the effect of more slot parameters on aerodynamic efficiency. Numerical results are presented and analysed for Re=230x10^3.
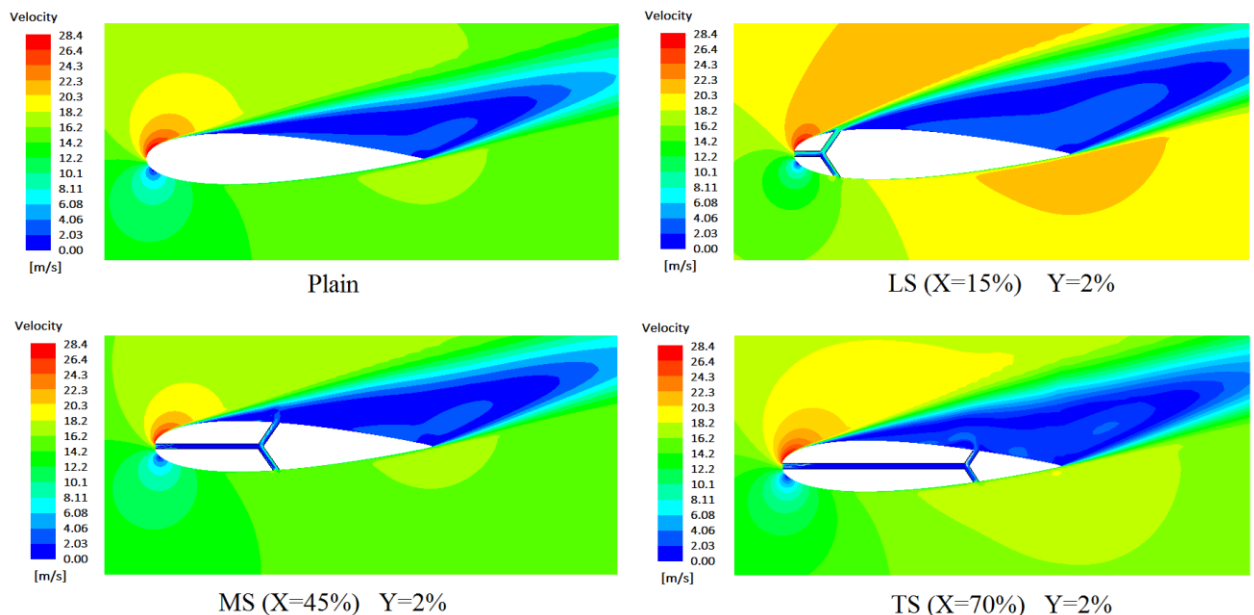
Figure 5.26: Velocity contours for Plain, LS, MS and TS aerofoils at Re= Re=138x10^3; AoA Y=2%; 16° AoA

5.4.2 Effect of Multiple Span-length Slots

This section deals with a scenario when more than one exit slots were produced on both sides of the NACA0018 aerofoil. A 2D section of the slotted aerofoil with multiple slot positions i.e. LMS (X=15% and X=45%), LTS (X=15% and X=70%), MTS (X=45% and X=70%) and LMTS (X=15% X=45% and X=70%) is shown in Fig. 5.27. The performance of these slotted aerofoils was examined based on their lift–to–drag ratios. The study was done over the whole range of AoA from 0° to 20° at Re= 230×10^3 and the results (in L/D ratio) were compared with that of the Plain, MS and TS aerofoils (see Fig. 5.28). L/D ratio was preferred because it gives a comprehensive representation of aerodynamic performance of an aerofoil.

Lead and Mid Slot (LMS) **Lead and Trail Slot (LTS)**

Mid and Trail Slot (MTS) **Lead, Mid and Trail Slot (LMTS)**
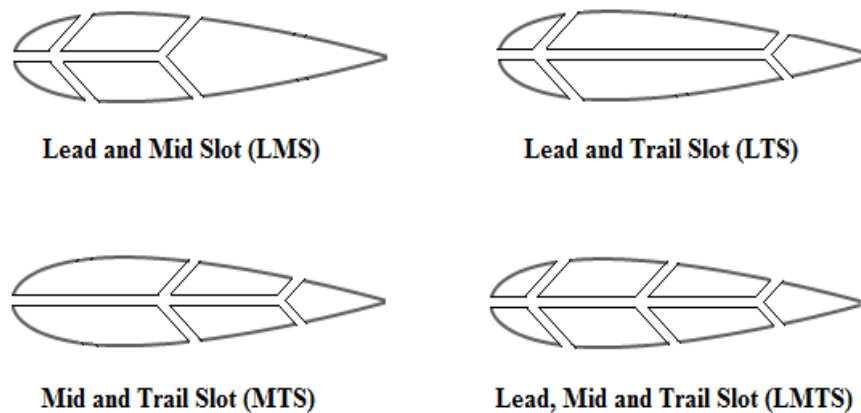
Figure 5.27: Combination of slot positions.

The MTS exhibited the highest L/D ratio among the aerofoils with multiply slot positions. Its maximum L/D value was 8.8 (at 10°) which was 2.5% higher than that of MS (also at 10°). From Fig. 5.28 it can be seen that the L/D values of MTS were slightly higher (about 5.4%) than MS between $\alpha = 0°$ to $\alpha = 12°$. This was as a result of the positive effect of the side slot X=70% at low AoAs. On the other hand, between $\alpha = 12°$ to $\alpha = 20°$ the L/D values of MTS were 2% lower than those of MS. A possible explanation for the decrease in L/D between $\alpha = 12°$ to $\alpha = 20°$ is that, the additional slots might have initiated an increase in turbulent wake and reverse flow downstream of the slots, thus causing an increase in drag. TS was the best slotted aerofoil; the

multiple slotted aerofoils with slot at X=15% (LMS, LTS and LMTS) displayed the least L/D ratio, which further confirms the fact that a slot at X=15% is detrimental to the aerofoil performance. Therefore span–length slots at multiple positions on the NACA0018 aerofoil were ineffective in improving the overall L/D performance beyond that of TS and plain aerofoil.
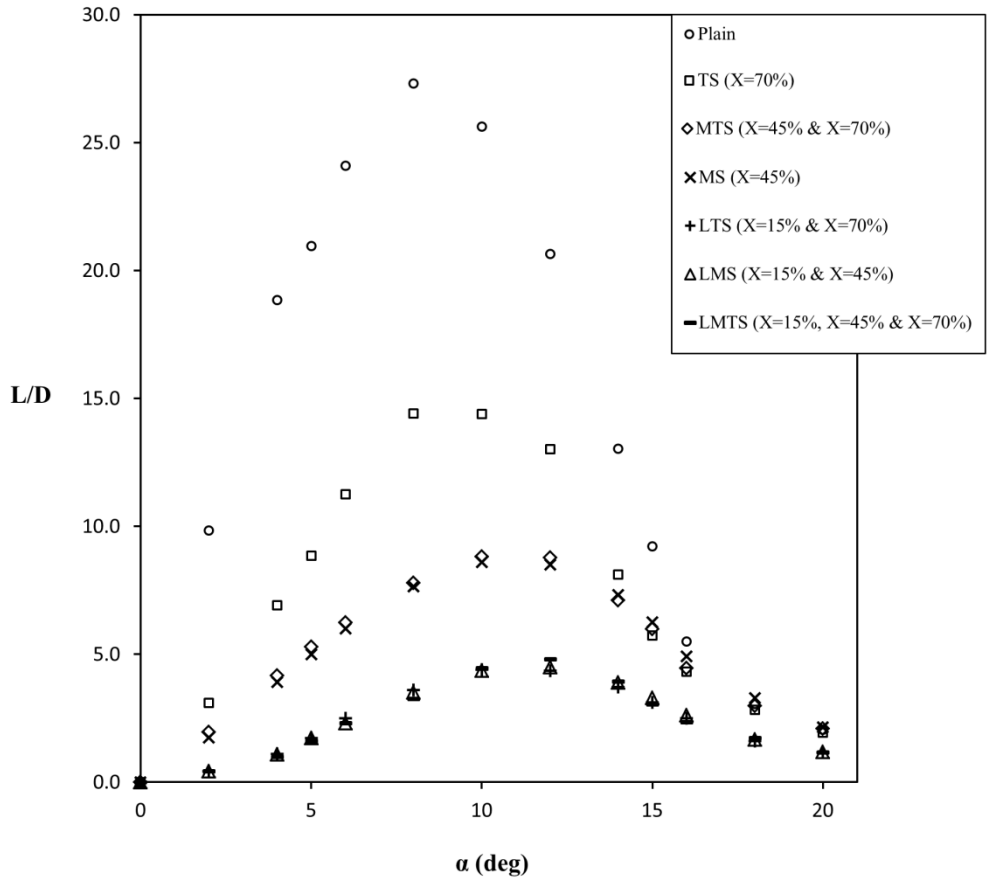
Figure 5.28: Multiple slot positions.

5.4.3   Effect of Slot width Variation on Span-length Slots

Changes to the widths of the slots can alter the pressure difference between slot ends; this can influence the speed of the fluid through the slot and consequently affect the boundary layer. The geometry of the slots was varied in ratios of Y_1/Y_2 in an attempt to increase the fluid speed at the suction side, thus the slot width on the suction side is reduced at intervals while the chordal slot width was fixed at $Y_1=2\%$ (0.02c). Y_1 represents the chordal slot width while Y_2 represents the

width of the side slots (see Fig. 5.29). With results for $Y_1/Y_2=1$ already established, the effect of the slot width variation on aerodynamic forces for four additional configurations i.e. $Y_1/Y_2=1.25$, $Y_1/Y_2=1.5$, $Y1/Y_2=1.75$ and $Y_1/Y_2=2$ (for all configurations $Y_1=2\%$) was investigated.
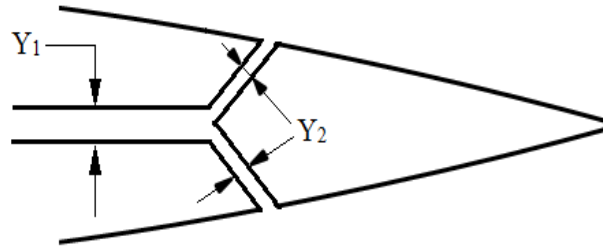
Figure 5.29: Variation of slot width on TS aerofoil.

This investigation was done for TS (X=70%) and MTS (X=45% and X=70%) aerofoils at Re=230x10^3; AoA=8°, 12°, 16°, and 20°; and slot slope ψ=55°. The slot width variation ratio Y_1/Y_2 was confined to the limit to which the slot Y_2 can be fabricated on a NACA0018 aerofoil of 0.25m chord length. The result is illustrated in Fig. 5.30. It was observed that at 8° AoA, reducing the slot width Y_2 (increasing Y_1/Y_2) of TS aerofoil led to a linear increase in the lift to drag ratio. The L/D ratio increased from 2.4% at $Y_1/Y_2=1.25$ to 12.1% at $Y_1/Y_2=2$. At 12° AoA, only $Y_1/Y_2=1.25$ had a positive effect (0.5% increase in L/D). Further increase in angles of attack and Y_1/Y_2 resulted in a decrease in L/D ratio; an average of 3.5% decrease between $Y_1/Y_2=1$ and $Y_1/Y_2=2$ at 16° AoA was detected. For MTS (Fig. 5.31), increase in slot width ratio increased the L/D ratio at 8° and 12° AoA but decreased it at 16° and 20° AoA. At 12° AoA for example, the increase in L/D was linear varying from 2.5% for $Y_1/Y_2=1.25$ to 9.7% for $Y_1/Y_2=2$. In summary, none of the slot width ratio was optimum over the entire range of AoA. Increasing Y_1/Y_2 was beneficial for L/D at pre–stall AoA but had an opposite effect at post stall angles (note; S_α of TS and MTS are 12° and 14° respectively). The decrease in L/D at post stall AoA is due to the

reduction of flow velocity in the slot at high AoAs. Therefore, since increase in L/D could not be guaranteed over the entire range of AoA, the initial slot width ratio $Y_1/Y_2=1$ was chosen.
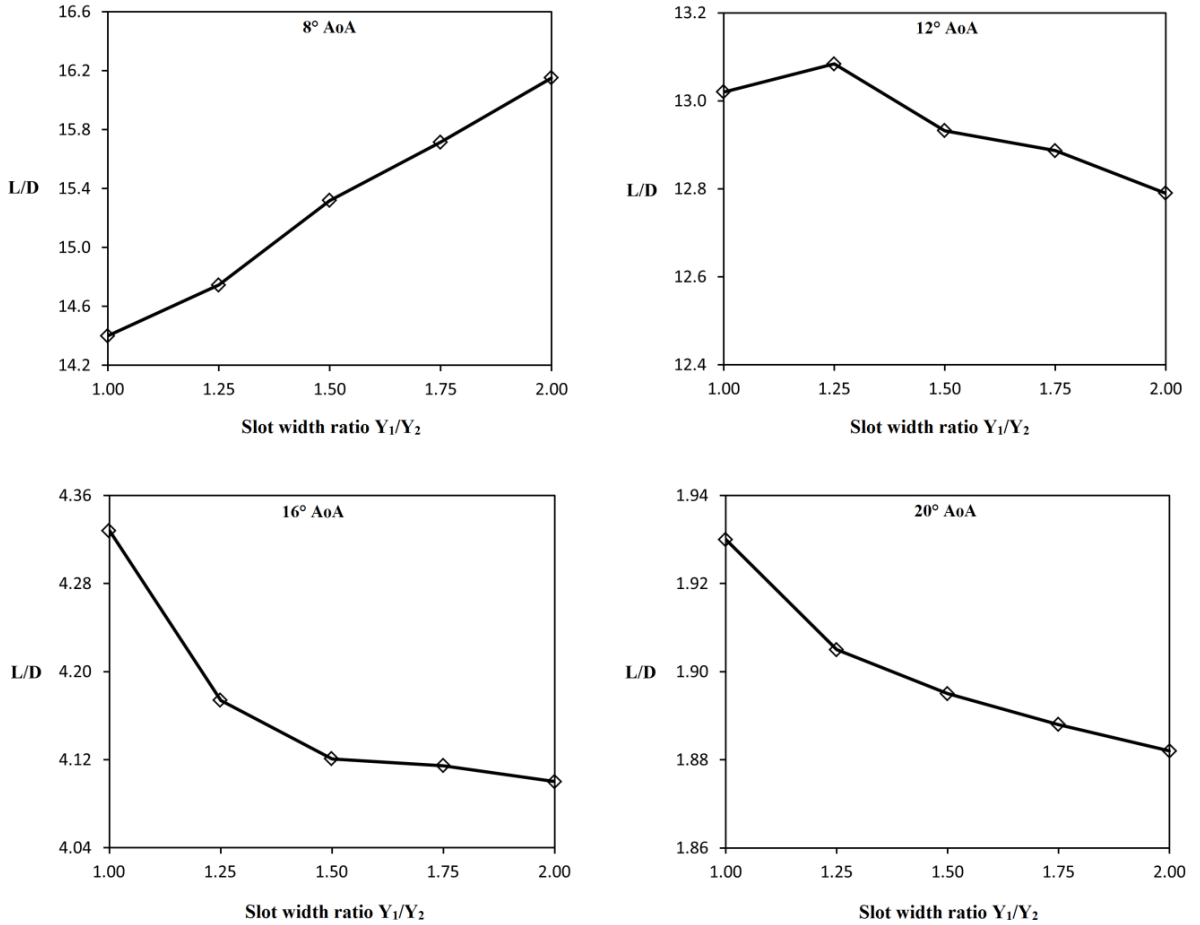
Figure 5.30: Variation of slot width for TS (X=70%).
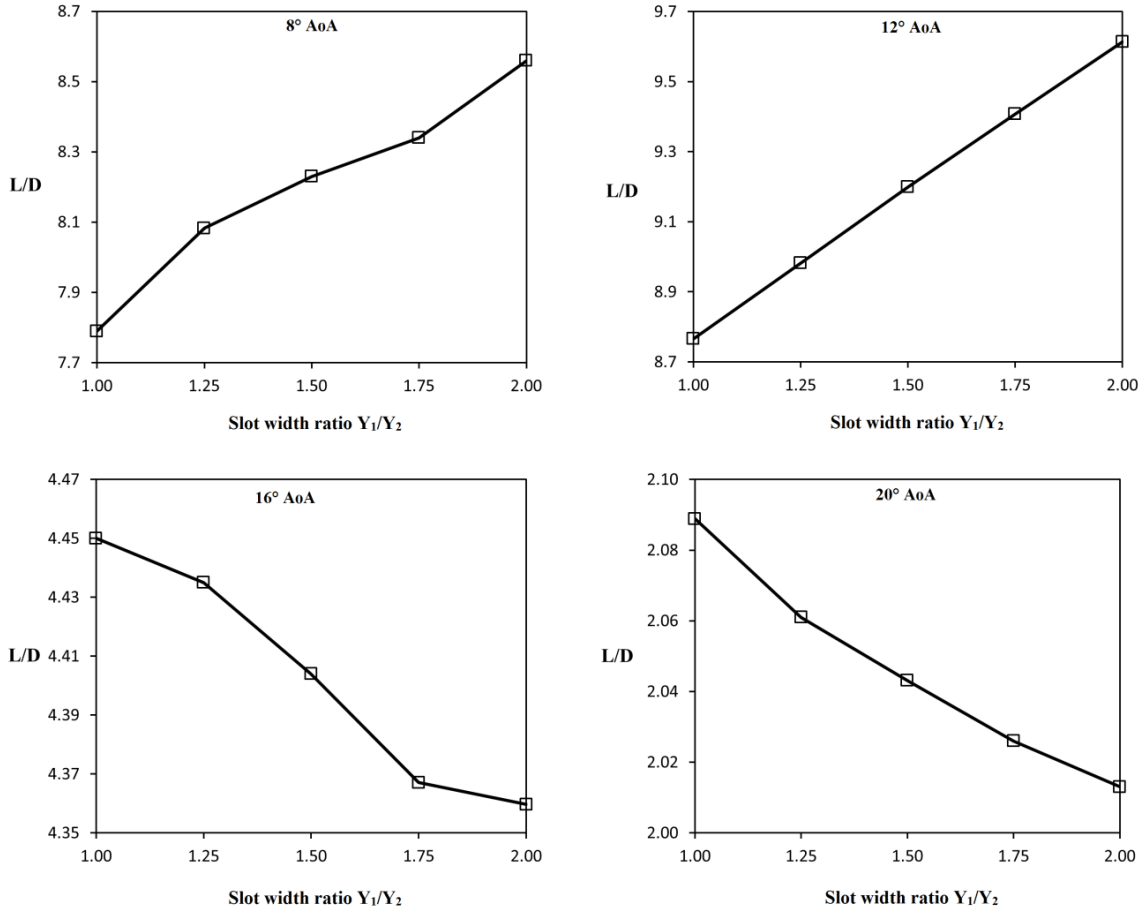
Figure 5.31: Variation of slot width for MTS (X=45% and X=70%)

5.4.4 Effect of Slot Slope on Span-length Slots

In this section, the influence of the slot slope ψ on the aerodynamic efficiency was investigated for Y_1/Y_2=1. The following values of slope angles were considered ψ 15°, 35°, 55°, and 70°. With $\psi = 55°$ initially determined, modification of the slot slope to the other desired angles was achieved by fixing the slot exit point X on the pressure and suction side and varying the point at which they both connect with the chordal slot. Fig. 5.32 illustrates the effect of the slot slope at a pre–stall and post–stall AoA ($\alpha = 8°$ and $\alpha = 16°$). The result indicates that the highest L/D ratio corresponds with the lowest slot slope, $\psi = 15°$. When the slot slope was decreased from $\psi = 55°$ to $\psi = 15°$; an average of 9% increase in L/D of TS and MTS was detected at $\alpha = 8°$, on the other hand at $\alpha = 16°$ there was a 4.6% and 3% increase in L/D of TS and MTS respectively. Fig. 5.33

shows a 2D pictorial view of the velocity contour around the MTS aerofoil with various slot slopes at 8° AoA. Due to the pressure difference between the pressure and suction sides, fluid flow was only detected in the chord slot and in the side slots in the top–half. By decreasing the slot slope, the fluid jet leaving the slot in the top–half becomes tangential to the aerofoil surface thus, delivering the fluid into the boundary layer which leads to an increase in L/D [159], while perpendicular blowing (increasing slot slope) on the other hand had an opposite effect.
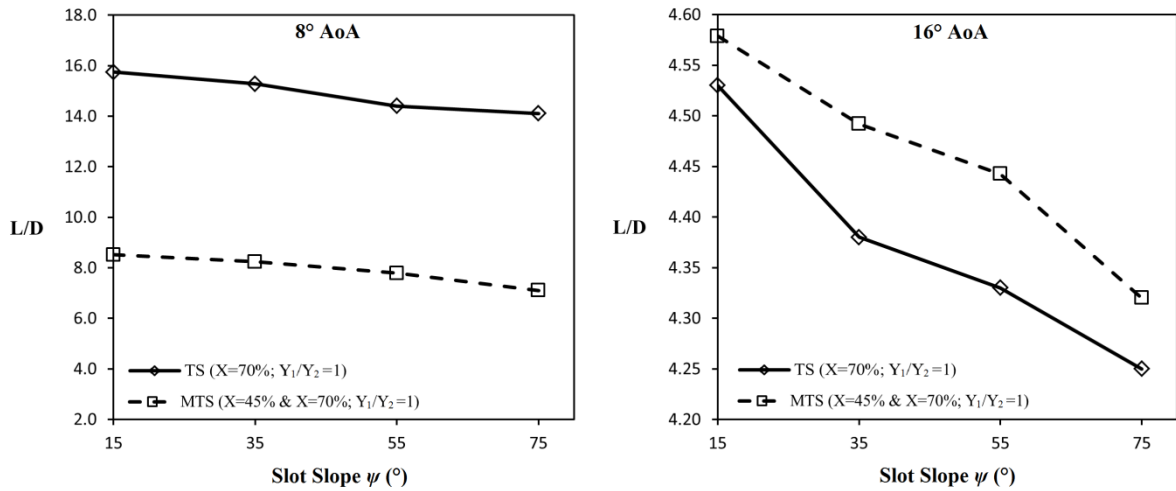
Figure 5.32: Variation of slot slope.
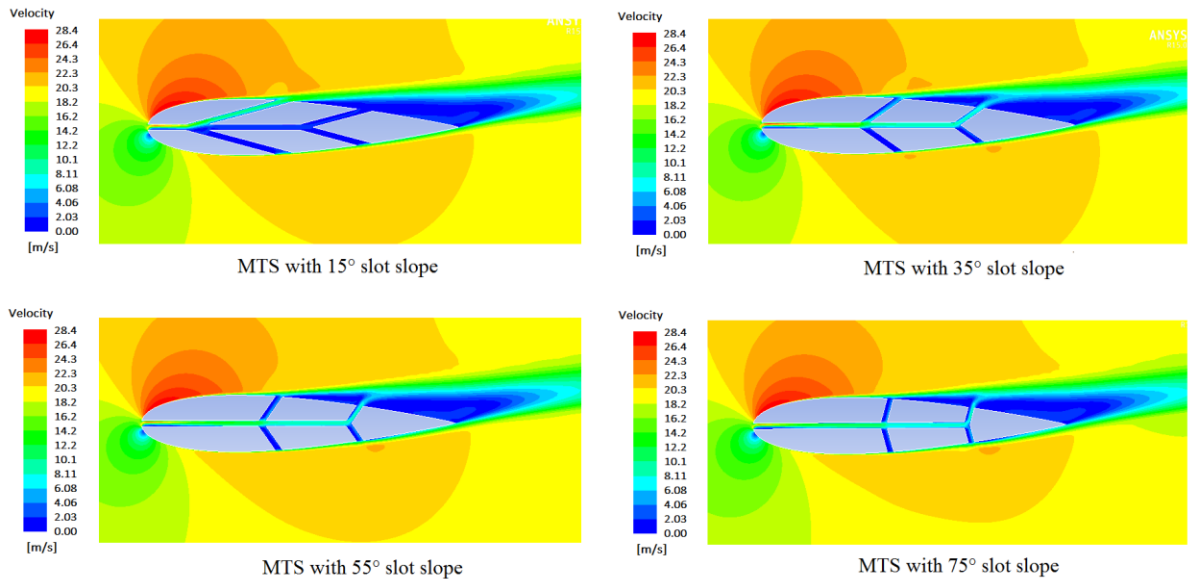
Figure 5.33 Velocity contours for MTS for various slot slope at 8° AoA.

99

5.4.5 Combined Effect of Slot Parameters for Span–length slots

So far, a great deal of effort has been devoted to the numerical parametric study, in order to improve the performance of the span–length slotted aerofoils; TS with initial slot parameters X=70%, Y_1/Y_2=1 and $\psi = 55°$, and MTS with slot parameters X=45%, X=70%, Y_1/Y_2=1 and $\psi = 55°$. Therefore, in this section the combined effect of the preferred slot parameters (from the individual slot geometric alterations) on the aerodynamic efficiency of these aerofoils over the entire range of AoA ($\alpha = 0°$ to $\alpha = 20°$) was examined. So far, slot positions X=45% and X=70% have been considered (MTS and TS cases) in order to observe single and multiple slot scenarios. Upon further parametric study of slot width variation and slope, the slot slope $\psi = 15°$ was selected because it increased L/D ratio at both pre stall and post stall AoAs, unlike in cases of slot width variation. Thus the slot slope was the major slot geometric parameter that differed from the initial configuration. Fig. 5.34 shows the L/D ratio of TS (X=70%) and MTS (X=45% and X=70%) of slot geometric parameters Y_1/Y_2=1, $\psi = 15°$. The figure shows that there was a 9% increase in maximum L/D ratio of TS ($\alpha = 8°$), and a 9.5% increase in maximum L/D ratio of MTS ($\alpha = 10°$) from their initial configuration of $\psi = 55°$. However, their overall performance was still less than that of the plain NACA0018 aerofoil.
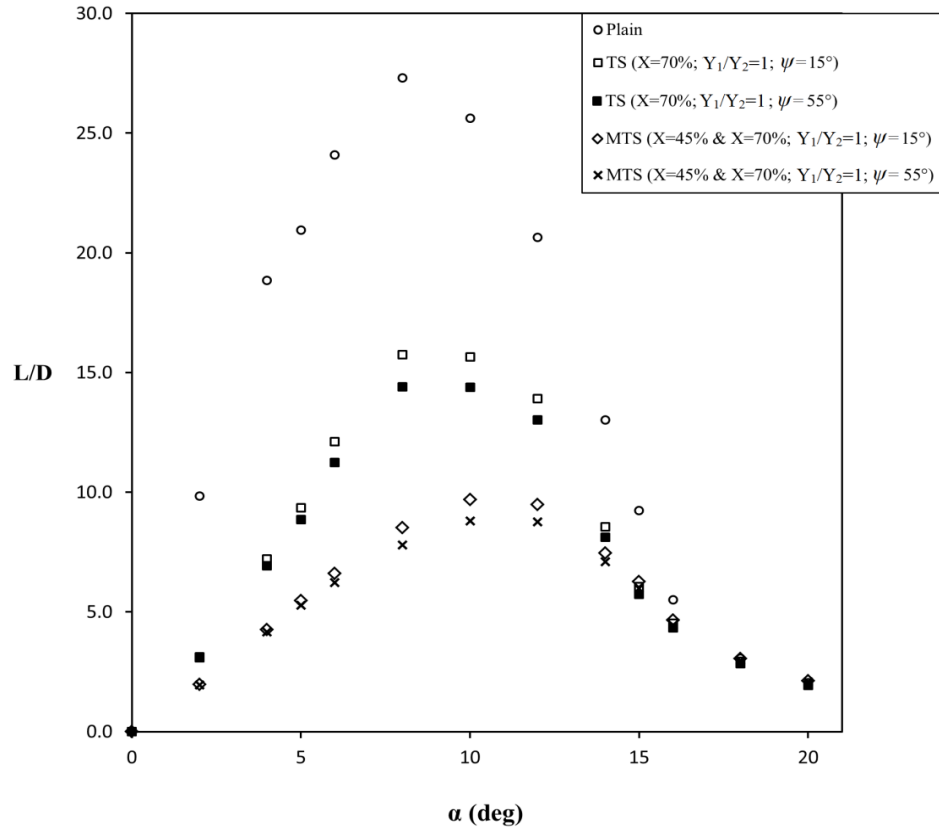
Figure 5.34: Final configuration of span-length slot parameters.

5.5 Effect of Spanwise Patterned Slots

The slots investigated so far all traversed the span of the NACA0018 (span–length slots). However, in order to create a similar slot layout to that of the Shenzhen ramjet rotors, the slots were patterned along the span. TS and MTS aerofoils consisting of patterned slots of parameters $Y_1/Y_2=1(Y_1= Y_2= 0.02c)$, $\psi = 15°$ were manually fabricated in the workshop. Figure 5.35 shows a 3D CAD model of the new TS and MTS with patterned slots. These new models represent the final configuration from the slot parametric study. The aerodynamic forces of the aerofoils were then measured in the wind tunnel.

(a) MTS Patterned Slots   **(b) TS Patterned Slots**
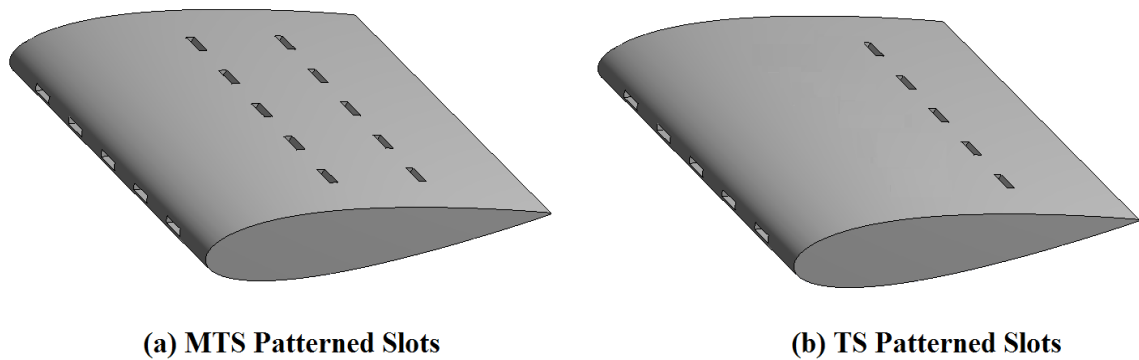
Figure 5.35: Patterned slot model.

5.5.1   Physical Model

The two new variants of TS and MTS were made from Styrofoam like the others (section 3.1.1), and the workshop fabrication process was similar to some degree. Segments of plane and slotted NACA0018 are bonded together to form these aerofoils; resulting in rows consisting of plane and slot regions alternating along the span, hence the term spanwise patterned slots. There are a total 5 slot segments and 6 plane segments, each slot segment is 20mm wide (0.08c) along the span. The plain segments at both ends of the span are 40mm wide (0.16c) while the ones between successive slots are 30mm wide (0.12c) (see Fig.5.36), this implies that the total slot volume was cut down by 60%. The chord length (250mm), and span (300mm) remained the same, other slot parameters are; $Y_1/Y_2=1(Y_1= Y_2= 0.02c)$ and $\psi = 15°$. Fig. 5.37 shows the bonding process of the new MTS aerofoil with patterned slots.
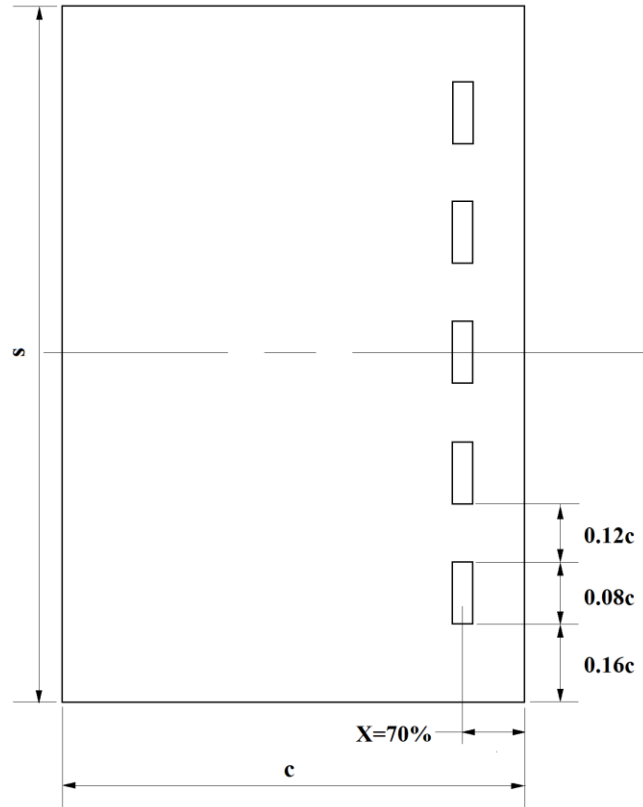
Figure 5.36 Top view of TS showing dimensions patterned slots.

Figure 5.37: Bonding Process of MTS with spanwise patterned slots.

5.5.2 Force Analysis

The effect of the patterned slots on aerodynamic forces was investigated by wind tunnel test on the newly fabricated aerofoils at Re=230x10^3. Wind tunnel test was preferred over numerical technique because the initial numerical set up of the model geometry is 2D with no spanwise thickness. Due to the geometry of the patterned–slot models, a numerical simulation (3D) will be computationally expensive and will require an additional validation stage for the numerical set–up. Fig. 5.37 to Fig. 5.39 shows the C_L, C_D and L/D curves of the pattern–slotted TS and MTS plotted against AoA.
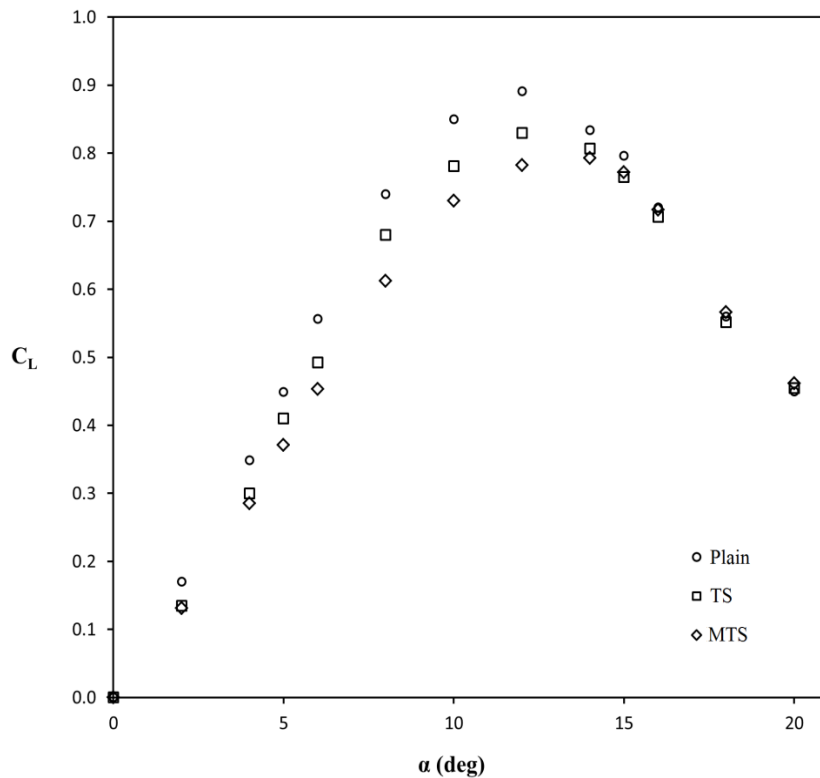
Figure 5.38: Lift Coefficient Comparison of Plain and patterned Slots
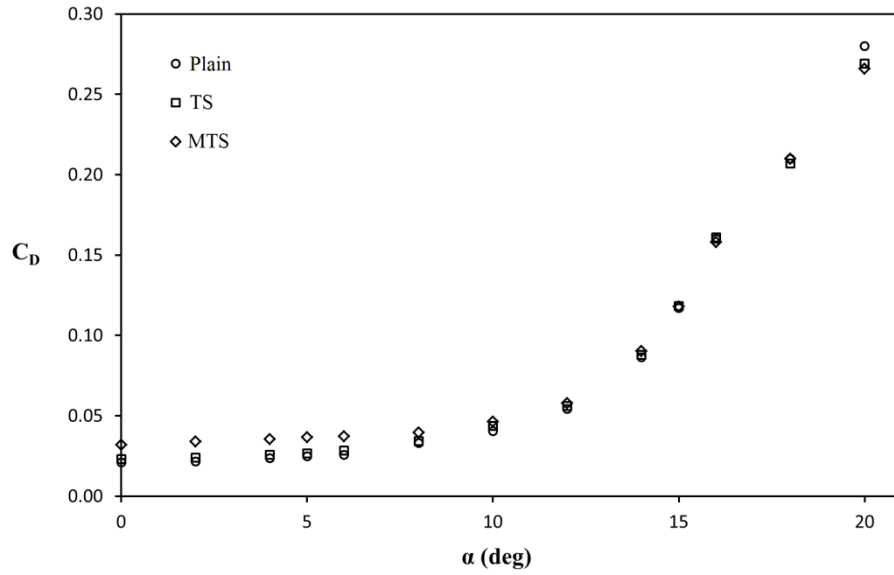
Figure 5.39: Drag Coefficient Comparison of Plain and patterned Slots.
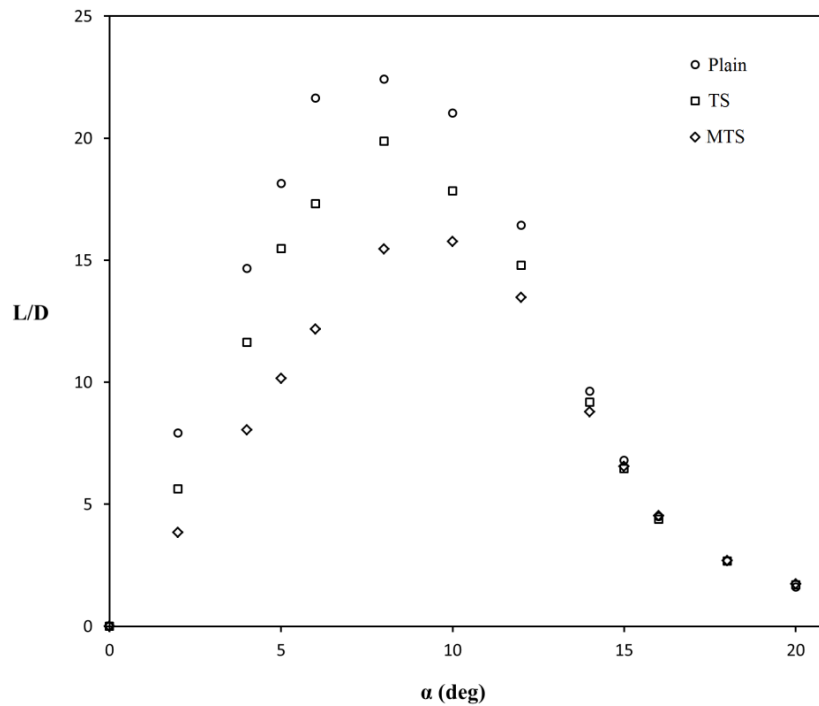
Figure 5.40: Lift–drag ratio Comparison of Plain and patterned Slots.

The result indicates that there is an improvement in performance compared to the span–length slot configuration; a 60% increase in TS and 50% increase in MTS. This was mainly as a result

of decrease in slot induced drag due to reduction in slot volume in the patterned slot configuration. In addition, between 16° to 20° AoA the MTS showed an average of 2.5% higher L/D compared to the Plain aerofoil. Despite the increase in L/D brought about by the patterned slots, the L/D ratio of plain aerofoil was still significantly higher, especially between 0° to 14° AoA. From the investigation it can be concluded that the suggested slot layout will not improve the aerodynamic performance of the aerofoil. However, the aerodynamic performance could be improved by changing the slot layout, most importantly the orientation of the slot on the pressure side of the aerofoil. With the current orientation, the slot (on the pressure side) is inclined toward the trailing edge and away from the flow stream, thus only a small volume of fluid flows into it. This volume of fluid lacks the momentum sufficient to stimulate the boundary layer on the suction side.

5.6 Summary

In this chapter, the results from wind tunnel test and CFD simulation to investigate the effects of slot position and geometric parameters on aerodynamic performance of a slotted NACA0018 has been discussed and compared with a plain NACA0018. The key point are summarised below;

- The force coefficients (C_L and C_D) and L/D curves of LS, MS and TS shows that the closer the slot location is to the leading edge the more detrimental it is to aerodynamic performance. After maximum C_L point, a slower rate of decrease in C_L gradient was detected in the slotted aerofoils.

- The presence of the span–length slots at X=45% and X=15% (MS and LS) led to a shift in stall angle S_α beyond that of the plain aerofoil; from $S_\alpha = 12°$ for the plain to $S_\alpha = 14°$ and $S_\alpha = 15°$ for MS and LS respectively.

- Span–length slots at multiple positions on the NACA0018 aerofoil (LMS, LTS, MTS and LMTS) were ineffective in improving the overall L/D performance beyond that of TS and plain aerofoil.

- For TS and MTS, increasing the slot width ratio Y1/Y2 led to an increase in L/D at pre–stall AoAs, but had an opposite effect at post–stall angles. On the other hand, reducing the slot slope ψ increased the L/D in the entire range of AoA, but lesser in post stall AoAs.

- Spanwise patterned slots of parameters Y1/Y2=1; 15° indicated a 60% and 50% increase in L/D of TS and MTS respectively, compared to their span–length slot counterpart. Despite this increase, the L/D ratio of plain aerofoil was still significantly higher, especially between 0° to 14° AoA.

Chapter 6

6. Conclusion

The influence of a unique slot layout on the aerodynamic performance of a NACA0018 aerofoil has been successfully studied using experimental and numerical methods. The effect of the slot position was studied using 2D wind tunnel test smoke visualization and CFD. The wind tunnel set up was validated by comparing its results with two other published studies on the same aerofoil profile at low Reynolds number. Furthermore, the effect of slot geometric parameters such as, slot width, slot slope and multiple slot positions on span–length slots was analysed using CFD flow simulations. The k–ω SST turbulence model which is known for its accuracy in boundary layer flows with large adverse pressure gradient and flow separations was chosen. Comparison between the numerical and experimental values shows that the chosen turbulent model demonstrated good accuracy in solving the flow. Based on the results of the parametric study, two new aerofoils with spanwise patterned slots were fabricated and tested in the wind tunnel. The study was carried out on the airfoils between $92\text{x}10^3$ to $230\text{x}10^3$ chord Reynolds numbers and angles of attack $0°$ to $20°$. The major finding from this study are summarised as follows:

The effect of three different span–length slot positions (X=15%, X=45% and X=70%) on aerodynamic performance was studied both experimentally and numerically. The results showed that the closer the side slot location is to the leading edge the more detrimental it is to aerodynamic performance. Thus the slot at X=15% resulted in the worst aerodynamic performance. Smoke visualization and CFD velocity contour images reveals that slot this position (X=15%) led to an early transition from lamina to turbulent flow, drag increase, and a huge

turbulent wake downstream of the slot. Similar outcome was observed in cases of aerofoils with multiple slot positions where one of the slots is located at X=15%.

In order to increase the aerodynamic performance above that of the initially tested aerofoils (LS, MS and TS) the effect of slot geometric parameters such as; multiple slot positions, slot width, slot slope, and spanwise patterned slots on the aerodynamic performance of the slotted NACA0018 was investigated. Numerical simulation was adopted for the parametric study so as to save aerofoil fabrication cost, and time required for wind tunnel test, data reduction and analysis. The results show that a combination of multiple span–length slots on the NACA0018 aerofoil (LMS, LTS, MTS and LMTS) was incapable of improving the overall L/D performance beyond that of TS and plain aerofoil. With results for $Y_1/Y_2=1$ already established, the effect of the slot width variation on L/D for four additional width ratios i.e. $Y_1/Y_2=1.25$, $Y_1/Y_2=1.5$, $Y1/Y_2=1.75$ and $Y_1/Y_2=2$ (for all configurations $Y_1=2\%$) was investigated. Results show that increasing the slot width ratio $Y1/Y2$ was effective in increasing L/D at pre–stall AoAs, but had an opposite effect at post–stall angles. The effect of slot slope ψ on the aerofoil L/D was investigated at slot slope; 15°, 35°, 55°, and 70°. It was observed that a reduction in the slot slope ψ increased the L/D in the entire range of AoA, but lesser in post–stall AoAs.

A final slotted NACA0018 aerofoil configuration consisting of spanwise patterned slots with slot parameters $Y_1/Y_2=1$ and $\psi = 15°$ was fabricated and tested. The patterned slots were fabricated on both TS and MTS configurations due to their L/D advantage over the other slotted aerofoil configurations. The total slot volume of each spanwise patterned aerofoil was 60% less than its span–length slotted configurations. The wind tunnel test results indicated that there was a 60% and 50% increase in L/D of patterned TS and MTS respectively when compared to their span–length slot counterpart. Also, between 16° to 20° AoA the MTS showed an average of 2.5% higher L/D compared to the plain aerofoil. Despite the increase in L/D brought about by the

reduction in slot induced drag in the patterned slots, the L/D ratio of plain aerofoil was still significantly higher, especially between 0° to 14° AoA.

In conclusion, the performance of slotted NACA0018 aerofoils has been compared with a plain NACA0018 aerofoil. It is important to mention that the suggested slot layout and its geometric alterations did not improve the overall aerodynamic performance of the slotted NACA0018 aerofoil beyond that of the plain NACA0018 aerofoil. Slot induced drag, early transition from lamina to turbulent flow, large turbulent wake downstream of the slots and the slot orientation on the pressure side were responsible for the poor performance of the slotted aerofoil. Thus, this particular slotted airfoil cannot be recommended to be used as a vertical axis wind turbine rotor.

6.1 Future Work

For the present slot configuration examined in this work, the slot orientation on the pressure side of the aerofoil makes it difficult for the slot to take full advantage of the high static pressure and flow stream direction (on the pressure side) to deliver higher momentum jets into the suction side in order to adequately stimulate boundary layer on. Therefore, in order to improve the aerodynamic performance of the aerofoil, the slot layout has to be altered in such a way that the slot slope on the pressure side is inclined towards the leading edge. Upon improving the aerodynamic performance, a full scale model vertical axis wind turbine with the new slotted aerofoils as rotors should be built, and its torque performance examined over 360° angle of attack at low wind speed.

References

[1]   "BP Statistical Review of World Energy June 2011," 2011.

[2]   J. L. Seitz, *Global Issues: An Inroduction*, 3rd ed. Blackwell Publishing, 2008.

[3]   International Energy Agency, "2014 Key World Energy STATISTICS," 2014.

[4]   J. Twidell and T. Weir, *Renewable Energy Resources*, 12th ed. 2010.

[5]   "BP Statistical Review of World Energy June 2014 About this review," no. June, 2014.

[6]   "GWEC. Global wind report – annual market update 2013.," *Brussels, Belgium: Global Wind Energy Council*, 2013.

[7]   M. Irwanto, N. Gomesh, M. R. Mamat, and Y. M. Yusoff, "Assessment of wind power generation potential in Perlis, Malaysia," *Renew. Sustain. Energy Rev.*, vol. 38, pp. 296–308, 2014.

[8]   M. Islam, D. Ting, and A. Fartaj, "Aerodynamic models for Darrieus-type straight-bladed vertical axis wind turbines," *Renew. Sustain. Energy Rev.*, vol. 12, no. 4, pp. 1087–1109, May 2008.

[9]   F. Balduzzi, A. Bianchini, E. A. Carnevale, L. Ferrari, and S. Magnani, "Feasibility analysis of a Darrieus vertical-axis wind turbine installation in the rooftop of a building," *Appl. Energy*, vol. 97, pp. 921–929, Sep. 2012.

[10]   J. C. Lin, *Review of research on low-profile vortex generators to control boundary-layer separation*, vol. 38. 2002.

[11]   M. Gad-el-hak, "Flow Control: Passive, Active and Reactive Flow Management," *Cambridge Univ. Press. London*, 2000.

[12]   S. A.-F. R. Wahidi, W. Chakroun, "The behavior of the skin-friction coefficient of a

turbulent boundary layer flow over a flat plate with differently configured transverse square grooves," *Exp. Therm. Fluid Sci.*, vol. 30, pp. 141–152, 2005.

[13] J.C. Lin and F.G. Howard, "Turbulent flow separation control through passive techniques," *(AIAA-1989-976).*, 1989.

[14] T. A. Harris and J. G. Lowry, "Pressure distribution over an NACA 23012 airfoil with a fixed slot and a slotted flap," *Report No. 732, NACA*, 1941.

[15] F. E. Weick and J. A. Shortal, "The effect of multiple fixed slots and a trailing-edge flap on the lift and drag of a clark Y airfoil," *Report No. 427, NACA*, pp. 531–536, 1932.

[16] J. F. Donovan, L. D. Kral, and A.W. Cary, "Active flow control applied to an airfoil," *AIAA Pap.*, pp. 98–0210, 1998.

[17] V. Skarolek and S. J. Karabelas, "Energy efficient active control of the flow past an aircraft wing: RANS and LES evaluation," *Appl. Math. Model.*, vol. 40, no. 2, pp. 700–725, 2016.

[18] G. Zhao and Q. Zhao, "Parametric analyses for synthetic jet control on separation and stall over rotor airfoil," *Chinese J. Aeronaut.*, vol. 27, no. 5, pp. 1051–1061, 2014.

[19] M. L. Hong Chen, "Wind generator with water float sail," 8742613, 2014.

[20] D. Berry, "Innovation and the price of wind energy in the US," *Energy Policy*, vol. 37, no. 11, pp. 4493–4499, Nov. 2009.

[21] "Small-scale wind energy Policy insights and practical guidance Table of Contents," *Carbon Trust*, pp. 1–40, 2008.

[22] E. Sesto and C. Casale, "Exploitation of wind as an energy source to meet the world's electricity demand," *J. Wind Eng. Ind. Aerodyn.*, vol. 74–76, pp. 375–387, Apr. 1998.

[23] D. H. Wood, *Small wind turbines: analysis, design and application.* London: Springer,

2011.

[24] S. O. Olayinka and O. A. Olaolu, "Assessment of wind energy potential and the economics of wind power generation in Jos, Plateau State," *Niger. Energy Sustain Dev*, vol. 16, pp. 78–83, 2012.

[25] M. Abbes and J. Belhadj, "Investigation of wind characteristics and wind power potential in El-Kef region, Tunisia," in *In: 8th international multi-conference. Systems, Signals and Devices*, 2011, pp. 1–10.

[26] J. Peinke, P. Schaumann, and S. Barth, *Wind Energy*. Springer Berlin Heidelberg, 2007.

[27] K. Sopian, M. Y. H. Othman, and a. Wirsat, "The wind energy potential of Malaysia," *Renew. Energy*, vol. 6, no. 8, pp. 1005–1016, 1995.

[28] T. L. Tiang and D. Ishak, "Technical review of wind energy potential as small-scale power generation sources in Penang Island Malaysia," *Renew. Sustain. Energy Rev.*, vol. 16, no. 5, pp. 3034–3042, 2012.

[29] N. Masseran, "Evaluating wind power density models and their statistical properties," *Energy*, vol. 84, pp. 533–541, 2015.

[30] M. R. Islam, R. Saidur, and N. A. Rahim, "Assessment of wind energy potentiality at Kudat and Labuan, Malaysia using Weibull distribution function," *Energy*, vol. 36, no. 2, pp. 985–992, 2011.

[31] M. F. Akorede, M. I. Mohd Rashid, M. H. Sulaiman, N. B. Mohamed, and S. B. Ab Ghani, "Appraising the viability of wind energy conversion system in the Peninsular Malaysia," *Energy Convers. Manag.*, vol. 76, pp. 801–810, 2013.

[32] N. Masseran, a. M. Razali, K. Ibrahim, and W. Z. Wan Zin, "Evaluating the wind speed persistence for several wind stations in Peninsular Malaysia," *Energy*, vol. 37, no. 1, pp. 649–656, 2012.

[33]　T. Khatib, K. Sopian, A. Mohamed, and M. Z. Ibrahim, "Sizing of a wind charger at minimum cost for remote housing electrification: A case study for nine coastal sites in Malaysia," *Energy Build.*, vol. 51, pp. 185–190, 2012.

[34]　R. Nurhayati, "Current Situtation of Wind Energy in Malaysia (2010)," pp. 1–4, 2010.

[35]　J. K. Kaldellis and D. Zafirakis, "The wind energy (r)evolution: a short review of a long history," *Renew. Energy*, vol. 36, pp. 1887–901, 2011.

[36]　J. Yen and N. Ahmed, "Improving safety and performance of small-scale vertical axis wind turbines," *Proc Eng*, vol. 49, pp. 99–106, 2012.

[37]　A. Hamdan, F. Mustapha, K. A. Ahmad, and A. S. Mohd Rafie, "A review on the micro energy harvester in Structural Health Monitoring (SHM) of biocomposite material for Vertical Axis Wind Turbine (VAWT) system: A Malaysia perspective," *Renew. Sustain. Energy Rev.*, vol. 35, pp. 23–30, 2014.

[38]　M. M. Aslam Bhutta, N. Hayat, A. U. Farooq, Z. Ali, S. R. Jamil, and Z. Hussain, "Vertical axis wind turbine – A review of various configurations and design techniques," *Renew. Sustain. Energy Rev.*, vol. 16, no. 4, pp. 1926–1939, May 2012.

[39]　Noll R. B. and Ham N. D., "Effects of Dynamic Stall on SWECS," *J. Sol. Eng.*, vol. 104, pp. 96–101, 1982.

[40]　Laneville A. and Vittecoq P., "Dynamic Stall: The Case of Vertical Axis Wind Turbine," *J. Sol. Eng.*, vol. 108, pp. 141–145, 1986.

[41]　T. C. Corke and F. O. Thomas, "Dynamic Stall in Pitching Airfoils: Aerodynamic Damping and Compressibility Effects," *Annu. Rev. Fluid Mech.*, vol. 47, pp. 479–505, 2015.

[42]　J. G. Leishman, "Challenges in modelling the unsteady aerodynamics of wind turbines," *Wind Energy*, vol. 5, no. 2–3, pp. 85–132, 2002.

[43]   N. Fujisawa and M. Takeuchi, "Flow Visualization and PIV Measurement of Flow Field around a Darrieus Rotor in Dynamic Stall," *J. Vis.*, vol. 1, no. 4, pp. 379–386, 1998.

[44]   C. J. S. Ferreira, H. Bijl, G. Van Bussel, and G. Van Kuik, "Simulating Dynamic Stall in a 2D VAWT: Modeling strategy, verification and validation with Particle Image Velocimetry data," *J. Phys. Conf. Ser.*, vol. 75, p. 12023, 2007.

[45]   C. Simão Ferreira, G. Kuik, G. Bussel, and F. Scarano, "Visualization by PIV of dynamic stall on a vertical axis wind turbine," *Exp. Fluids*, vol. 46, pp. 97–108, 2008.

[46]   C. Simão Ferreira, G. Kuik, G. Bussel, and F. Scarano, "Visualization by PIV of dynamic stall on a vertical axis wind turbine," *Exp. Fluids*, vol. 46, pp. 97–108, 2009.

[47]   M. Zamani, M. J. Maghrebi, and S. R. Varedi, "Starting torque improvement using J-shaped straight-bladed Darrieus vertical axis wind turbine by means of numerical simulation," *Renew. Energy*, vol. 95, pp. 109–126, 2016.

[48]   M. A. Singh, A. Biswas, and R. D. Misra, "Investigation of self-starting and high rotor solidity on the performance of a three S1210 blade H-type Darrieus rotor," *Renew. Energy*, vol. 76, pp. 381–387, 2015.

[49]   M. Douak and Z. Aouachria, "Starting Torque Study of Darrieus Wind Turbine," *Int. J. Math. Comput. Phys. Electr. Comput. Eng.*, vol. 9, no. 8, pp. 472–477, 2015.

[50]   J. R. Baker, "Features to aid or enable self-starting of fixed pitch low solidity vertical axis wind turbines," *J. Wind Eng. Ind. Aerodyn.*, vol. 15, no. 1–3, pp. 369–380, 1983.

[51]   B. Habtamu and Y. Yingxue, "Effect of Camber Airfoil on Self Starting of Vertical Axis Wind Turbine," *J. Environ. Sci. Technol.*, vol. 4, no. 3, pp. 302–312, 2011.

[52]   F. Feng, S. Li, Y. Li, and D. Xu, "Torque Characteristics Simulation on Small Scale Combined Type Vertical Axis Wind Turbine," *Phys. Procedia*, vol. 24, pp. 781–786, Jan. 2012.

[53]   J. Gavaldà, J. Massons, and F. Díaz, "Experimental study on a self-adapting Darrieus—Savonius wind machine," *Sol. Wind Technol.*, vol. 7, no. 4, pp. 457–461, 1990.

[54]   F. M. White, *Fluid Mechanics*, Sixth. The McGraw-Hill Companies, Inc., New York, 2009.

[55]   R. K. Rajput, *A Testbook of Fluid Mechanics*, Third. S. Chand and company Ltd., 2006.

[56]   S. Armstrong, A. Fiedler, and S. Tullis, "Flow separation on a high Reynolds number, high solidity vertical axis wind turbine with straight and canted blades and canted blades with fences," *Renew. Energy*, vol. 41, pp. 13–22, 2012.

[57]   S.-J. Lee and Y.-G. Jang, "Control of flow around a NACA 0012 airfoil with a micro-riblet film," *J. Fluids Struct.*, vol. 20, no. 5, pp. 659–672, Jul. 2005.

[58]   Y. F. Lin, K. Lam, L. Zou, and Y. Liu, "Numerical study of flows past airfoils with wavy surfaces," *J. Fluids Struct.*, vol. 36, pp. 136–148, Jan. 2013.

[59]   S. G. V. Lin J.C., Howard F.G., "Small submerged vortex generators for turbulent flow separation control," *J. Spacecr. Rockets*, vol. 27, no. 5, pp. 503–507, 1990.

[60]   A. S. Jenkins L., Gorton S.A., "Flow control device evaluation for an internal flow with an adverse pressure gradient.," in *40th AIAA Aerospace Sciences Meeting and Exhibit*, 2002, pp. 2002–266.

[61]   Lin J.C., "Control of turbulent boundary-layer separation using micro-vortex generators," in *30th AIAA Fluid Dynamics Conference*, 1999, pp. 99–3404.

[62]   H. F. G. Lin J.C., Selby G.V., "Exploratory study of vortex-generating devices for turbulent flow separation control.," in *AIAA 29th Aerospace Sciences Meeting*, 1991, pp. 91–42.

[63]   L. R. Kerho M, Hutcherson S, Blackwelder RF, "Vortexgenerators used to control laminar separation bubbles," *J. Aircr.*, vol. 30, no. 3, pp. 315–9, 1993.

[64] K. X. H. Luo, W. Qiao, "Passive control of laminar separation bubble with spanwise groove on a low speed highly loaded low-pressure turbine blade," *J. Therm. Sci.*, vol. 18, no. 3, pp. 193–201, 2009.

[65] P. . Viswanath, "Aircraft viscous drag reduction using riblets," *Prog. Aerosp. Sci.*, vol. 38, no. 6–7, pp. 571–600, Aug. 2002.

[66] M. Ahmadi-Baloutaki, R. Carriveau, and D. S.-K. Ting, "Effect of free-stream turbulence on flow characteristics over a transversely-grooved surface," *Exp. Therm. Fluid Sci.*, vol. 51, pp. 56–70, 2013.

[67] G. Lachman, "Results of experiments with slotted wings," *Report No.282, NACA*, 1924.

[68] D. Greenblatt and I. J. Wygnanski, "The control of flow separation by periodic excitation," vol. 36, 2000.

[69] F. E. Weick and C. J. Wenlinger, "The Characteristics of A Clark Y wing model equipped with several forms of low-drag fixed slots," *Report No. 407, NACA*, pp. 155–161, 1932.

[70] Clarence L. Gillis and John W. McKee, "Wartime Report," *Natl. Advis. commitee Aeronaut.*, vol. 1–19, no. October, 1941.

[71] H. Beri and Y. Yingxue, "Numerical Simulation of Unsteady FLow to Show self-starting of Vertical Axis Wind Turbine Using Fluent," *J. Appl. Sci.*, vol. 11, no. 6, pp. 962–971, 2011.

[72] M. Gaunaa, F. Zahle, N. N. Sørensen, and C. Bak, "Quantification of the Effects of Using Slats on the Inner Part of a 10MW Rotor," in *Wind Energy Conference & Exhibition, EWEA, Denmark*, 2012.

[73] C. Bak, R. Bitsche, A. Yde, T. Kim, M. H. Hansen, F. Zahle, M. Gaunaa, W. J. J. Heinen, and T. Behrens, "Light Rotor: The 10MW Reference Wind Turbine," in *Proceedings of EWEA Conference, Copenhagen, Denmark*, 2012.

[74]   A. M. Ragheb and M. S. Selig, "Multi-Element Airfoil Configurations for Wind

        Turbines," in *Applied Aerodynamics Conference, Honolulu HI*, 2011.

[75]   S. Narsipur, B. W. Pomeroy, and M. S. Selig, "CFD analysis of multielement airfoils for

        wind turbines," *30th AIAA Apllied Aerodyn. Conf.*, no. June, pp. 1–18, 2012.

[76]   Ari Glezer and M. Amitay, "Synthetic Jets," *Annu. Rev. Fluid Mech.*, vol. 34, pp. 503–29,

        2002.

[77]   D. P. Jansen, "Passive Flow Separation Control on an Airfoil-Flap Model," Delf

        University of Technology, 2012.

[78]   L. M. M. Boermans, "Practical Implementations of Boundary Layer Suction for Drag

        Reduction and Lift Enhancement at Low Speed.," *Present. KATnet II Work. Ascot UK.*,

        2008.

[79]   J. S. Chawla, S. Suryanarayanan, B. Puranik, J. Sheridan, and B. G. Falzon, "Efficiency

        improvement study for small wind turbines through flow control," *Sustain. ENERGY

        Technol. ASSESSMENTS*, vol. 7, pp. 195–208, 2014.

[80]   A. G. M. Amitay, D. Smith, V. Kibens, D. Parekh, "Aerodynamic flow control over an

        unconventional airfoil using synthetic jet actuators," *AIAA J.*, vol. 39, no. 3, 2001.

[81]   M. V. R. Duvigneau, "Simulation and optimization of stall control for an airfoil with a

        synthetic jet," *Aerosp. Sci. Technol.*, vol. 10, no. 4, pp. 279–287, 2006.

[82]   A. W. Kral L. D., Donovan J. F., Cain A. B. and Cary, "Numerical Simulation of

        Synthetic Jet Actuators," *AIAA Pap.*, pp. 97–1824, 1997.

[83]   S. H. Kim and C. Kim, "Separation control on NACA23012 using synthetic jet," *Aerosp.

        Sci. Technol.*, vol. 13, no. 4–5, pp. 172–182, Jun. 2009.

[84]   S. B. Kim, W. Bong, and C. Kim, "Separation Control Mechanism ofAirfoil Using

        Synthetic Jet," vol. 21, pp. 1367–1375, 2007.

[85] D. Greenblatt, M. Schulman, and A. Ben-Harav, "Vertical axis wind turbine performance enhancement using plasma actuators," *Renew. Energy*, vol. 37, no. 1, pp. 345–354, Jan. 2012.

[86] N. Benard, J. Jolibois, and E. Moreau, "Lift and drag performances of an axisymmetric airfoil controlled by plasma actuator," *J. Electrostat.*, vol. 67, no. 2–3, pp. 133–139, May 2009.

[87] R. Sosa and G. Artana, "Steady control of laminar separation over airfoils with plasma sheet actuators," *J. Electrostat.*, vol. 64, no. 7–9, pp. 604–610, 2006.

[88] Mueller T. J. and DeLaurier J. D., "Aerodynamics of Small Vehicles," *Annu. Rev. Fluid Mech.*, vol. 35, pp. 89–111, 2003.

[89] S. S. Bhat and R. N. Govardhan, "Stall flutter of NACA 0012 airfoil at low Reynolds numbers," *J. Fluids Struct.*, vol. 41, pp. 166–174, 2013.

[90] S. Wang, D. B. Ingham, L. Ma, M. Pourkashanian, and Z. Tao, "Numerical investigations on dynamic stall of low Reynolds number flow around oscillating airfoils," *Comput. Fluids*, vol. 39, no. 9, pp. 1529–1541, 2010.

[91] R. Gerakopulos, M. S. H. Boutilier, and S. Yarusevych, "Aerodynamic Characterization of a NACA 0018 Airfoil at Low Reynolds Numbers," in *40th Fluid Dynamics Conference and Exhibit*, 2010, no. July, pp. 1–13.

[92] Lei Juanmian, Guo Feng, and Huang Can, "Numerical study of separation on the trailing edge of a symmetrical airfoil at a low Reynolds number," *Chinese J. Aeronaut.*, vol. 26, no. 4, pp. 918–925, 2013.

[93] B. Rasuo, "On status of wind tunnel wall correction," *25th ICAS Congr.*, pp. 1–12, 2006.

[94] M. Selig, R. Deters, and G. Williamson, "Wind tunnel testing airfoils at Low Reynolds Numbers," *49th AIAA Aerosp. Sci. ……*, no. January, 2011.

[95]   M. Selig, J. J. Guglielmo, A. P. Broeren, and P. Giguere, "Experiments on Airfoils at low Reynolds numbers," in *34th AIAA aerospace sciences meeting and exhibit*, 1996.

[96]   M. Selig, J. J. Guglielmo, A. P. Broeren, and P. Giguere, *Summary of Low-Speed Airfoil Data*, vol. 1. 1995.

[97]   A. S. S. Sudhakar, Shashank Mishra, G. Ramesh, K.T. Madhavan, "Experimental Studies on SM4308 Airfoil at Low Reynolds Number," in *Symposium on Applied Aerodynamics and Design of Aer ospace Vehicle (SAROD 2011)*, 2011.

[98]   Thomas J. Mueller and Stephen M. Batil, "Experimental Studies of Separation on a Two-Dimensional Airfoil at Low Reynolds Numbers," *AIAA J.*, vol. 20, no. 4, pp. 457–463, 1982.

[99]   D. H. Kim and J. W. Chang, "Low-Reynolds-number effect on the aerodynamic characteristics of a pitching NACA0012 airfoil," *Aerosp. Sci. Technol.*, vol. 32, no. 1, pp. 162–168, 2014.

[100] P. Selig M.S., Guglielmo J.J., Broeren A.P., and Giguere, "Experiments on Airfoils at Low Reynolds Numbers," in *34th Aerospace Sciences Meeting & Exhibit*, 1996.

[101]   and S. M. S. Lyon C.A., Broeren A.P., Giguere P., Gopalarathnam A., "Summary of Low-Speed Airfoil Data," *SoarTech Publ.*, vol. 3, 1998.

[102] Z. Yang, H. Igarashi, M. Martin, and H. Hu, "An experimental investigation on aerodynamic hysteresis of a low-Reynolds number airfoil," *46th AIAA Aerosp. Sci. ...*, pp. 1–11, 2008.

[103] R. E. Sheldahl and P. C. Klimas, "Aerodynamic characteristics of seven symmetrical airfoil sections through 180-degree angle of attack for use in aerodynamic analysis of vertical axis wind turbines. Technical Report SAND80-2114, Sandia National Laboratories," 1981.

[104]   C. Ostowari and D. Naik, "Post-stall Studies of Untwisted Varying Aspect Ratio Blades with an NACA 4415 Airfoil Section - Part I," *J. Wind Eng.*, vol. 8, no. 3, pp. 176–194, 1984.

[105]   C. Ostowari and D. Naik, "Post-stall Studies of Untwisted Varying Aspect Ratio Blades with an NACA 44XX Airfoil Section - Part II," *J. Wind Eng.*, vol. 9, no. 3, pp. 149–164, 1985.

[106]   Mallon K.J., "The NACA0018-64 Aerofoil at Low Reynolds Numbers with Application to Vertical Axis Wind Turbines - Including Turbulence Stimulation," in *11th Australasian Fluid Mechanics Conference, University of Tasmania, Hobart, Australia, 14-18 December*, 1992.

[107]   G. Bergeles, N. Athanassiadis, and A. Michos, "Aerodynamic characteristics of NACA 0012 aircraft in relation to wind generators," *Wind Eng.*, vol. 7, no. 4, pp. 247–262, 198AD.

[108]   C. Critzos, H. Heyson, and R. Boswinkle, "Aerodynamic Characteristics of NACA 0012 Airfoil Section at Angles of Attack from 0 to 180 Degrees," *Tech. Rep. TN 3361, NACA.*, 1995.

[109]   G. Massini, E. Rossi, and S. D'Angelo, "Wind tunnel measurements of aerodynamic coefficients of asymmetrical airfoil sections for wind turbine blades extended to high angles of attack," in *European Community Wind Energy Conference*, 1988, pp. 241–245.

[110]   G. Bergeles, N. Athanassiadis, and A. Michos, "Aerodynamic Characteristics of Naca 0012 Airfoil in Relation To Wind Generators," *Wind Eng.*, vol. 7, no. 4, pp. 247–262, 1983.

[111]   C. Critzos, H. Heyson, and R. Boswinkle, "Aerodynamic Characteristics of NACA 0012 Airfoil Section at Angles of Attack from 0 to 180 Degrees. Technical Report TN 3361,

NACA.," 1955.

[112] G. Massini, E. Rossi, and S. D'Angelo, "Wind tunnel measurements of aerodynamic coefficients of asymmetrical airfoil sections for wind turbine blades extended to high angles of attack," in *European Community Wind Energy Conference, Herning, Denmark,* 1988, pp. 241–245.

[113] A. Pope, "The Forces and Pressures over a NACA 0015 Airfoil Through 180 Degrees Angle of Attack. Technical Report E-102, Georgia Institute of Technology.," 1947.

[114] D. Spera, "Models of Lift and Drag Coefficients of Stalled and Unstalled Airfoils in Wind Turbines and Wind Tunnels. Technical Report NASA/CR-2008-215434, NASA.," 2008.

[115] J. Rainbird, "The Aerodynamic Development of a Vertical Axis Wind Turbine," M. Eng Thesis, School of Engineering, University of Durham, 2007.

[116] J. M. Rainbird, J. Peiró, and J. M. R. Graham, "Blockage-tolerant wind tunnel measurements for a NACA 0012 at high angles of attack," *J. Wind Eng. Ind. Aerodyn.*, vol. 145, pp. 209–218, 2015.

[117] J. B. Barlow, W. H. Rae, and A. Pope, *Low-speed wind tunnel testing*, 3 edition. New York: John Wiley & Sons, Inc, 1999.

[118] L. Kong, "Road vehicle model testing in a blockage tolerant wind tunnel," *J. Wind Eng. Ind. Aerodyn.*, vol. 57, no. 2, pp. 137–143, 1995.

[119] J. Yao, J. Wang, W. Yuan, H. Wang, and L. Cao, "Analysis on the influence of Turbulence model changes to aerodynamic performance of vertical axis wind turbine," *Procedia Eng.*, vol. 31, no. 2011, pp. 274–281, Jan. 2012.

[120] J. Yao, W. Yuan, J. Wang, J. Xie, H. Zhou, M. Peng, and Y. Sun, "Numerical simulation of aerodynamic performance for two dimensional wind turbine airfoils," *Procedia Eng.*, vol. 31, pp. 80–86, 2012.

[121] "Ansys Fluent Theory Guide," 2013.

[122] R. Howell, N. Qin, J. Edwards, and N. Durrani, "Wind tunnel and numerical study of a small vertical axis wind turbine," *Renew. Energy*, vol. 35, no. 2, pp. 412–422, Feb. 2010.

[123] B. Debnath, A. Biswa, and R. Gupta, "Computational Fluid Dynamics analysis of combined three bucket Savonious and three bladed Darrieus rotor at various overlap," *J. Renew. Sustain. Energy*, no. 1, pp. 1–13, 2009.

[124] T. J. Mueller, "Aerodynamic measurements at low Reynolds numbers for fixed wing micro-air vehicles. Presented at the RTO AVT/VKI special course on development and operation of UAVs for military and civil applications, VKI, Belgium, September 13-17, 1999."

[125] M. H. Mohamed, "Performance investigation of H-rotor Darrieus turbine with new airfoil shapes," *Energy*, vol. 47, no. 1, pp. 522–530, 2012.

[126] F. Fish, "Imaginative solutions by marine organisms for drag reduction," *Proc. Int. Symp. Seawater Drag Reduct.*, vol. 1, pp. 443–50, 1998.

[127] W. A. Timmer, "Two-dimensional low-Reynolds number wind tunnel results for airfoil NACA 0018," *Wind Eng.*, vol. 32, pp. 525–537, 2009.

[128] M. S. Selig, B. D. Mcgranahan, M. S. Selig, and B. D. Mcgranahan, "Wind Tunnel Aerodynamic Tests of Six Airfoils for Use on Small Wind Turbines Period of Performance : Wind Tunnel Aerodynamic Tests of Six Airfoils for Use on Small Wind Turbines Period of Performance :," Urbana, Illinois, 2004.

[129] W. Sutherland, "The viscosity of gases and molecular forces," *Philos. Mag.*, vol. 5, no. 36, pp. 507–531, 1893.

[130] I. Abdallah, A. Natarajan, and J. D. Sørensen, "Impact of uncertainty in airfoil characteristics on wind turbine extreme loads," *Renew. Energy*, vol. 75, pp. 283–300,

2015.

[131] K. Duraisamy, W. McCroskey, and J. Baeder, "Analysis of wind tunnel wall interference effects on subsonic unsteady airfoil flows," *J. Aircr.*, vol. 44, no. 5, 2007.

[132] K. W. McAlister and R. K. Takahashi, "NACA 0015 wing pressure and trailing vortex measurements," 1991.

[133] B. F. R. Ewald, "Wind Tunnel Wall corrections," *AGARDograph*, vol. 336, 1998.

[134] H. C. Garner, E. W. E. Rogers, W. E. A. Acum, and E. C. Maskell, "Subsonic Wind Tunnel Wall Corrections," *AGARDograph*, vol. 109, 1966.

[135] E. C. Maskell, "A Theory of Blockage Effects on Bulff Bodies and Stalled Wings in a Closed Wind Tunnel," *Aeronaut. Res. Counc. reports Memo.*, vol. no. 3400, no. AD-A955-243, pp. 1–26, 1963.

[136] T. J. Blackwell, "Subsonic Wind-Tunnel Wall Corrections on a Wing With a Clark Y-14 Airfoil," no. May, 2011.

[137] E. Daniele, "Numerical and Experimental Investigations of Low Reynolds number wind turbine airfoils under stall and post stall condistions (Ph.D thesis in Engineering)," University of Naples Federico II, 2013.

[138] I. Ross and A. Altman, "Wind tunnel blockage corrections: Review and application to Savonius vertical-axis wind turbines," *J. Wind Eng. Ind. Aerodyn.*, vol. 99, no. 5, pp. 523–538, 2011.

[139] S. M. Batill and T. J. Mueller, "Visualization of Transition in the Flow over an Airfoil Using the Smoke-Wire Technique," *AIAA J.*, vol. 19, no. 3, pp. 340–345, 1981.

[140] S. S. Dol and M. A. M. N. and M. K. Kamaruzaman, "An Improved Smoke-Wire Flow Visualization Technique," *Proc. 4th WSEAS Int. Conf. Fluid Mech. Aerodyn.*, vol. 2006, pp. 231–236, 2006.

[141] C. Curtis, A. Dunbar, and S. Y. Zhou, "Design of a Setup for Flow Visualizations," 2005.

[142] D. A. Peters, "Two-dimensional incompressible unsteady airfoil theory—An overview," *J. Fluids Struct.*, vol. 24, no. 3, pp. 295–312, Apr. 2008.

[143] P. J. Kunz, "Aerodynamics and Design for Ultra-Low Reynolds number Flight," Stanford University, 2003.

[144] M. Ariff, S. Salim, and S. Cheah, "Wall Y+ Approach for Dealing With Turbulent Flow Over a Surface Mounted Cube: Part 1–Low Reynolds Number," *Seventh Int. Conf. CFD Miner. Process Ind.*, no. December, pp. 1–6, 2009.

[145] H.F. Lam and H.Y. Peng, "Study of wake characteristics of a vertical axis wind turbine by twoand three-dimensional computational fluid dynamics simulations," *Renew. Energy*, vol. 90, pp. 386–398, 2016.

[146] J. Morgado, R. Vizinho, M. A. R. Silvestre, and J. C. Pascoa, "XFOIL vs CFD performance predictions for high lift low Reynolds number airfoils," *Aerosp. Sci. Technol.*, vol. 52, pp. 207–214, 2016.

[147] G. Bedon, S. De Betta, and E. Benini, "Performance-optimized airfoil for Darrieus wind turbines," *Renew. Energy*, vol. 94, pp. 328–340, 2016.

[148] R. Belamadi, A. Djemili, A. Ilinca, and R. Mdouki, "Aerodynamic performance analysis of slotted airfoils for application to wind turbine blades," *J. Wind Eng. Ind. Aerodyn.*, vol. 151, pp. 79–99, 2016.

[149] A. Kovacevic, "Boundary adaptation in grid generation for CFD analysis of screw compressors," *Int. J. Numer. Methods Eng.*, vol. 64, no. 3, pp. 401–426, Sep. 2005.

[150] J. F. Marchman, "Aerodynamic testing at low Reynolds numbers," *J. Aircr.*, vol. 24, no. 2, pp. 107–114, 1987.

[151] E. V Laitone, "Wind tunnel tests of wings at Reynolds numbers below 70 000," *Exp.*

Fluids, vol. 23, pp. 405–409, 1997.

[152]   M. H. Sadraey, *Aircraft Design: A Systems Engineering Approach*. Wiley, 2012.

[153]   M. Mahmood, "Flow Visualization in Wind Tunnels," in *Wind Tunnels and Experimental Fluid Dynamics Research*, Prof. Jorge Colman Lerner (Ed.), Ed. 2011, pp. 100–115.

[154]   P. Crimi and B. L. Reeves, "Analysis of leading-edge separation bubbles on airfoils," *AIAA J.*, vol. Vol. 14, no. No. 11, pp. 1548–1555, 1976.

[155]   T.-J. Wu, "Visualization of stall characteristics of airfoil using the smoke-wire technique," The University of Texas Arlington, 1992.

[156]   M. K. Phan and J. Shin, "Numerical investigation of aerodynamic flow actuation produced by surface plasma actuator on 2D oscillating airfoil," *Chinese J. Aeronaut.*, vol. 29, no. 4, pp. 882–892, 2016.

[157]   T. Cebeci, G. J. Mosinskis, and A. M. O. Smith, "Calculation of separation points in incompressible turbulent flows," *J. Aircr.*, vol. 9, no. 9, pp. 618–624, 1972.

[158]   S. Agarwal and P. Kumar, "Numerical Investigation of Flow Field and Effect of Varying Vortex Generator Location on Wing Performance," vol. 6, no. 1, pp. 11–19, 2016.

[159]   K. Yousefi and R. Saleh, "The effects of trailing edge blowing on aerodynamic characteristics of the NACA 0012 airfoil and optimization of the blowing slot geometry," *J. Theor. Appl. Mech.*, vol. 52, no. 1961, pp. 165–179, 2014.

Appendix A

Additional information regarding wind tunnel experiment
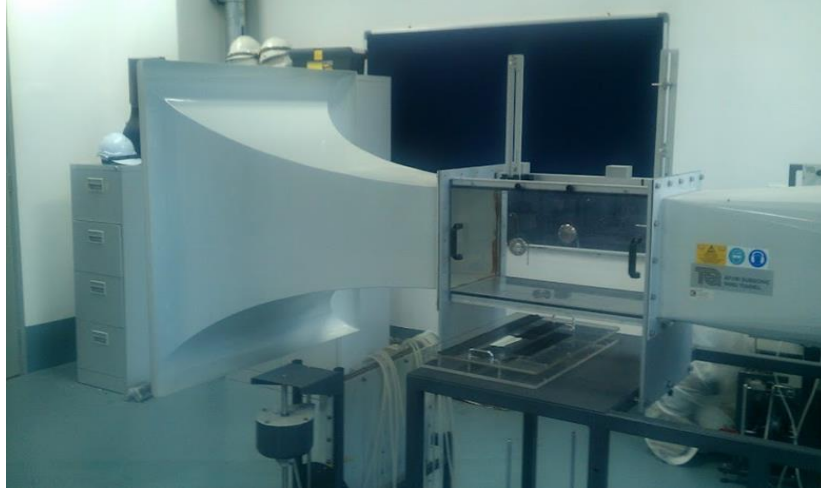
Figure A.1: The University of Nottingham Malaysia Campus subsonic the wind tunnel.

A.1 Aerofoil Fabrication

This section explains the entire process involved in making both the plain and slotted aerofoils. Extra caution is taken to ensure that the finished aerofoil conforms to the required aerofoil profile (NACA 0018). The process begins with downloading the NACA 0018 profile (coordinates) from online (see Fig B.1). The downloaded note pad file format is then converted into an excel file. In excel, the coordinates are plotted as a line graph to create the NACA 0018 shape. The plotted shape is enlarged to scale and then printed on an A4 size paper. For the sake of durability and easy handling, the printout is laminated with a plastic sheet and the aerofoil shape is cut out with a paper cutter. Then the laminated paper is placed on a 30mm x 30mm 10mm Styrofoam block and the aerofoil shape was traced out with a pen (Fig A.2 (a) and (b)). The Styrofoam block with the aerofoil shape tracing is then transferred to a vertical band saw in the workshop where a solid, plane aerofoil was cut out (Fig A.2 (a), (b) and (c)). However, producing the slotted aerofoils was far more tedious. The process starts with cutting out a plane aerofoil from a Styrofoam block as

described above. Then the slots were drawn on one end of the plane, once again the vertical band saw is used to cut out the slots from the aerofoil leaving it in pieces.
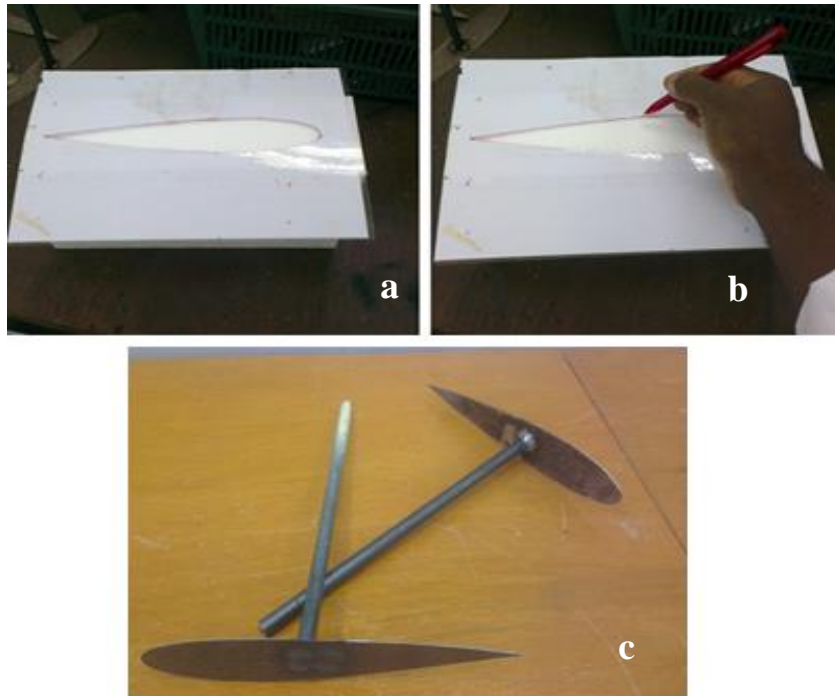
Figure A.2: (a) Laminated aerofoil cut out (b) Tracing of Aerofoil shape on a Styrofoam block (c) Steel Aerofoil Sheets.

For the purpose of force measurement in the subsonic wind tunnel, the aerofoil must have a rod connected on one end which must pass through one of the side the walls in the wind tunnel working section into a strain gauge. Four 12mm steel rods each 350m long were cut using a horizontal band saw and all ends were chaffered. Also eight NACA 0018 aerofoil shapes were cut out from steel sheets using the same technique used for cutting the aerofoil (Fig A.2 (c)). The cut out pieces of the Styrofoam that make up the slotted aerofoils were then put together and glued onto a steel sheet (aerofoil shape) using a water base adhesive. Each aerofoil required 2 steel sheets glued onto it to hold the pieces together and to connect it to the stain gauge. For a smooth surface finish on the aerofoils, aluminium foil was glued onto the surface of the aerofoils. However, the foil was unsuitable because it gets permanent indentions easily whenever an object

is place or pressed on it and this roughens the surface. To fix this problem, a plastic sheet the same used for paper lamination was used instead and it proved to be far more effective.
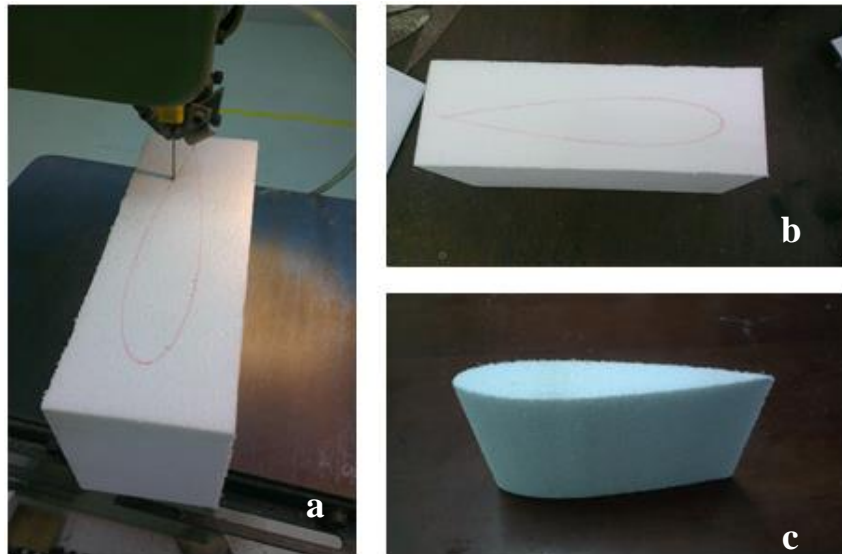
Figure A.3: (a) Vertical ban saw Cutting Aerofoil (b) Styrofoam with aerofoil tracing on (c) Cut out Plane aerofoil.

Table A.1: Technical Data of wind tunnel.

Item	Specification
Total Length of Apparatus	3700 mm
Total Depth (front to back)	1065 mm
Total Height	1900 mm
Working Section	305 mm x 305 mm x 600 mm
Air Velocity	0-36m/s
Fan Motor	AC Three-Phase variable speed
Electricity Supply	
Type	Three-Phase AC
Voltage	220V
Total Current (with all optional instruments connected)	26A

Table A.2: Technical Details of Force balance.

Item	Detail
Weight	Display Unit (with power supply): 1 kg Balance Assembly (on back plate): 5 kg
Maximum Load	10 kg (100 N) *The load cell is rated at 20 kg
Display Unit	12 VDC input
Uncertainty	±0.2 N
Power Supply	100 VAC to 240 VAC input at 1 A 50 Hz to 60 Hz 12 VDC output

Zero button
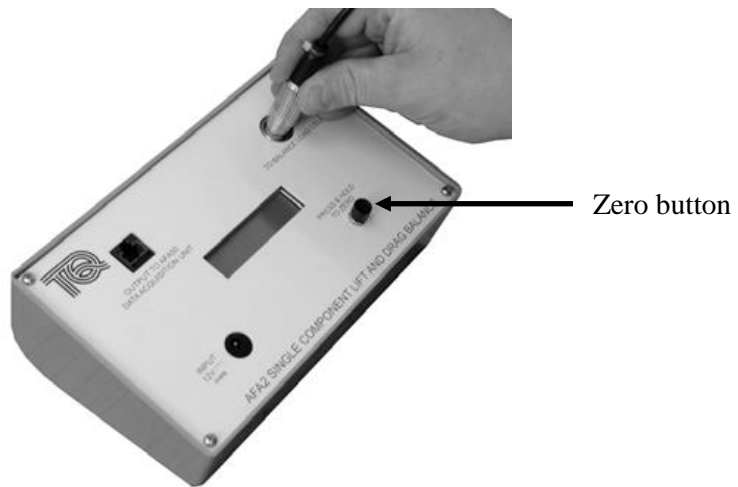
Figure A.4: Force Display Unit.
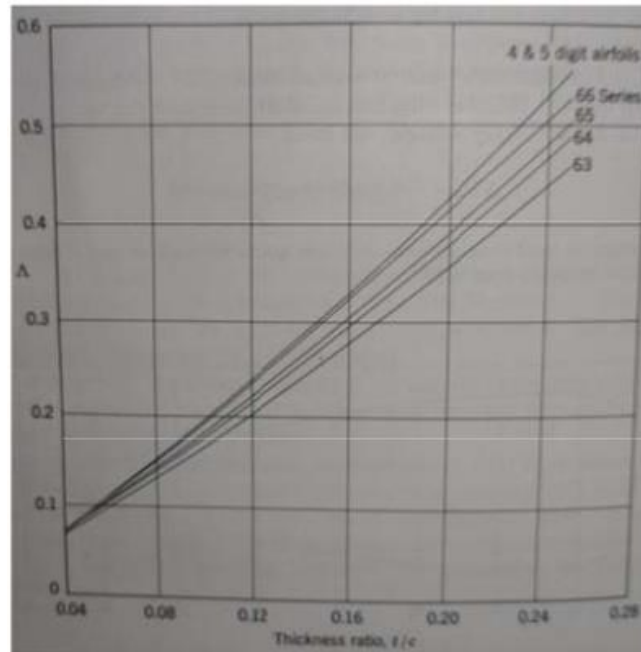
Figure A.5: Values for Shape factor for various aerofoil families [117]**.**

All models are available for 230v or 110v power, and come complete with 2kg CO2 cylinder, CO2 regulator, container of smoke oil and 5m wired remote control

Vicount Compact 1300		
Specifications (approx)		
Fluid tank size	1.3 litres	
Size	41 x 18 x 37cm	
Weight (kg)	12kg	
Power Supply	230v, 50hz	
Optional	110v, 50/60hz	
Warm up time from cold	4 minutes	
Particle Size (mmd)	0.2 - 0.3 microns	
	Standard	**High-output**
Heat Exchanger wattage	1,100 watts	2,200 watts
Running time at maximum output	40 minutes	22 minutes
Smoke output (@ 1.0m visibility)	0 - 150 m3/min	0 - 290 m3/min
Smoke oil consumption	2000ml/hr	3600ml/hr

Figure A.6: Technical data of the smoke generator.

A.2 Calibration of Test-Section

It was imperative that the aerofoil received an even velocity distribution in the wind tunnel test section. Therefore, before the commencement of test, the wind tunnel equipment was calibrated. The calibration was done in an empty test section in order to avoid induced flow by model. Two tests were carried out, they are; (1) Establishing of the Reference Velocity and (2) velocity uniformity test. In both tests caution was taken to ensure that the Pitot tube is parallel to the wind direction to avoid extraneous static pressure. Only the area in the vertical plane at the upstream and downstream (between the supposed aerofoil position) of the test section is surveyed. Results are valid only for the temperature and pressure at the time of measurement since the ambient conditions may vary.

A.3 Establishing of the Reference Velocity
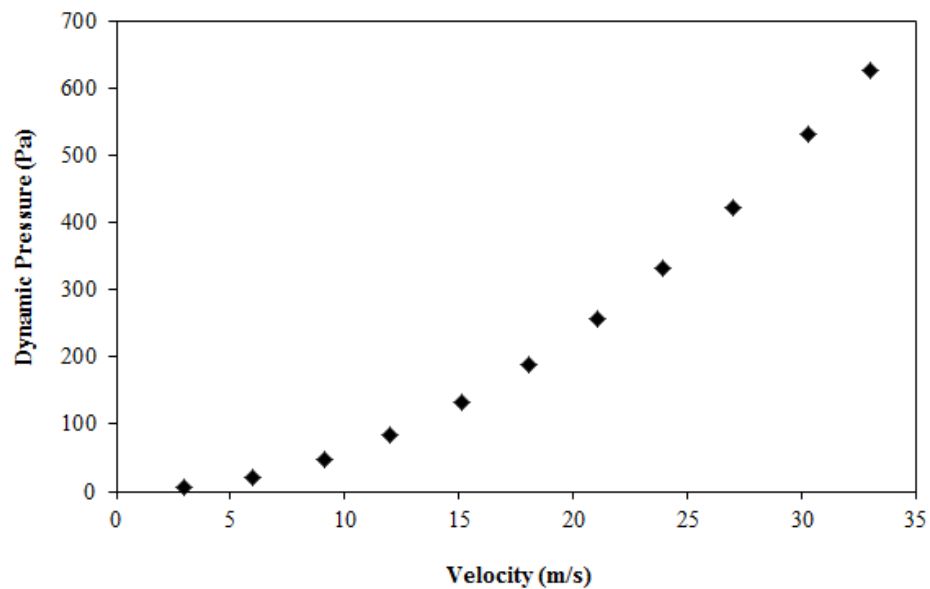
Figure A.7: Variation of Dynamic pressure with Velocity.

The velocity and dynamic pressure relationship was surveyed at the point of measurement to establish a reference velocity for further testing. The wind tunnel axial fan was switched on and ran at max speed (34m/s), and the pressure reading from the differential manometer at the

maximum speed was recorded. The fan speed was reduced at intervals of 3m/s and the corresponding manometer reading (mean values) was taken (see Fig A.7). All measurements were taken with the pitot static tube position along the centre axis of the tunnel (180 mm from the bottom) at the upstream pitot position (25mm from the inlet of the working section). By using the plot below, the velocity at the upstream pitot position can be referred to when aerofoils are placed in the working section.

A.4 Velocity Uniformity Test

The probe of the Pitot tube was positioned along the centre line of the tunnel and the fan was set to the maximum speed of about 34m/s. Then the position of the probe was moved to the floor of the test section and the velocity reading taken. The probe was moved up, away from the floor at intervals of 1mm up to 15cm position, then 20mm intervals was taken up to the centre of the test section. At each point the corresponding velocity was recorded every second for 2 minutes (radius of pitot tube was noted).
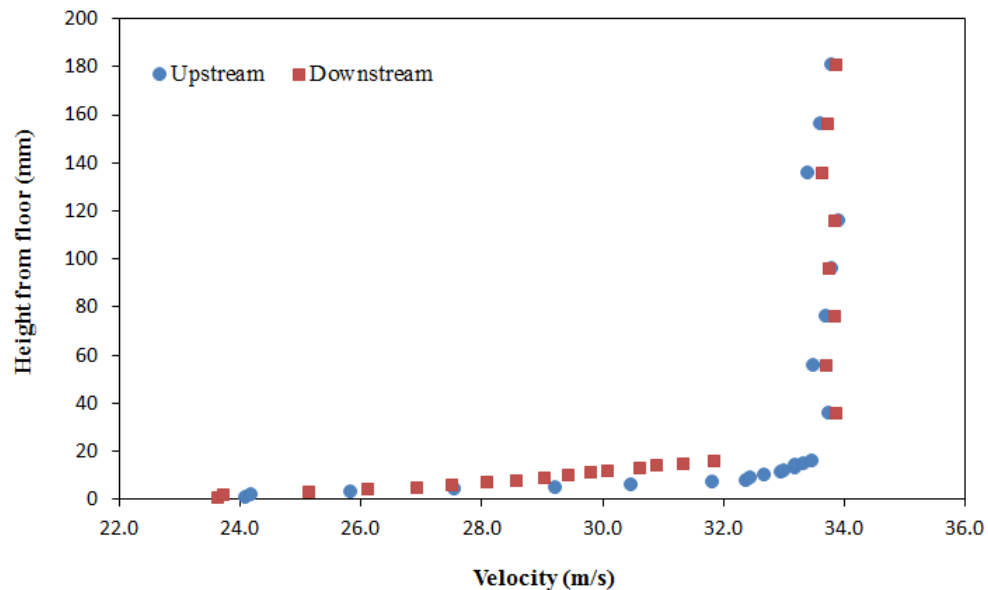
Figure A.8: Velocity distribution at upstream and downstream positions.

Fig A.8 shows a plot of height from the test section floor against velocity at the upstream and downstream pitot positions. Both curves show that a higher and fairly constant velocity is observed at the centre of the test section while a reduced velocity occurs near the floor of the test section. Thus at a height of 0 to 16mm from the floor, there was a slower increase in velocity at downstream position than in the upstream. This was as a result of boundary layer presence which makes the test section smaller at the exit, hence creating to a negative pressure gradient.

A.5 Test Section pressure gradient

A practical measure of the boundary layer estimation is expressed through displacement thickness. Therefore the laminar boundary layer thickness at the test section exit is;

$$\delta_{LB} = 1.72 \frac{x}{\sqrt{\text{Re}}} , \qquad (A.1)$$

where $x = 0.6m$ is the length of the test section. Thus the effective area of the test section exit A_2 is;

$$A_2 = (H - 2\delta_{LB}) \times (L - 2\delta_{LB}) \qquad (A.2)$$

where $H = 0.36m$ is height of the test section, $L = 0.305m$ is the test section width. The effective velocity V_2 at the test section exit is;

$$V_2 = V_1 \cdot \frac{A_1}{A_2} \qquad (A.3)$$

where V_1 is the velocity at the test section inlet whose area is $A_1 = H \cdot L$. Going by Bernoulli's equation, the effective pressure P_2 at the test section exit is:

$$P_2 = P_1 + 0.5 \cdot \rho \cdot (V_1^2 - V_2^2), \qquad (A.4)$$

where P_1 is the pressure at the test section entrance and ρ is the air density in the test section.

With P_1 and P_2 now known, the pressure gradient in the test section is;

$$p' = \frac{\Delta p}{\Delta l} = \frac{P_2 - P_1}{x} \tag{A.5}$$

A.6 Test Section Turbulence Intensity

The turbulence intensity in the test section was measured using a hot-wire anemometer. The hot-wire probe was positioned at the centre of the test section with its orientation perpendicular to the flowstream. Turbulence Intensity is defined as the rms (standard deviation) variation from the mean velocity value at a particular point over a specified period of time, usually expressed in percentage. Velocity measurements were recorded between 3m/s to 30m/s. At each reference velocity, 60 samples were taken in 2 minutes interval (0.5 Hz) and from the data obtained; turbulence intensity was computed on a spread sheet using the equations below (Eqn A.6, A.7 and A.8). A plot of turbulence intensity variation with velocity was made (see Fig A.9). From the plot, it is clear that the turbulence intensity of the wind tunnel decreases from a maximum value of 3.85% at 3m/s and stabilizes slightly to 0.37% (between 12m/s to 21m/s) as the velocity is increased. Overall, the average turbulence intensity of the wind tunnel within its operational range is 0.81%.

Mean Velocity: $$V_{mean} = \frac{1}{N} \sum_1^N V_i \tag{A.6}$$

Standard Deviation of Velocity: $$V_{rms} = \left(\frac{1}{N-1} \sum_1^N (V_i - V_{mean})^2 \right)^{0.5} \tag{A.7}$$

Turbulence Intensity: $$T_u = \frac{V_{rms}}{V_{mean}} \times 100\% \tag{A.8}$$
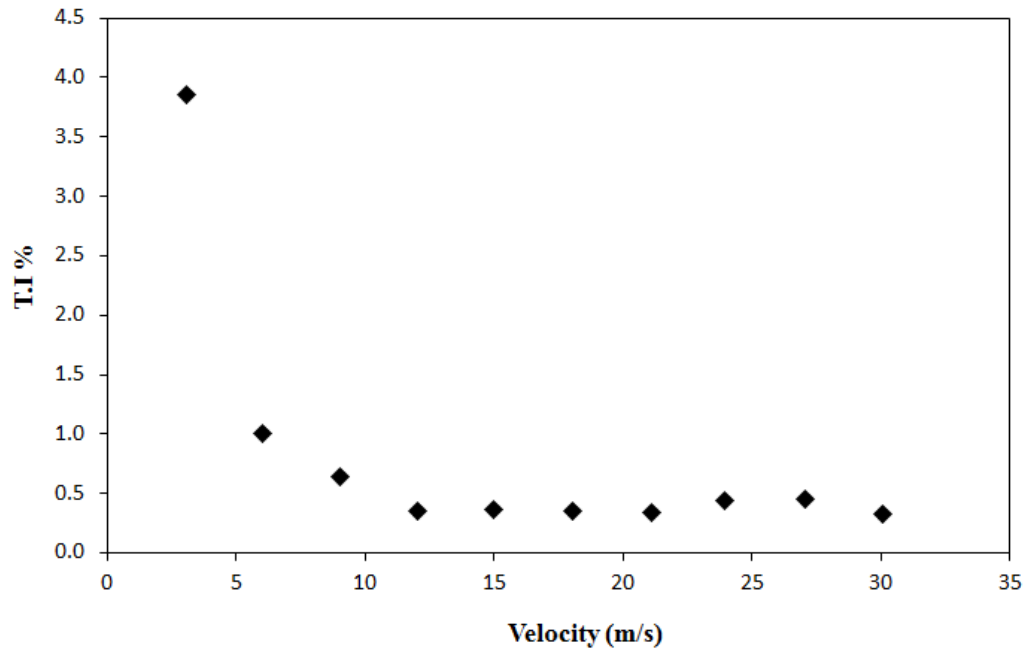
Figure A.9: Variation of turbulence intensity with velocity at the middle of the working section.

Appendix B

Figure B.1 below is the downloaded coordinates of the NACA0018 aerofoil.

		#NACA0018										
Point	X_cord	Y_cord	Z_cord	Point	X_cord	Y_cord	Z_cord	Point	X_cord	Y_cord	Z_cord
1	1.0000	0.0000	0	51	0.2500	0.0891	0	101	0.2500	-0.0891	0
2	0.9996	0.0001	0	52	0.2321	0.0883	0	102	0.2684	-0.0897	0
3	0.9982	0.0004	0	53	0.2146	0.0872	0	103	0.2871	-0.0900	0
4	0.9961	0.0009	0	54	0.1977	0.0859	0	104	0.3062	-0.0900	0
5	0.9930	0.0015	0	55	0.1813	0.0842	0	105	0.3257	-0.0898	0
6	0.9891	0.0024	0	56	0.1654	0.0824	0	106	0.3455	-0.0893	0
7	0.9843	0.0034	0	57	0.1502	0.0802	0	107	0.3655	-0.0887	0
8	0.9787	0.0046	0	58	0.1355	0.0778	0	108	0.3858	-0.0877	0
9	0.9722	0.0060	0	59	0.1215	0.0751	0	109	0.4063	-0.0866	0
10	0.9649	0.0075	0	60	0.1082	0.0722	0	110	0.4270	-0.0853	0
11	0.9568	0.0092	0	61	0.0955	0.0691	0	111	0.4477	-0.0838	0
12	0.9479	0.0110	0	62	0.0835	0.0657	0	112	0.4686	-0.0821	0
13	0.9382	0.0130	0	63	0.0723	0.0621	0	113	0.4895	-0.0803	0
14	0.9277	0.0151	0	64	0.0618	0.0583	0	114	0.5105	-0.0783	0
15	0.9165	0.0173	0	65	0.0521	0.0543	0	115	0.5314	-0.0761	0
16	0.9045	0.0196	0	66	0.0432	0.0501	0	116	0.5523	-0.0739	0
17	0.8918	0.0220	0	67	0.0351	0.0457	0	117	0.5730	-0.0715	0
18	0.8785	0.0246	0	68	0.0278	0.0412	0	118	0.5937	-0.0690	0
19	0.8645	0.0272	0	69	0.0213	0.0365	0	119	0.6142	-0.0664	0
20	0.8498	0.0298	0	70	0.0157	0.0316	0	120	0.6345	-0.0638	0
21	0.8346	0.0326	0	71	0.0109	0.0267	0	121	0.6545	-0.0610	0
22	0.8187	0.0354	0	72	0.0070	0.0216	0	122	0.6743	-0.0583	0
23	0.8023	0.0382	0	73	0.0039	0.0163	0	123	0.6938	-0.0554	0
24	0.7854	0.0410	0	74	0.0018	0.0110	0	124	0.7129	-0.0526	0
25	0.7679	0.0439	0	75	0.0004	0.0055	0	125	0.7316	-0.0497	0
26	0.7500	0.0468	0	76	0.0000	0.0000	0	126	0.7500	-0.0468	0
27	0.7316	0.0497	0	77	0.0004	-0.0055	0	127	0.7679	-0.0439	0
28	0.7129	0.0526	0	78	0.0018	-0.0110	0	128	0.7854	-0.0410	0
29	0.6938	0.0554	0	79	0.0039	-0.0163	0	129	0.8023	-0.0382	0
30	0.6743	0.0583	0	80	0.0070	-0.0216	0	130	0.8187	-0.0354	0
31	0.6545	0.0610	0	81	0.0109	-0.0267	0	131	0.8346	-0.0326	0
32	0.6345	0.0638	0	82	0.0157	-0.0316	0	132	0.8498	-0.0298	0
33	0.6142	0.0664	0	83	0.0213	-0.0365	0	133	0.8645	-0.0272	0
34	0.5937	0.0690	0	84	0.0278	-0.0412	0	134	0.8785	-0.0246	0
35	0.5730	0.0715	0	85	0.0351	-0.0457	0	135	0.8918	-0.0220	0
36	0.5523	0.0739	0	86	0.0432	-0.0501	0	136	0.9045	-0.0196	0
37	0.5314	0.0761	0	87	0.0521	-0.0543	0	137	0.9165	-0.0173	0
38	0.5105	0.0783	0	88	0.0618	-0.0583	0	138	0.9277	-0.0151	0
39	0.4895	0.0803	0	89	0.0723	-0.0621	0	139	0.9382	-0.0130	0
40	0.4686	0.0821	0	90	0.0835	-0.0657	0	140	0.9479	-0.0110	0
41	0.4477	0.0838	0	91	0.0955	-0.0691	0	141	0.9568	-0.0092	0
42	0.4270	0.0853	0	92	0.1082	-0.0722	0	142	0.9649	-0.0075	0
43	0.4063	0.0866	0	93	0.1215	-0.0751	0	143	0.9722	-0.0060	0
44	0.3858	0.0877	0	94	0.1355	-0.0778	0	144	0.9787	-0.0046	0
45	0.3655	0.0887	0	95	0.1502	-0.0802	0	145	0.9843	-0.0034	0
46	0.3455	0.0893	0	96	0.1654	-0.0824	0	146	0.9891	-0.0024	0
47	0.3257	0.0898	0	97	0.1813	-0.0842	0	147	0.9930	-0.0015	0
48	0.3062	0.0900	0	98	0.1977	-0.0859	0	148	0.9961	-0.0009	0
49	0.2871	0.0900	0	99	0.2146	-0.0872	0	149	0.9982	-0.0004	0
50	0.2684	0.0897	0	100	0.2321	-0.0883	0	150	0.9996	-0.0001	0
								0	1.0000	0.0000	0

Figure B.1: Aerofoil coordinates

Appendix C

Formulation of the turbulence model

Where μ_t is the turbulence eddy viscosity (kgm^{-1}s^{-1}), it is computed as;

$$\mu_t = \frac{\rho a_1 k}{\max(a_1 \omega, S F_2)}$$

$$\tau_{ij} = \mu_t \left(2 S_{ij} - \frac{2}{3} \frac{\partial u_k}{\partial x_k} \delta_{ij} \right) - \frac{2}{3} \rho k \delta_{ij}$$

$$S_{ij} = \frac{1}{2} \left(\frac{\partial u_j}{\partial x_i} + \frac{\partial u_i}{\partial x_j} \right)$$

The additional enclosure equation and constants are also given by

$$P_k = \min \left(\tau_{ij} \frac{\partial u_i}{\partial x_j}, 10 \beta^* k \omega \right)$$

P_k is a production limiter used in the Menter's shear stress transport turbulence model to prevent the build-up of turbulence in stagnation regions.

$$F_2 = \tanh \left\{ \left[\max \left(\frac{2\sqrt{k}}{\beta^* \omega y}, \frac{500 \nu}{y^2 \omega} \right) \right]^2 \right\}$$

$$F_2 = \tanh \left\{ \left\{ \min \left[\max \left(\frac{\sqrt{k}}{\beta^* \omega y}, \frac{500 \nu}{y^2 \omega} \right), \frac{4 \sigma_{\omega 2} k}{CD_{k\omega} y^2} \right] \right\}^4 \right\}$$

$$CD_{k\omega} = \max \left(2 \rho \sigma_{\omega 2} \frac{1}{\omega} \frac{\partial k}{\partial x_i} \frac{\partial \omega}{\partial x_i}, 10^{-10} \right)$$

F_1 denotes blending function, it is equal to zero away from the surface (k-ε model), and switches over to one inside the boundary layer (k- ω model). All of the constants (Φ) are a blend of inner (Φ1) and outer (Φ2) constants, blended via the following linear equation:

$$\Phi = F_1\Phi_1 + (1 - F_1)\Phi_2$$

$\beta^* = 0.09, \ \sigma_{k1} = 0.85, \sigma_{k2} = 1, \ \sigma_{\omega 1} = 0.5, \sigma_{\omega 2} = 0.856,$